University of Technology, Sydney

Doctoral Thesis

Development and Implementation of Environmental Photoelectron Yield Spectroscopy

Author:
Toby William Shanley

Supervisor:
Prof. Milos Toth
A. Prof. Igor Aharonovich
Prof. Matthew Phillips

A thesis submitted in fulfilment of the requirements
for the degree of Doctor of Philosophy

in the

Materials and Technology for Energy Efficiency
School of Physics and Advanced Materials

February 2017

Declaration of Authorship

I, Toby William Shanley, declare that this thesis titled, Development and Implementation of Environmental Photoelectron Yield Spectroscopy, and the work presented in it is my own.

- I certify that the work in this thesis has not previously been submitted for a degree nor has it been submitted as part of requirements for a degree except as fully acknowledged within the text.
- I also certify that the thesis has been written by me. Any help that I have received in my research work and the preparation of the thesis itself has been acknowledged. In addition, I certify that all information sources and literature used are indicated in the thesis.

Signed: _____

Date: _____

"Productive stupidity means being ignorant by choice."

Martin Schwartz

UNIVERSITY OF TECHNOLOGY, SYDNEY

Abstract

Faculty of Science
School of Physics and Advanced Materials

Doctor of Philosophy

Development and Implementation of Environmental Photoelectron Yield Spectroscopy

by Toby William Shanley

Environmental photoelectron yield spectroscopy (EPYS) is a novel, low vacuum, surface analysis technique that probes the electronic structure of solid-gas interfaces. Unlike its conventional, ultra high vacuum counterparts that interrogate ideal surfaces in non-realistic conditions, EPYS enables real-time characterisation of dynamic surface processes in semi-realistic, reactive gaseous environments. This capability is a requirement for the technological progress and fundamental understanding of processes in nanotechnology, materials physics, chemistry and bio-sciences.

The system has been built and implemented from the outset of its existence at UTS. This project has contributed to the development of EPYS, and further developed a number of novel applications. Specifically, its application in elucidating the nature of four, fundamentally different physical phenomena is demonstrated. The thesis describes the origins of EPYS in ultra high vacuum photoelectron emission spectroscopy and the theoretical groundwork on which it is based. It also details the EPYS development, and demonstrates applications of the EPYS in the analysis of gas ionisation cascades, subsurface defects, surface termination, and adsorbate coverage.

The value of this study is partly in the instrumentation development itself, but also in the demonstration of its application in studies of material systems responding to their environments.

Acknowledgements

I am grateful for the guidance and support that my supervisors, Milos Toth, Matthew Phillips and Igor Aharonovich have granted me during my studies. Their knowledge, creativity and approach to both research and supervision enabled me, not only to see this project to completion, but gave me the opportunity to do so with enjoyment and great satisfaction.

I am indebted to the technical staff of the Microscopy Analysis Unit and the University workshop: Geoff McCredie; Katie McBean; Mark Berkahn; Greg Delsanto; Greg Evans and the late Paul Fanos for their persistent advice and patient assistance.

To my colleagues, the post graduate students, thank you for the many enlightening conversations. One was never without good company in the lab.

I must finally thank my friends and family, who have supported and encouraged me throughout this period. In particular, I am thankful for the help that my father, Chris, has afforded me, and deeply grateful for the love and companionship of my partner Sarah, who has endured me kindly. Thank you.

Contents

Declaration of Authorship ii

Abstract iv

Acknowledgements v

List of Figures ix

Abbreviations xvii

Contributing Publications xix

Non-Contributing Publications xx

1 Introduction 1
- 1.1 Project objectives and methodology . . . 1
- 1.2 Thesis outline . . . 1

2 Background and literature 3
- 2.1 Overview . . . 3
- 2.2 Photoelectron emission spectroscopy in modern surface science . . . 4
- 2.3 Photoelectron spectroscopy (PES) in ultra high vacuum . . . 5
  - 2.3.1 History and development . . . 5
- 2.4 Photoemission yield spectroscopy (PYS) . . . 8
  - 2.4.1 General theory . . . 10
  - 2.4.2 Theory of threshold determination . . . 12
- 2.5 Surface characterisation . . . 16
- 2.6 Atmospheric photoelectron yield spectroscopy . . . 22
- 2.7 Townsend gas capacitance model . . . 23
- 2.8 Limitations of existing knowledge . . . 24

3 EPYS development 25
- 3.1 Overview . . . 25
- 3.2 Introduction . . . 25
- 3.3 Vacuum chamber . . . 29
- 3.4 Sample stage . . . 32
- 3.5 Detector . . . 34
- 3.6 Light delivery . . . 36
  - 3.6.1 System response . . . 37

3.7 Gas delivery . . . 38
3.8 Automation and control . . . 39

4 Application of EPYS: gas cascade amplification 41
4.1 Summary . . . 41
4.2 Introduction . . . 41
4.2.1 Gas amplification model . . . 42
4.2.2 Positive feedback and breakdown . . . 43
4.3 Experimental methods . . . 44
4.3.1 ESEM . . . 44
4.3.2 EPYS . . . 45
4.4 Results . . . 47
4.5 Discussion . . . 50
4.5.1 Dependence of amplification on pressure . . . 51
4.5.2 Dependence of amplification on detector bias . . . 52
4.5.3 Ultimate amplification efficiency and dielectric breakdown . . . 53
4.6 Conclusion . . . 54
4.7 Implications . . . 55

5 Application of EPYS: characterisation of subsurface defects and sensitivity to ambient gas 56
5.1 Summary . . . 56
5.2 Introduction . . . 57
5.2.1 Intrinsic point defects in ZnO . . . 58
5.2.1.1 Oxygen vacancies . . . 59
5.2.1.2 Zinc vacancies . . . 60
5.2.2 Optical properties . . . 61
5.2.2.1 Near band edge luminescence . . . 61
5.2.2.2 Defect luminescence . . . 62
5.2.3 Electrical properties . . . 63
5.3 Experimental methods . . . 63
5.3.1 Sensitivity to NH_3 . . . 64
5.4 Results . . . 65
5.4.1 Sensitivity to NH_3 . . . 68
5.5 Discussion . . . 70
5.5.1 Sensitivity to NH_3 . . . 75
5.6 Conclusion . . . 76
5.7 Implications . . . 77

6 Application of EPYS: in-situ study of surface functionalisation 79
6.1 Summary . . . 79
6.2 Introduction . . . 79
6.2.1 Nitrogen-vacancy centre in diamond . . . 80
6.2.2 Hydrogen and fluorine terminated diamond . . . 82
6.2.2.1 Hydrogen terminated diamond . . . 82
6.2.2.2 Fluorine terminated diamond . . . 84
6.3 Experimental methods . . . 86

6.3.1 Thermally activated fluorination . . . 87
6.3.2 Electron beam induced fluorination . . . 87
6.4 Results . . . 88
6.5 Discussion . . . 91
6.6 Conclusion . . . 93
6.7 Implications . . . 93

7 Application of EPYS: monitoring adsorbate coverage 95
7.1 Summary . . . 95
7.2 Introduction . . . 95
7.2.1 CO oxidation reaction . . . 96
7.2.2 CO on platinum . . . 97
7.3 Experimental methods . . . 99
7.4 Results . . . 101
7.5 Discussion . . . 105
7.6 Conclusion . . . 109
7.7 Implications . . . 109

8 Conclusion 110

A Townsend gas capacitance model 112

B EPYS Standard Operating Procedure 119
B.1 Purpose . . . 119
B.2 Procedures . . . 119
B.2.1 Venting EPYS Chamber . . . 119
B.2.2 Removing/Loading samples into EPYS Chamber . . . 120
B.2.3 Pumping EPYS Chamber . . . 120
B.2.4 Operating EPYS Chamber . . . 121
B.2.4.1 Introducing Gas . . . 121
B.2.4.2 Set-up Light Delivery . . . 122
B.2.4.3 Set-up Detector Voltage and Begin Measurement . . . 123
B.2.4.4 Finish Measurement . . . 124
B.3 Heating and Cooling Sample Stage . . . 124
B.3.1 Heating . . . 125
B.3.2 Cooling . . . 126
B.4 Calibrate Light Delivery . . . 127
B.4.1 Gathering System Response . . . 128
B.5 Troubleshoot LabView – Instrument Communication Errors . . . 128
B.5.1 Monochromator . . . 128
B.5.2 Beam Chem Monitor . . . 129
B.6 Troubleshoot Hardware Failure . . . 129
B.7 Data Processing and Analysis . . . 130
B.7.1 EPYS Spectral Analysis in Igor Pro . . . 131
B.8 Using the EPYS Chamber for DC Plasma Treatment . . . 131

Bibliography 132

List of Figures

2.1 Representation of the photoelectron emission process. Together, the diagrams compare the initial energetic positions of electrons within a solid to the final energy distribution of free photoelectrons, when excited by a monochromatic light source of energy hv. on the x and y axis respectively, N(E) represents the number of of electrons, while E represents the energy of electrons; E_F represents the Fermi level within the sample; V_S is the energy required for an electron to escape the material surface; $\hbar w$ is the incident photon energy; E_K is kinetic energy of free photoelectrons in vacuum; Φ_S is the surface work function; and Φ_A is the energy of a free electron in vacuum reference to E_F. The difference between Φ_S and Φ_A is due to a dipole at solid-vacuum interface. 6

2.2 Diagram of energy versus density of states showing the relationship between the density of states of electrons within the valence band, the energy of excitation, and the total number of photoelectron emitted from a surface. The yield is the integral of the density of states between E_{VAC} and hv below the E_{VAC}. This expression for the yield must also be scaled by the probability of an excited carrier's transport to, and escape from the surface. 9

2.3 Intersection of the 'optical surface' and the 'escape surface' from [67]. The region bound by these surfaces contain the k values for which the probability of excitation may be calculated. As electron energy E decreases, the circle of intersection shrinks to k_d, the momentum corresponding to photoelectron emission threshold energy. 13

2.4 Summary of Ballantyne's results for the threshold determination of PES from semiconductors and metals [55]. Notably, the yield from most semiconductors was predicted to increase linearly with the cube root of incident photon energy, and the yield from most metals was predicted to increase linearly with the square root of incident photon energy. 15

2.5 Density of states derived from PYS data on the Si (111) 2×1 reconstructed surface. The solid lines represent the total density of states and the dashed lines represent densities of individual states. Trace 1) is plotted against the logarithmic axis on the left and trace 2) is plotted against the linear axis on the right. The spectra revealed the presence of inter-bandgap, dangling bond states at the Si surface. 16

2.6 Comparison between PYS data and the electronic band structure it represents. (a) PYS spectra of GaAs(111): the solid line is the photoelectron yield and the dashed line is the derivative of the yield which represents the density of states. The lower dashed line is the derivative plotted against a linear vertical axis (right side). (b) the derivative of the yield plotted on a band diagram to highlight how energetic positions correspond to photoemission thresholds [70]. 17
2.7 PYS spectra from Ristein et. al. showing photoelectron emission from inter-bandgap states at 4.4 eV, and enhanced photoelectron emission strength for NEA diamond attributed to exciton-phonon induced free electron generation at 5.485 eV. 18
2.8 PYS spectra from Ristein et al. of single crystal type IIb diamond (111) and (100) surfaces after exposure to hydrogen plasma [75]. The sharp increase at 5.54 eV marks the exciton absorption edge, and confirms a NEA. 19
2.9 Experimental setup of an atmospheric PYS system developed by Honda et al. [57]. 21
2.10 Atmospheric PYS spectra of Phthalocyanine films upon repeated exposure to air and evacuation of the vacuum chamber. Honda et al. identified two separate photoelectron emission thresholds, and observed an increase in the ionisation potential upon exposure to air [57]. 21
2.11 Atmospheric PYS spectra collected by Nakayama el al. showing an increase in the ionisation potential of single crystalline ruberene during photo-oxidation [81]. The increase in the ionisation potential was attributed to generation of polar oxide molecules and reversible physisorption of H_2O. 23

3.1 Photograph of the complete EPYS instrument. 27
3.2 Photographs of the EPYS system showing: (a) The EPYS chamber, wrapped in foil to enable uniform heating of the inner side walls, with a TMP connected to the front 8" port and a variety of feedthroughs for electrical connections and gas delivery; (b) The top flange that hosts the majority of feedthroughs and a sapphire window that is positioned above the sample and detector; (c) Light being directed through the sapphire window onto the sample inside the chamber. The diameter of the irradiated spot is 5 mm; (d) The vacuum side of the top flange which consists of an annular GED held in place with a Macor ring and a gas injection needle pointing towards the centre. 28
3.3 Photograph of the (a) back and (b) front of the EPYS chamber. 30
3.4 Schematic of the EPYS system showing: (i) a high voltage power supply connected to the detector; (ii) a Keithley electrometer that measures the current through the sample stage generated by the cascading photoelectrons; (iii) the controllable-flow pumping outlet for operating in low vacuum; (iv) the chamber window through which UV light is passed to the sample; (v) the detector; (vi) the controllable flow inlet from gas delivery lines; (vii) the sample stage, electrically grounded through the electrometer; (viii) the sample heater; and (ix) the current supply for temperature control. 31
3.5 Schematic of the chamber used in the EPYS instrument. 32

3.6 Diagram of the EPYS detector-sample geometry with the excitation source directed through the centre of the detector, onto the sample. Neutral gas molecules between the sample and detector are ionised by photoelectrons moving under the influence of an electric field. 35
3.7 Diagram of the path of light from the deuterium lamp, focused into a Czerny-Turner monochromator with a CaF_2 lens, then collimated and re-focused with CaF_2 lenses onto the delivery optic fibre. 36
3.8 Normalised intensity spectrum of light that is incident on the sample. . . 38
3.9 Diagram of the EPYS gas delivery system. MFCs are used to control the flow of pressurised gaseous sources, while a manual needle valve is adequate for liquid sources like H_2 and C_3H_6O. 39

4.1 Schematic illustration of (a) an ESEM setup and secondary electron amplification in a gas ionisation cascade, (b) an EPYS vacuum chamber and (c) the EPYS measurement process. In both methods, emitted electrons are accelerated by an electric field between the sample and a detector anode, and are multiplied by ionising gas molecules. The EPYS chamber consists of a pumping system (not shown), gas inlet and outlet, specimen stage, heater, gas cascade detector, and an optical window. (d) Shows Lewis diagrams representing the number of valence electrons contributing to the interaction cross sections of H_2O, NH_3 and CH_3CH_2OH 45
4.2 Gas-amplified electron emission current measured versus pressure using ethanol, NH_3 and H_2O. (a) In ESEM, the current is a sum of two components ($I_{\delta+\eta}$) that correspond to cascade-amplified, low energy ($\lesssim 20$ eV) secondary electrons and high energy (keV) backscattered electrons. (b) In EPYS the current (I_p) is generated purely by low energy ($\lesssim 7$ eV) photoelectrons. The detector anode bias was 400 V in both cases. 46
4.3 Gas-amplified electron emission current (I_Σ) and ($I_{\delta+\eta}$) measured versus ESEM detector anode bias using ethanol, NH_3 and H_2O, at gas pressures of (a) 0.1 Torr, (b) 1 Torr, and (c) 5 Torr. The maximum $I_{\delta+\eta}$ reached at the onset of dielectric breakdown of each gas is shown for each pressure on the plots. 48
4.4 Gas-amplified photoelectron emission current (I_p) measured versus EPYS detector anode bias using ethanol, NH_3 and H_2O, at gas pressures of (a) 0.1 Torr, (b) 1 Torr, and (c) 5 Torr. The maximum current reached at the onset of dielectric breakdown of each gas is shown for each pressure on the plots. The three amplification regimes (i, ii and iii) labelled on the plots are discussed in the main text. 49
4.5 Images taken at high and low magnification in (a) and (b): H_2O, (c) and (d): NH_3, (e) and (f): ethanol vapour. The sequences verify that little to no carbon deposition occurs during electron beam irradiation in the presence of ethanol. 50

5.1 Charge states and transition levels of intrinsic point defects in ZnO. The charge states depend on value of the Fermi level. Figure adapted from Janotti and van der Walle [172]. 59
5.2 Formation energies of native point defects in ZnO calculated by Janotti et al. [175]. The formation energies are plotted as a function of the Fermi level position in oxygen (left) and zinc (right) rich conditions. The different slopes of the traces represent different charge states. 60

5.3 Characteristic cathodoluminescence profile from ZnO at room temperature showing the near band edge emission at 3.37 eV and defect related emission arising from inter-bandgap radiative recombination pathways. . . 61
5.4 SEM images of nanorods thermally annealed in (a) O_2 environment (b) Zn vapour environment. The mean diameter and hexagonal structure of the nanorods remains unchanged; however, a slight reorientation with respect to the substrate can be observed. (c) As-grown nanorods (inset highlights high density hexagonal $\langle 0001 \rangle$ growth) and (d) shows XRD patterns of as-grown, O_2 annealed and Zn annealed nanorods. Changes in the relative peak heights arise from a reorientation of the nanorods with respect to the substrate. Data collected by Suranan Anantachaisilp. 66
5.5 Cathodoluminescence spectra of ZnO nanorod samples. The yellow trace is a CL profile from as-grown ZnO nanorods and is dominated by the YL at 1.9 eV. The red trace is a CL profile from O_2 annealed nanorods and shows a large defect emission in the RL band (1.7 eV) and a smaller contribution from the GL (2.5 eV). The green trace is a CL profile from Zn vapour annealed nanorods (magnified by 4) and exhibits GL defect emission and a relatively strong NBE emission. Data collected by Suranan Anantachaisilp. 67
5.6 EPYS spectra of ZnO nanorods. The red trace shows an EPYS spectrum from as-grown nanorods, the green trace is from O_2 annealed nanorods and the blue trace is from Zn vapour annealed nanorods. Both thermally treated samples (O_2 and Zn vapour annealed) exhibited a significantly greater photoelectron emission current than as-grown nanorods. While as-grown and O_2 annealed nanorods both began to emit photoelectrons at 4.5 eV, the Zn vapour annealed nanorods exhibited a lower photoelectron emission threshold at 4.2 eV. 68
5.7 Electrical conductance sensitivity of ZnO nanorods to gaseous NH_3 for (a) as-grown; (c) O_2 annealed; and (e) Zn vapour annealed samples. Figures (b), (d) and (f) show the corresponding ratio of the chance in conductivity as a function of NH_3 concentration. Data collected by Suranan Anantachaisilp. 69
5.8 EPYS spectra from as-grown ZnO nanorods collected in an environment transitioning from argon into gaseous NH_3. The blue traces were collected initially in a dry, argon environment, and the pale red traces were collected in a NH_3 environment. Inset shows the spectra on a log-linear scale. As the partial pressure of NH_3 increases, the photoelectron emission threshold decreases. The gaps in the spectra are periods during which NH_3 is introduced to the chamber: spectra were not collected during this period as the detector bias had to be adjusted to compensate for the changing amplification medium. 70
5.9 EPYS spectra from oxygen annealed ZnO nanorods collected in an environment transitioning from argon into gaseous NH_3. The blue traces were collected initially in a dry, argon environment, and the pale red traces were collected in a NH_3 environment. Inset shows the spectra on a log-linear scale. As the partial pressure of NH_3 increases, the photoelectron emission threshold decreases. 71

5.10 EPYS spectra from zinc annealed ZnO nanorods collected in an environment transitioning from argon into gaseous NH_3. The blue traces were collected initially in a dry, argon environment, and the pale red traces were collected in a NH_3 environment. Inset shows the spectra on a log-linear scale. As the partial pressure of NH_3 increases, the photoelectron emission threshold decreases. 71
5.11 Band diagrams for the as-grown, oxygen annealed and zinc annealed ZnO samples. The Fermi level sits higher with respect to the conduction and valence bands in oxygen annealed and zinc annealed samples, and the zinc annealed ZnO exhibits greater downward band bending due to the presence of V_o. 74

6.1 The diamond crystal lattice structure (left) containing a NV defect and the electronic structure of the NV^- in diamond (right) [211]. 80
6.2 Characteristic photoluminescence spectra of the NV^- (red) and NV^0 (blue) defects in diamond. 81
6.3 Electrical conductivity data from Maier et al. [248] showing the change in surface conductivity when hydrogen terminated diamond is exposed to air. 83
6.4 Top: Schematic of the hydrogenated diamond surface in contact with a H_2O overlayer taken from Maier et al. [248]. Bottom: Evolution of the band bending during the electron transfer process at the interface between diamond and the H_2O overlayer. 85
6.5 Photograph of the confocal photoluminescence setup used in this study. The lens in the foreground focuses excitation light into a 0.5 μm^2 spot on the sample, and also collects the photoluminescence from the sample. . . 86
6.6 A schematic of the confocal photoluminescence setup used in this study. A 532 nm excitation laser is directed onto the sample, and its x-y position at the sample surface scanned using a piezoelectric scanning mirror. Emitted and reflected light returns along the path of the excitation laser until they are separated at a dichroic mirror. The photons generated by the sample are allowed to pass through the dichroic mirror, where they are detected by avalanche photodiodes for panchromatic mapping, and/or a spectrometer. 88
6.7 Normalised photoelectron yield spectra of H-terminated diamond (acquired in a H_2 environment) and F-terminated diamond (acquired in NF_3 vapour). The latter were generated by thermal (solid line) and electron beam (dashed line) induced fluorination. 89
6.8 (a) Schematic illustration of nanodiamonds before, during and after electron beam irradiation in NF_3 vapour. (b) SEM image of a cluster of nanodiamonds. (c) PL spectra collected from virgin, H-terminated, and irradiated nanodiamonds (solid lines). (d) PL map showing the sample region that was irradiated by an electron beam. The dashed traces in (c) show 5 additional spectra acquired from the virgin and irradiated sample regions, illustrating the consistency of data collected from H-terminated and irradiated nanodiamonds. 90
6.9 Simplified schematic of a diamond surface terminated with hydrogen and fluorine. [E_{CB} = conduction band minimum, E_{VB} = valence band maximum, E_F = Fermi level, E_{VAC} = vacuum level, ξ = ionisation energy] . . 91

6.10 Illustration of the activation of near-surface NV^- defects in nanodiamonds by irradiation with an electron beam in the presence of NF_3. Electron bombardment removes a protective water overlayer, and exposed bare hydrogen terminated diamond to NF_3, which then undergoes a spontaneous exchange reaction, fluorinating the nanodiamonds. 92

7.1 Temporal evolution of reaction diffusion spiral waves. The fronts of the waves are where a CO oxidation reaction is taking place with adsorbed O^- on Pt. The dark lines are O^- covered and the white spaces are CO covered [294]. 97

7.2 Potential energy diagrams of the three chemisorbed states of CO on platinum. The binding strength decreases with increasing coverage due to adsorbate-adsorbate interactions. When there is less CO present, the adsorbate molecule binds more strongly with the Pt atoms (hybridised C-Pt bonds) and when there is more CO, the nature of the C-Pt bonding changes, resulting in a more weakly bound state. 98

7.3 Speculative schematic of how coverage of CO molecules on platinum atoms affects the CO-platinum bonding configuration (taken from Culver [296]). (1) represents the most strongly bound state in the lowest coverage regime, while (5) shows a weakly bound state situated between chemisorbed CO molecules. 99

7.4 Temperature-resolved EPYS spectra acquired while Pt was heated in a CO environment. The blue traces were collected at ∼47°C the temperature was incrementally increased and recorded for each set of spectra until reaching ∼380°C, shown in red. After collecting spectra at 380°C, the temperature was decreased to 307°C to check for reversibility. The inset is a log-linear plot of the same data that highlights the shifting photoelectron emission threshold. 101

7.5 Temperature-resolved EPYS spectra acquired while Pt was cooled in a CO environment. The light red traces were collected at ∼380°C, the temperature was allowed to decrease until reaching room temperature, shown in blue. The temperature was measured only at the start and end of this experiment due to the influence of measuring temperature on the EPYS signal integrity. The inset is a log-linear plot of the same data that highlights the decreasing photoelectron emission threshold. 102

7.6 Work function determined from the average of photoelectron emission thresholds collected as a function of sample temperature. The existence of different binding states can explain the nonlinear relationship between the observed work functions and temperature. 103

7.7 (Top) A repeat experiment monitoring the photoelectron emission from CO-covered Pt with increasing temperature in which O_2 was injected at ∼370°C. Upon O_2 injection, the work function immediately decreased, and then returned to its former CO covered state. (Bottom) The corresponding residual gas analysis of this experiment. The work function slowly returns to its high temperature CO-covered state as O_2 is depleted via the CO oxidation reaction. 104

7.8 Distribution of binding states of CO on Pt taken from Nishiyama [299]. . 107

7.9 Desorption kinetics of CO chemisorbed on Pt taken from Nishiyama [299]. 107

A.1 Simulated $\alpha(z)$ curve [86] for typical gas cascade detector operating conditions (d_{gap} =8.5 mm, p =5 Torr and V =500 Volts). Regions I to III represent different ionisation efficiencies as electrons move through the gap. Region 1: no ionisation by low energy electrons near the sample surface; Region II represents increasing ionisation efficiency as electrons are accelerated under the electric field; Region II: swarm conditions and constant ionisation efficiency where energy gained under the influence of an the electric field is equal to the energy loss from inelastic scattering collisions. 113

A.2 Gas cascade amplification $\mathcal{A}$ versus H_2O pressure as a function of (a) detector voltage at d_{gap} = 5 mm and (b) sample-detector separation distance. Figure adapted from [310] 116

A.3 Gas cascade amplification $\mathcal{A}$ versus (a) detector voltage at d_{gap} = 5 mm and (b) sample-detector separation distance calculated at four pressures: 2, 3, 4 and 5 Torr of H_2O. Figure adapted from [310]. 117

Abbreviations

AES	**A**uger **E**lectron **S**pectroscopy
APD	**A**valanche **P**hoto**d**iode
ARPES	**A**ngle **R**esolved **P**hotoelectron **E**emission **S**pectroscopy
BSE	**B**acks**s**cattered **E**lectron
CBM	**C**onduction **B**and **M**inimum
CCD	**C**harge **C**oupled **D**etector
CL	**C**athodo**l**uminescence
DAP	**D**onor **A**cceptor **P**air
DAQ	**D**ata **Acq**uisition
DOS	**D**ensity **O**f **S**tates
$\mathbf{E_{CB}}$	**E**nergy of **C**onduction **B**and minimum
$\mathbf{E_F}$	**E**nergy of **F**ermi level
$\mathbf{E_V}$	**E**nergy of a free electron in **V**acuum
$\mathbf{E_{VB}}$	**E**nergy of **V**alence **B**and maximum
EPYS	**E**nvironmental **P**hotoelectron (emission) **Y**ield **S**pectroscopy
ESEM	**E**nvironmental **S**canning **E**lectron **M**icroscope
FWHM	**F**ull **W**idth **H**alf **M**aximum
GED	**G**aseous **E**lectron **D**etector
GL	**G**reen **L**uminescence
LEED	**L**ow **E**energy **E**lectron **D**iffraction
MFC	**M**ass **F**low **C**ontroller
NBE	**N**ear **B**and **E**dge
NEA	**N**egative **E**lectron **A**ffinity
NV	**N**itrogen **V**acancy
$\mathbf{O_i}$	**I**nterstitial **O**xygen

PE	**P**rimary **E**lectron
PEA	**P**ositive **E**lectron **A**ffinity
PES	**P**hotoelectron **E**mission **S**pectroscopy
PI	**P**ositive **I**on
PID	**P**roportional-**I**ntegral-**D**erivative
PL	**P**hoto**l**uminescence
PMT	**P**hoto**m**ultiplier **T**ube
PYS	**P**hotoelectron (emission) **Y**ield **S**pectroscopy
RGA	**R**esidual **G**as **A**nalyser
RL	**R**ed **L**uminescence
SE	**S**econdary **E**lectron
SEM	**S**canning **E**lectron **M**icroscope
SFG	**S**um **F**requency **G**eneration
SHE	**S**tandard **H**ydrogen **E**lectrode
TDS	**T**hermal **D**esorption **S**pectroscopy
TMP	**T**urbo **M**olecular **P**ump
UHV	**U**ltra **H**igh **V**acuum
UPS	**U**ltraviolet **P**hotoelectron (emission) **S**pectroscopy
UV	**U**ltra**v**iolet
$\mathbf{V_O}$	**O**xygen **V**acancy
$\mathbf{V_{Zn}}$	**Z**inc **V**acancy
VBM	**V**alence **B**and **M**aximum
WRG	**W**ide **R**ange **G**auge
XANES	**X**-ray **A**bsorption **N**ear **E**dge **S**tructure
XPS	**X**-ray **P**hotoelectron (emission) **S**pectroscopy
XRD	**X**-**r**ay **D**iffraction
YL	**Y**ellow **L**uminescence
$\mathbf{Zn_i}$	**I**nterstitial **Z**inc
ZPL	**Z**ero **P**honon **L**ine

Contributing Publications

- Localized Chemical Switching of the Charge State of Nitrogen-Vacancy Luminescent Centers in Diamond, **Toby Shanley**, Aiden Martin, Igor Aharonovich, Milos Toth, *Applied Physics Letters 105*, 063103, Published 11 August 2014

- Role of Gas Molecule Complexity in Environmental Electron Microscopy and Environmental Photoelectron Yield Spectroscopy, **Toby Shanley**, Fadi Bonnie, John Scott, Milos Toth, *in submission*

- Band Structure of Stoichiometrically dissimilar ZnO surfaces, **Toby Shanley**, Suranan Anantachaisilpm Matthew Phillips, Milos Toth, *in submission*

Non-Contributing Publications

- Silicon Oxide Nanowire Growth Mechanisms Revealed by Real-Time Electron Microscopy, Miroslav Kolibal, Libor Novak, **Toby Shanley**, Milos Toth, Tomas Sikola, *Nanoscale 8* 266-275, Published 26 November 2015

- Synthesis of Liminescent Europium Defects in Diamond, Andrew Magyar, Wenhao Hu, **Toby Shanley**, Michael Flatte, Evelyn Hu, Igor Aharonovich, *Nature Communications 5* 3523, Published 24 March 2014

Chapter 1

Introduction

1.1 Project objectives and methodology

The primary objective of this research project is to develop a novel surface characterisation technique to enable real time analysis of dynamic surface processes that take place in low vacuum environments. The characterisation technique developed is an extension of an existing high vacuum photoelectron emission spectroscopy technique for which the photoelectron detection mechanism is modified to enable higher pressure operation. Applications of the instrument have been demonstrated in the analysis of four fundamentally different phenomena that are discussed in Chapters 4-7. The four physical processes investigated consist of: gas cascade amplification; the role of sub-surface defects in the formation of surface dipole fields; an effect of surface functionalisation on the charge state of sub-surface defects; and real-time observation of surface state evolution arising from adsorbate-adsorbate interactions.

1.2 Thesis outline

In Chapter 2, a background of photoelectron spectroscopy and specifically the technique adapted in this project are presented in addition to the theory of low vacuum electron detection using gas cascade amplification. The technique developed in this project is discussed within the context of modern, low vacuum surface science, and relevant literature and current limitations of similar techniques are presented.

Chapter 3 details the hardware assembled to develop the instrument, its limitations and functionality. Data analysis techniques and experimental methodology are presented.

In Chapter 4, a study of gas cascade amplification is presented, demonstrating a unique capability to study this process with a variety of gaseous molecules using only low energy electrons. EPYS is applied to illuminate the role of molecular complexity in gas cascade amplification by comparing the amplification profiles - as a function of detector bias and chamber pressure - of three different gas species.

In Chapter 5, a model of surface band bending as a result of sub-surface defect formation is developed in conjunction with correlative photoelectron emission, cathodoluminescence and electrical characterisation of ZnO surfaces. Specifically, EPYS is applied to identify the extent and direction of surface band bending using the photoelectron emission threshold to indicate the initial energetic position of valence band electrons. Furthermore, the ability to collect real-time EPYS measurements in a gaseous environment that is changing composition is demonstrated.

In Chapter 6, a technique for locally altering the charge state of near-surface defects in diamond is developed using photoelectron spectroscopy to elucidate a mechanism for spontaneous surface fluorination and the effect of fluorination on surface electronic structure. This is achieved by monitoring a dramatic shift in the photoelectron emission threshold the arises from the substitution of surface-terminating hydrogen by fluorine.

In Chapter 7, the work function of platinum in the presence of gaseous CO is observed to change significantly with temperature. Real-time, temperature resolved EPYS measurements are used to link the observed photoelectron emission changes with CO binding energies. A model for the observed behavior of CO adsorption on platinum invoking the effect of adsorbate-adsorbate interactions on the molecule's energetic state is presented.

In Chapter 8, the thesis is concluded with final remarks and projects for future consideration.

Chapter 2

Background and literature

2.1 Overview

There is no existing literature that employs an EPYS system that is used in gaseous environments other than air and its constituents ; nor is there a standardised methodology for interpreting the data it provides. There are similar instruments that provide comparable information, and comprehensive theoretical considerations of the material properties that it probes. However, there is no other instrument that can probe the pressure or temperature ranges, or utilise the variety of reactive gases that the EPYS is capable of. The purpose of this chapter is to present a background to the phenomena of photoelectron emission and how it has been used to study surfaces. Several variants of photoelectron emission spectroscopy are described, and their contribution to our current understanding of fundamental principles in solid state physics is discussed. Examples are given of how the EPYS predecessor, photoelectron yield spectroscopy, has been used to comprehensively characterise near-bandgap surface electronic structure, and also how recent implementations of PYS-based systems that operate in atmospheric conditions have been used to characterise materials. A semi-phenomenological model - that is partially based on a first principles calculation and scaled by empirically derived probabilities - for the photoelectron excitation and emission process is presented, and gas cascade amplification by electron impact ionisation is also discussed. The latter is a key aspect of the EPYS system, as the gaseous electron amplification mechanism allows low vacuum implementation of a traditionally ultra high vacuum technique.

The importance of developing low vacuum techniques for surface characterisation is stressed in the context of modern science. The significance of material surface properties is growing in the chemical and biological sciences, and understanding the role of solid-gas interfaces in the dynamic environments in which they exist is key to innovating new technologies and opening new avenues of inquiry.

2.2 Photoelectron emission spectroscopy in modern surface science

Photoelectron emission spectroscopy (PES) has been established as one of the most important methods used to study the electronic structure of surfaces [1–4]. PES provides information that has widespread practical implications for fields including surface chemistry and material science [5–8], and has significantly contributed to the understanding of fundamental principles in solid state physics.

Surface science itself has undergone very rapid advances over the last several decades [9, 10]. These advances reveal structural, dynamic, compositional and thermodynamic properties of surfaces that can be utilised in the development of chemical processes that underpin much of nanotechnology and heterogeneous catalysis. Characterisation of single crystal surfaces in vacuum with techniques such as ultraviolet photoelectron spectroscopy (UPS), X-ray photoelectron spectroscopy (XPS), low energy electron diffraction (LEED) and Auger electron spectroscopy (AES), revealed a variety of surface phenomena that led to new concepts in surface science [11–14].

All of these techniques, however, are based on the detection of electrons emitted from a surface directly; thus it is necessary that experiments are performed in ultra high vacuum (UHV). Discoveries made by these vacuum studies include clean surface reconstruction of semiconductors and metals [15–17], the kinks and steps on surfaces that are chemically active, leading to site selectivity for adsorption or dissociation [18–20] and the fact that adsorbed molecules and atoms preferentially occupy certain sites on surfaces and can thus cause further reconstruction.

The development of surface characterisation instruments that operate in high pressure environments has profound implications for studies of fundamental processes that form

the basis of modern nanoscience [9, 10, 21–23]. These include real-time and temperature resolved studies of surface reactions such as oxidation, chemical etching and deposition, catalytic reactions, surface-adsorbate interactions and studies of nanostructure growth processes.

2.3 Photoelectron spectroscopy (PES) in ultra high vacuum

The process of photoelectron emission from solid into vacuum, and the relationship between photon, electron and photoelectron energy is illustrated in Figure 2.1. This schematic of electronic states shows how the final energy distribution of photoelectrons corresponds to the initial density of states, through the excitation energy and surface ionisation potential.

PES is typically identified as being either UPS or XPS, which are distinguished by the energy of excitation (10-50 eV and 200-2000 eV respectively) [2, 24–26]. Both of these and their related techniques essentially involve irradiating a sample with monochromatic light and subsequently analysing the energy of photoelectrons. This provides extensive information about the density of states, ranging from the energetic position and shape of valence, conduction and defect bands in solids to core levels of atoms in UPS and XPS respectively. These techniques are of great significance in modern surface science. However, a requirement for conservation of photoelectron kinetic energy is an ultra high vacuum environment.

2.3.1 History and development

The first experiments to reveal the photoelectric effect were performed by Heinrich Hertz in 1887 [27, 28], before the discovery of the electron. However, observations on the photoelectric effect were not satisfactorily explained until Einstein's hypothesis on the quantisation of light in 1905 [27]. In 1907, the first investigation of "cathode particles emitted under the influence of Rontgen rays" [29] from metal surfaces found that the maximum velocity of photoelectrons did not vary with the intensity of incident light but with the frequency, in agreement with Einstein's theory.

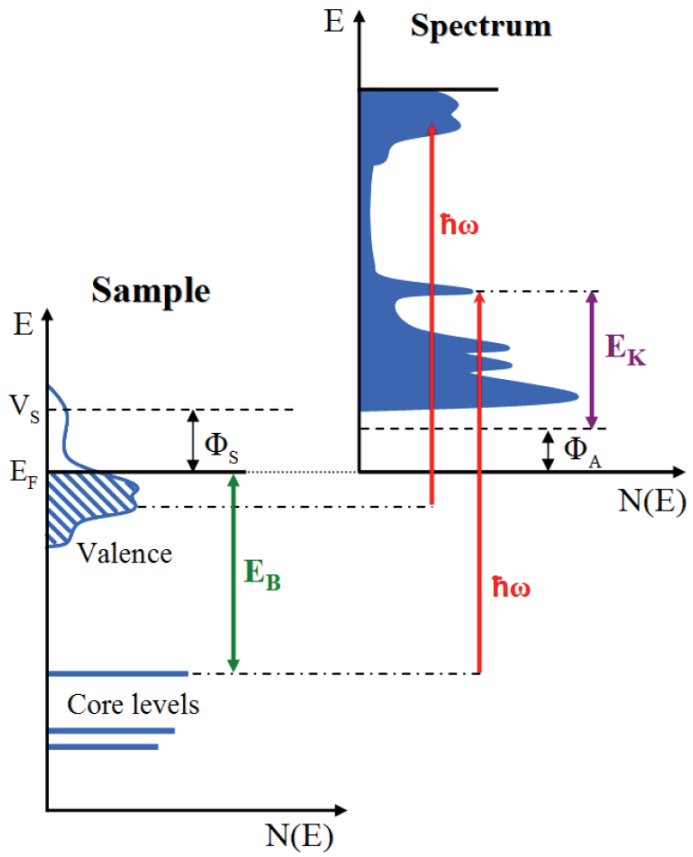

FIGURE 2.1: Representation of the photoelectron emission process. Together, the diagrams compare the initial energetic positions of electrons within a solid to the final energy distribution of free photoelectrons, when excited by a monochromatic light source of energy hv. on the x and y axis respectively, N(E) represents the number of of electrons, while E represents the energy of electrons; E_F represents the Fermi level within the sample; V_S is the energy required for an electron to escape the material surface; $\hbar w$ is the incident photon energy; E_K is kinetic energy of free photoelectrons in vacuum; Φ_S is the surface work function; and Φ_A is the energy of a free electron in vacuum reference to E_F. The difference between Φ_S and Φ_A is due to a dipole at solid-vacuum interface.

Over the following years, experiments performed by Rutherford using X-ray lines and electron energy analysers continued to prove a linear relationship between the frequency of light and the maximum kinetic energy of electrons [30, 31]. However, it seems those working in either the high or low energy regimes (now XPS and UPS) were not aware of each others' work until the 1920s, during which Einstein's concept was given weight by Millikan's experiments on the particle nature of the electric charge [32, 33].

The period between the 1920s and 1960s was characterised by improvement of instrumentation, and a progress in theory [34, 35]. Various electron energy analysers were developed to increase energy resolution and sensitivity. A range of spectral light sources

in both the UV and X-ray range became readily available, in addition to monochromatised radiation from white sources. Vacuum technology also continued to improve, such that the chemical condition of the surfaces became more clearly defined. This experimental side was complimented by enormous progress in the understanding of atomic and solid-state structure from a quantum mechanical point of view and the physics of metals and semiconductors could be described in terms of band structure [27, 36–39].

The theoretical methods for modeling photoelectron emission from metals and semiconductors were pioneered in the early 1960s by several groups [2, 40], in particular by the group of Spicer Berglund [35]. He developed the three-step model involving excitation, transport and escape of electrons; measured the first UPS valence band spectrum on copper; and demonstrated the surface sensitivity of UPS [41–44]. Electronic surface states were first reported in 1962 [45], the study of which became of intense interest and a defining feature of PES [15, 46–48]. Angle-resolved photoelectron emission spectroscopy (ARPES) was realised by Allen, Gobeli and Kane in 1964 [49] and became a unique tool for mapping the dispersion of occupied electron bands in solids. The theory behind ARPES advanced quickly to the point that bonding sites and lengths could be determined by emission from adsorbates [50]. A further degree of complexity in PES experiments was reached with analysis of electron spin. The first observation of electron spin polarisation in photoelectrons was performed using photoelectron yield spectroscopy (PYS) [27] and a flurry of spin related experiments followed [5, 51–54].

In 1972, a theoretical treatment of the photoelectron emission threshold was produced by Ballantyne [55] which was a powerful analysis tool for quantifying the energetic position of initial states. Ballantyne's formalisation of the relationship between the electron yield and incident photon energy is still invoked today in PYS studies [56–59].

Today, most PES experiments are basically carried out in the same way as a century ago. Monochromatic light liberates electrons from the material, which are subsequently analysed with respect to their emission angle and kinetic energy by an electrostatic analyser. However, most of the theoretical and experimental work that has been done advancing PES does not directly apply to environmental PYS due to the methodology of the different techniques.

2.4 Photoemission yield spectroscopy (PYS)

PYS measures total photoelectron yield as a function of incident photon energy. It is a variation of PES that was developed to enable very high energy resolution and sensitivity by exchanging an electron energy analyser and excitation source with an electron counter and a variable monochromatised light source [6, 60–62]. This exchange shifted the energy resolution limit from that of the photoelectron detectors to the excitation monochromator. PYS has proven to be particularly adept at identifying the shape of surface electronic bands and their position with respect to the bulk band structure. The main advantage of PYS is its ability to provide accurate information about filled surface states in the bandgap and upper valence band in addition to values for work function and ionisation energy. The technique is only able to probe a narrow energy range of a few eV below the Fermi level of most metals and semiconductors.

PYS offers a unique possibility to distinguish between surface and bulk states of semiconductors through the properties of space charge regions. With differently doped surfaces, it is possible to modify the population of filled surface states. When surface states are present in the gap up to the Fermi level, the photoelectron emission threshold marks the work function (ϕ). When electronic levels are shifted due to surface band bending, they can be differentiated from bulk states by their photoelectron emission threshold.

The first PYS system was build by Sebenne and his results were first published in 1977 [61, 63, 64]. His measurements allowed high-resolution (20 meV) spectra of the photoelectron current under illumination of light in the energy range 4-6 eV. The main advantage this method had over other techniques was that it could provide very accurate information about filled surface states within the bandgap and states from the upper part of the valence band. A band diagram showing how the energy of the light and the density of states corresponds to the PYS signal collected is shown in Figure 2.2.

PYS methodology consists of measuring the yield (number of photoelectrons per incident photon) as a function of photon energy. This is performed over a small energy range, typically 4-7 eV, and is thus extremely sensitive to emission from the valence band, defects and surface states of the sample. The quantitative and qualitative data gathered using PYS are photoelectron emission thresholds and density of states (DOS) respectively. Thresholds mark the onset of photoelectron emission into vacuum, and an

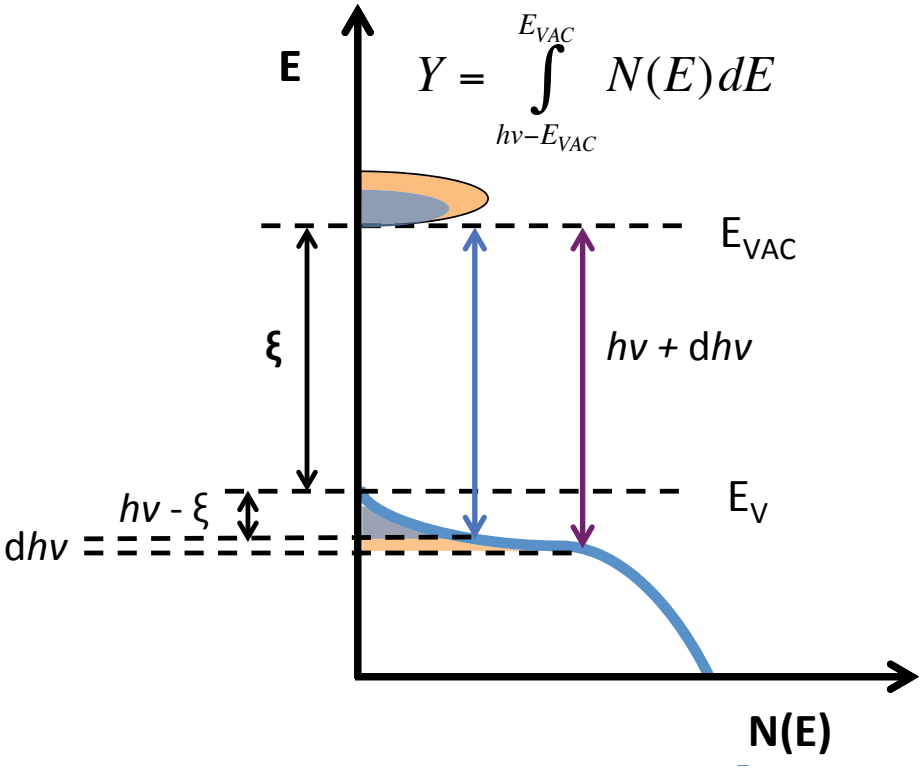

FIGURE 2.2: Diagram of energy versus density of states showing the relationship between the density of states of electrons within the valence band, the energy of excitation, and the total number of photoelectron emitted from a surface. The yield is the integral of the density of states between E_{VAC} and hv below the E_{VAC}. This expression for the yield must also be scaled by the probability of an excited carrier's transport to, and escape from the surface.

effective DOS can be derived from the emission spectrum. The threshold is determined by extrapolating the rate of change in photoelectron yield ($Y(hv)$) over a small energy range at the surface ionisation potential to $Y(hv) = 0$. The $Y(hv)$ varies according to the relationship $Y(hv) = C(hv)^n$ where C is a constant and $n = 2$ or 3 depending on whether the material is a metal or a semiconductor respectively. This is achieved by taking the square or cube root of the yield as a function of photon energy, and fitting a linear plot over an energy range near threshold to intersect with the baseline. The intersection of this fitted line with the background signal marks the minimum energy of an electronic band below the vacuum level. The nature of the threshold value is not always obvious, but it typically represents the work function or the ionisation potential of a metal or semiconductor respectively.

An effective DOS can be derived from the yield curve as $Y(hv)$ increases: $Y(hv + dhv)$ with an increase dhv of the photon energy. $Y(hv + dhv) - Y(hv)$ corresponds to the

states located between hv and $hv+dhv$ below the vacuum level. The first derivative with respect to energy, $dY(hv)/dE$, is an energy distribution curve representative of the DOS, with the assumption that is common to PES and a good approximation over a small range of low energy photons: that the escape function of electrons and the transition matrix elements are constant with respect to energy.

2.4.1 General theory

Photoelectron emission is the ejection of electrons from a solid in response to incident light. It is often modelled in three successive independent steps: (1) excitation of an electron from a filled to an empty state above E_{VAC} by absorption of a photon; (2) transport of the excited electron to surface; and (3) escape from the surface [4]. This method defines the photoelectron current ($I^{-}_{PE}(hv)$) as the product of three terms representing the photoabsorption rate ($P(hv)$), a propagation factor ($T(hv)$) and the escape probability ($D(hv)$).

$$Y(hv) = \frac{N_{PE}}{N_{photons}} = \frac{I^{-}_{PE}}{qJ_0} \tag{2.1}$$

$$I^{-}_{PE}(hv) = qP(hv)T(hv)D(hv) \tag{2.2}$$

Where q is the fundamental unit of electronic charge and J_0 is the photon flux. $P(hv)$ is considered to be the dominant process and is most commonly modelled as the transition rate from a filled to empty state using Fermi's Golden Rule and an interacting Hamiltonian of an incident radiation field. The transition rate from an initial state $|\varphi_i\rangle$ to a final state $\langle\varphi_f|$ is given as

$$P(hv) = C|\langle\varphi_f|A\cdot p|\varphi_i\rangle|^2\delta\left(E_f(k) - E_i(k) - hv\right) \tag{2.3}$$

where $|\langle\varphi_f|A\cdot p|\varphi_i\rangle|^2$ is the transition probability of a photon-induced excitation of a system in the ground state to the final state. $A\cdot p$ is a Hamiltonian perturbation operator that describes the interaction of an electron in the system with the electromagnetic field vector potential A. The delta function enforces energy conservation by making only

transitions that are hv higher than the initial energy state possible. This method is often applied to generate spectral functions and energy distribution curves for UPS and XPS techniques including ARPES, and is less applicable to low energy photoexcitation due to a collapse of the sudden approximation. The sudden approximation relies on the time scale of a transition τ to be much smaller than the response time, Δt, of the initial state to excitation, $\tau \ll \Delta t$. The response time of a state is governed by the time-energy uncertainty principal, in which ΔE is the typical splitting among energy levels, $\Delta t \sim \frac{\hbar}{\Delta E}$, such that for the sudden approximation to hold

$$\tau \ll \frac{\hbar}{\Delta E} \tag{2.4}$$

The transition time τ is inversely proportional to the excited electron's final kinetic energy and corresponding velocity. Intuitively, low energy excitations have longer transition times, and when they approach the response time of the initial state to excitation, the sudden approximation breaks down. It is normally assumed that this approximation is valid for photoelectrons with $E_f - E_i - hv > 20$ eV, which is above the energy of photoelectrons generated in PYS.

The propagation factor $T(hv)$ is the probability that an excited electron with a momentum component towards the surface will reach the surface before undergoing an inelastic scattering event. It is defined by the relationship between the excited electron mean free path λ, and photon attenuation depth θ.

$$T(hv) = \frac{{}^{\lambda}/_{\theta}}{1 + {}^{\lambda}/_{\theta}} \tag{2.5}$$

When the mean free path of excited electrons is large compared to their excitation depth, $\lambda \gg \theta$, the probability of transport to the surface taking place approaches unity $T(hv) \to 1$. Conversely, if the penetration depth of light and hence depth of excitation is larger than the mean free path of electrons, then they are more likely to undergo inelastic scattering events and thermalise before reaching the surface, $T(hv) \to 0$.

The escape probability $D(hv)$ defines the escape criterion, that an electron at the surface must have sufficient energy arising from a momentum component normal to the surface (k_z) that it exceeds the surface energetic barrier

$$D(h\nu) = 1 \text{ for } \frac{\hbar^2 k_z^2}{2m} > E_{VAC} - E_i \tag{2.6}$$

$$D(h\nu) = 0 \text{ for otherwise} \tag{2.7}$$

The following subsection 2.4.2 provides a simple mathematical model for the determination of photoelectron emission threshold.

Numerous microscopic theories of the photoelectron emission process have also been developed. These have included a steady state scattering theory [65], a Kubo response theory [7] and Green's function methods [66]. A description of these methods is not given here; the reader is instead directed to Williams et al. [7] for a review of such theories.

2.4.2 Theory of threshold determination

A small field of theory developed for interpretation of PES experiments which has large implications - specifically for PYS - focuses on methods to determine the photoelectron emission threshold value. Theory on threshold determination was first modelled by Kane in 1962 [67] and subsequently by Ballantyne in 1972 [55]. The method for modelling the yield versus energy involved calculating the rate of optical transitions caused by photoexcitation, and scaling this rate with the probability of a photoexcited electron having momentum normal to the escape surface. Kane's paper deals primarily with the photoelectron yield versus energy curve near threshold for a general band structure by considering the possible photoelectric production and escape mechanisms involving bulk and surface states. His calculations are based on density of states considerations and involve energy band Taylor expansions to the lowest non-vanishing order about the threshold point. Escape conditions, that the excited state must have a k vector component normal to the escape surface and any k vector tangential to the escape surface is conserved, define the possible values of k, an effective escape solid angle, for electron emission. The rate of optical transitions is calculated with Fermi's Golden Rule as described previously. The quantum yield is thus determined by dividing the sum of the rate of transitions over k space that satisfy the escape conditions by the sum of the photon absorption over one Brillouin Zone.

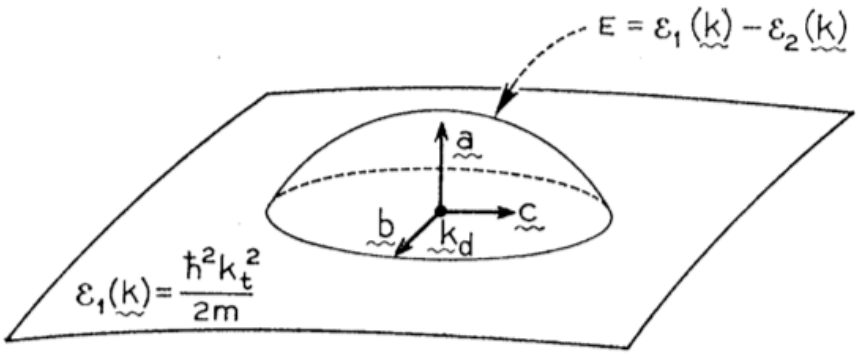

FIGURE 2.3: Intersection of the 'optical surface' and the 'escape surface' from [67]. The region bound by these surfaces contain the k values for which the probability of excitation may be calculated. As electron energy E decreases, the circle of intersection shrinks to k_d, the momentum corresponding to photoelectron emission threshold energy.

If the escape condition is written as

$$E_{ESC}(k) = \frac{\hbar^2 k_n^2}{2m} \tag{2.8}$$

and the energy conservation relation is

$$h\nu = E_f(k) - E_i(k) \tag{2.9}$$

equations 2.8 and 2.9 can be combined to define a photoelectron escape surface, as shown in Figure 2.3 (where $E_f(k)$ and $E_i(k)$ are the final and initial photoelectron energies respectively, and $k_n = k_t$).

At the threshold (E_d), the two surfaces are tangential at the point k_d in k-space. Expansions about this point k_d lead to expressions of possible values of k that result in photoelectron emission for small energies above E_d. Kane included a number of possible factors that would affect the optical and escape surface and thus the yield near threshold. Inelastic scattering of photoexcited electrons leads to redistribution in k-space after excitation, thus lowering the threshold E_d, but decreasing the total quantum yield. He also attempted to include effects due to indirect optical transitions in the bulk and surface, and surface roughness. Taylor expansions of the yield as a function of excited electron energy near threshold lead to a sum of products of constant transition probability (slowly varying in energy) and the energy difference $(h\nu - E_d)^n$. The value

of n was determined by whether the emission was dominated by factors including direct or indirect optical excitation originating from a bulk or surface defect, or intrinsic band states. The energy term in the Taylor expansion with the largest coefficient governs the relationship between yield and photon energy and hence the value of n applied to the relation

$$Y(h\nu) = C(h\nu - E_d)^n \tag{2.10}$$

Kane's results were used experimentally to both identify the excitation and scattering mechanisms of solids and surfaces, and to determine the photoelectron emission threshold with precision when the mechanisms were known. However, there was some ambiguity about the results (n was found to be 1, $^3/_2$, 2 and $^5/_2$, and in some cases the relation was unable to differentiate between combinations of emission processes e.g: both direct excitation of surface band states and elastically scattered indirect excitations from bulk states were indistinguishable) and the theory was incomplete as it had not considered energy loss due to inelastic scattering effects.

In 1971 at Stanford University, Ballantyne published a model for the photoelectron emission yield near threshold [55] based on Kane's work but included effects of energy loss due to phonon scattering. The effect of phonon scattering (θ_{ph}) was incorporated into the model using a continuous energy loss term scaled by the distance of an electron from the surface, z, which is given by the reciprocal of the optical absorption coefficient $\alpha_{h\nu}$

$$\theta_{ph} = \frac{E_{ph}}{\alpha_{h\nu}\lambda(E)} \tag{2.11}$$

where E_{ph} is the average energy lost per phonon scattering event and $\lambda(E)$ is the energy dependent mean free path for phonon scattering. Ballantyne's models provided good fits to existing data, and proved simpler and more consistent than Kane's results. Ballantyne's expressions for the photoelectron emission yield near threshold are used to this day to precisely determine the value of the photoelectron yield threshold [57, 68, 69]. His results are in the same form as Kane's, but show that the yield is proportional to

Case	Energy dependence of yield[a]
1(a) Direct transitions with quasi-elastic scattering and energy loss, final states at threshold not at an extremum in conduction band	$\frac{\alpha(h\nu)}{(h\nu)^2\epsilon_2(h\nu)}(h\nu - h\nu_s)^3$
1(b) Nondirect transitions when excited distribution is rectangular, with energy loss to quasielastic scattering	$\frac{\alpha(h\nu)}{(h\nu)^2\epsilon_2(h\nu)}(h\nu - h\nu_i)^3$
1(c) Most semiconductors	Same as 1(a) or 1(b)
2(a) Direct transitions with quasi-elastic scattering but no energy loss, final states at threshold not at an extremum in conduction band	$\frac{1}{(h\nu)^2\epsilon_2(h\nu)}(h\nu - h\nu_s)^2$
2(b) Nondirect transitions when excited distribution is rectangular but no energy loss to quasielastic scattering	$\frac{1}{(h\nu)^2\epsilon_2(h\nu)}(h\nu - h\nu_i)^2$
2(c) Most metals	Same as 2(a) or 2(b)
3 Indirect transitions only, with quasielastic scattering and energy loss, final states at threshold not at an extremum in conduction band	$\frac{\alpha(h\nu)}{(h\nu - \Delta\mathcal{E})^2}(h\nu - h\nu_i)^{7/2}$
4(a) Direct transitions, no quasielastic scattering	$\frac{1}{(h\nu)^2\epsilon_2(h\nu)}(h\nu - h\nu_d)$

FIGURE 2.4: Summary of Ballantyne's results for the threshold determination of PES from semiconductors and metals [55]. Notably, the yield from most semiconductors was predicted to increase linearly with the cube root of incident photon energy, and the yield from most metals was predicted to increase linearly with the square root of incident photon energy.

$(hv - E_d)^n$ where n=2 or 3 in most cases. A summary of his results is shown in Figure 2.4. Note that he summarises that most metals and most semiconductors have a $Y(hv)^{1/2}$ and $Y(hv)^{1/3}$ energy dependence respectively.

In practice, yield data collected from PYS is processed by calculating the square or cube root of the yield at each hv increment, which produces a linear curve that can be extrapolated to the background signal. The intercept of the linear fit and the background is the threshold energy, which is the depth of the highest initial energetic positions

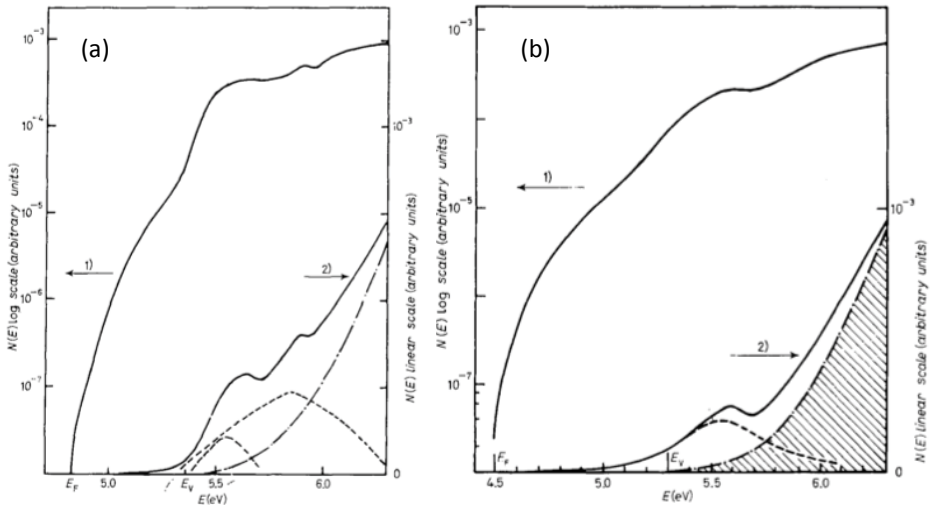

FIGURE 2.5: Density of states derived from PYS data on the Si (111) 2×1 reconstructed surface. The solid lines represent the total density of states and the dashed lines represent densities of individual states. Trace 1) is plotted against the logarithmic axis on the left and trace 2) is plotted against the linear axis on the right. The spectra revealed the presence of inter-bandgap, dangling bond states at the Si surface.

of photoelectrons within the material. This value is frequently assigned to the work function, ϕ, in metals and the ionisation potential, ζ, in semiconductors.

2.5 Surface characterisation

PYS has been an important tool for characterising surface phenomena such as band bending, negative electron affinity (NEA), and inter-bandgap defect states of semiconductor materials. It was used extensively in the late 1970s to thoroughly characterise these properties of Si, Ge and III-V compounds [60–62, 70–72]. Notably it was used to identify the energetic position of dangling bond surface states on the Si (111) 2 × 1 reconstructed surface and the effects of oxygen adsorption on the type and concentration of surface states [73]; to characterise the formation of negative electron affinity [74]; and to study the diffusion length of carriers in negative electron affinity diamond [75].

The first experiments carried out to study the effect of oxygen absorption on passivation of intrinsic surface defect states in Si were performed with PYS. Experimental results from Si (111) 2 × 1 are shown in Figure 2.5 [73]. Figures (a) and (b) are the effective density of states on both a logarithmic scale (left axes) and a linear scale (right axes) of the Si (111) 2 × 1 surface. The broken lines show the surface and bulk contributions to the effective density of states. In these cases, the work function corresponds to the

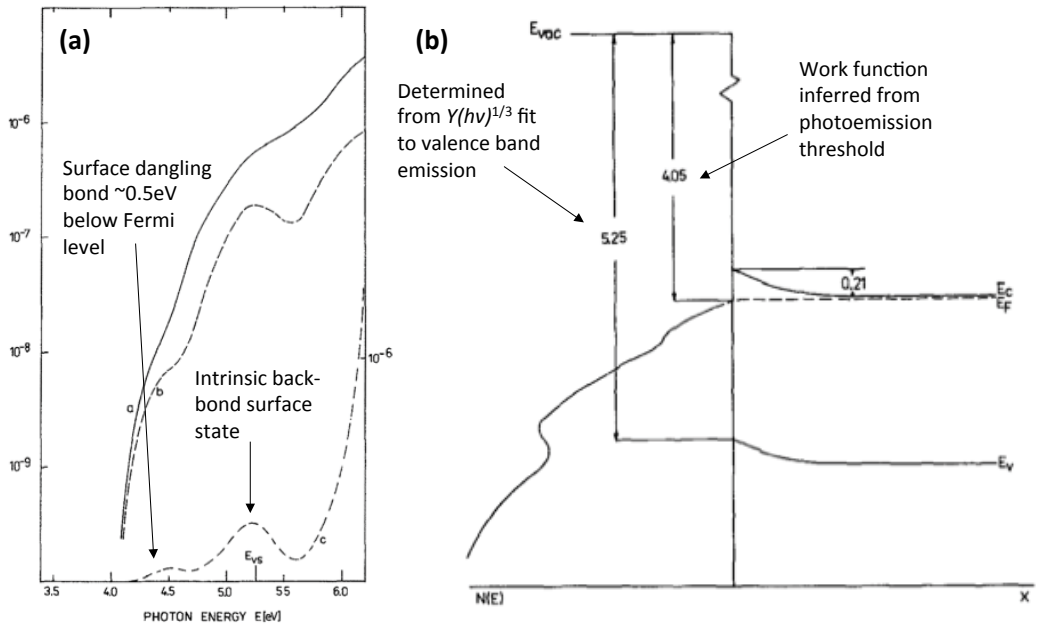

FIGURE 2.6: Comparison between PYS data and the electronic band structure it represents. (a) PYS spectra of GaAs(111): the solid line is the photoelectron yield and the dashed line is the derivative of the yield which represents the density of states. The lower dashed line is the derivative plotted against a linear vertical axis (right side). (b) the derivative of the yield plotted on a band diagram to highlight how energetic positions correspond to photoemission thresholds [70].

photoelectron emission threshold value, determined by the onset of electron emission from the logarithmic plot. This emission from the Fermi level indicated that there were filled inter-bandgap states at the surface. The clean Si (111) 2×1 surface in Figure 2.5 (a) exhibited two surface states, centered at 0.7 eV and 1.05 eV below the Fermi level, attributed to steps and dangling bonds of terrace atoms respectively. The ionisation potential ($\xi = E_{VAC} - E_V$) was found by fitting a linear section to a cube root plot after a secondary photoemission threshold marking the onset of emission from the valence band. It produced such precise results because the signal to noise ratio of the collected photocurrent was greater than five orders of magnitude. This extreme sensitivity enabled the extraction of accurate information about filled electronic states from the yield curves.

The effective density of states (that is revealed in the energy distribution curves of UPS and XPS) is given by the first derivative of the photo-yield, $Y(h\nu)$, with respect to photon energy [6, 60, 70]. A schematic of the relationship between PYS spectra and density of initial photoelectron states is shown in Figure 2.6 (b).

PYS was applied to a hydrogen terminated and clean reconstructed (001) IIa diamond to characterise electron emission properties over the spectral regime 4 to 7.5 eV [75,

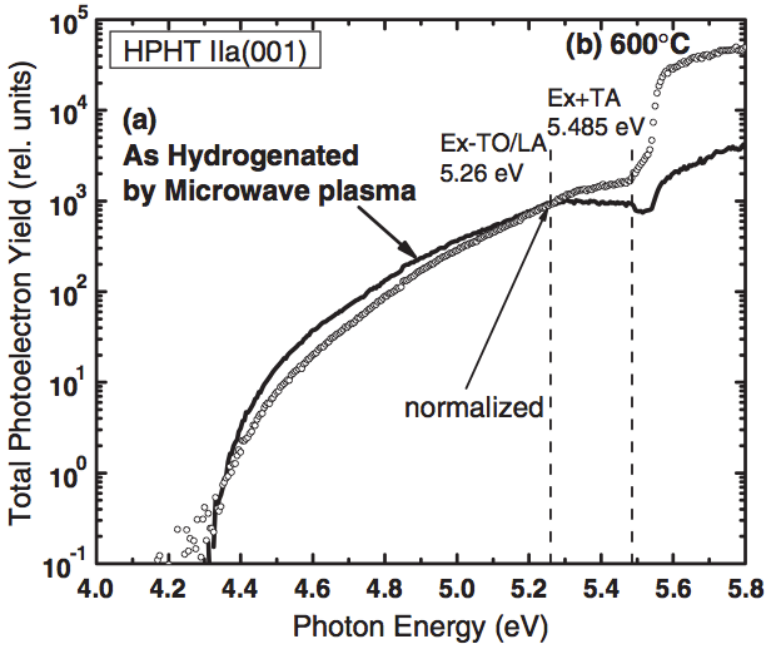

FIGURE 2.7: PYS spectra from Ristein et. al. showing photoelectron emission from inter-bandgap states at 4.4 eV, and enhanced photoelectron emission strength for NEA diamond attributed to exciton-phonon induced free electron generation at 5.485 eV.

76]. The results, shown in Figure 2.7, indicate that the PYS threshold at 4.4 eV, as detected on undoped, n- and p-type diamond is due to direct photoexcitation of valence band electrons into the vacuum level which is 1.1 eV below the conduction band minimum. Partial removal of hydrogen from the surface results in a decrease of the negative electron affinity from 1.1 to 0.9 eV. Annealing experiments also show that the surface band bending is a significant barrier for conduction band electrons. After thermal annealing at 700 °C the barrier vanishes and the amplitude of emission rises by two orders of magnitude, revealing contribution due to exciton-phonon induced free electron generation. Finally, after complete hydrogen evaporation, the electron affinity becomes positive. Taking into account the energy dependent properties of PYS spectra, an electron affinity of + 1.17 eV was calculated for the clean (001) diamond surface.

Novel photoelectron yield experiments performed with a dynamic range of 8 orders of magnitude (shown in Figure 2.8) revealed a new excitation channel for electron emission from diamond (100) and (111) surfaces with negative electron affinity, which was attributed to defect states 2.0 and 4.1 eV below the conduction band minimum. Additionally, Ristein et al. were able to employ photoelectron emission yield spectroscopy as a means of determining the conduction band electron diffusion length in hydrogen terminated diamond [75]. This was a particularly clever application of the technique, as

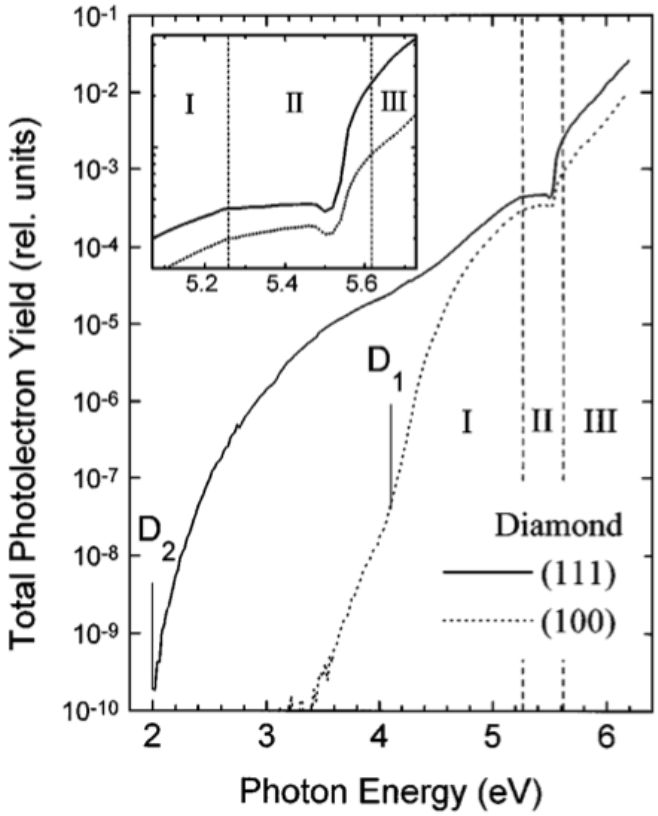

FIGURE 2.8: PYS spectra from Ristein et al. of single crystal type IIb diamond (111) and (100) surfaces after exposure to hydrogen plasma [75]. The sharp increase at 5.54 eV marks the exciton absorption edge, and confirms a NEA.

the photoelectron emission probability does not typically depend on electron diffusion lengths, but rather the electron thermalisation length.

After photoexcitation, electrons in the conduction band of a semiconductor will dissipate their excess kinetic energy by inelastic scattering with other electrons and phonons. This thermalisation process takes place on a subpicosecond time scale and within a spatial range corresponding to the thermalisation length of the order of 100 nm. In the case of positive electron affinity (PEA), thermalised electrons at the conduction band minimum (CBM) are lost from the photoelectron emission current since they are not able to overcome the energy barrier, the electron affinity χ, at the surface. The probe depth of the total yield technique is thus limited by the thermalisation length. As long as the reciprocal of the absorption constant α is greater than the thermalisation length - which is a valid approximation near the absorption threshold - most of the photoexcited electrons will not contribute to the photoelectron current.

However, the situation is different for surfaces with negative electron affinity (NEA).

Thermalised electrons will now also contribute to the photoelectron emission current and electrons are only lost by recombination which takes place on a microsecond time scale depending on the concentration of deep defect states acting as recombination centres. The escape depth is no longer limited by the thermalisation length but instead by the much longer diffusion length L of the electrons. The photoelectron yield will be correspondingly higher than in the case of NEA. The total yield measured at a photon energy hv is defined as the ratio of the photoelectron current divided by the photon flux incident on the sample (and corrected for reflection losses). For a photon flux density j_0 an excitation as a function of depth into the sample z take the exponential form

$$P(z) = j_0 \alpha_{hv} e^{-\alpha_{hv} z} \tag{2.12}$$

Applying the properties of NEA surface discussed above, an expression for the propagation factor $T(z)$ of photoexcited electrons, was developed

$$T(z) = \frac{S_{EM}}{S_{EM} + S_{REC} + L^{-1}D} e^{-L^{-1}z} \tag{2.13}$$

where S_{EM} is a surface transition probability, S_{REC} is a recombination probability and D is the electron diffusion coefficient. Using the excitation probability profile and propagation factor of equations 2.12 and 2.13, Ristein et al. developed an expression for the photoelectron yield normalised to incident photon flux [75]

$$Y(hv) = \frac{p \cdot L \cdot \alpha_{hv}}{1 + L\alpha_{hv}} \tag{2.14}$$

where p represents the prefactor of the exponential in equation 2.13. This formalisation is only applicable to surfaces with a NEA, but by quantitatively characterising the incident photon flux, and measuring the corresponding photoelectron yield, they were able to calculate the diffusion length of conduction band electrons in diamond.

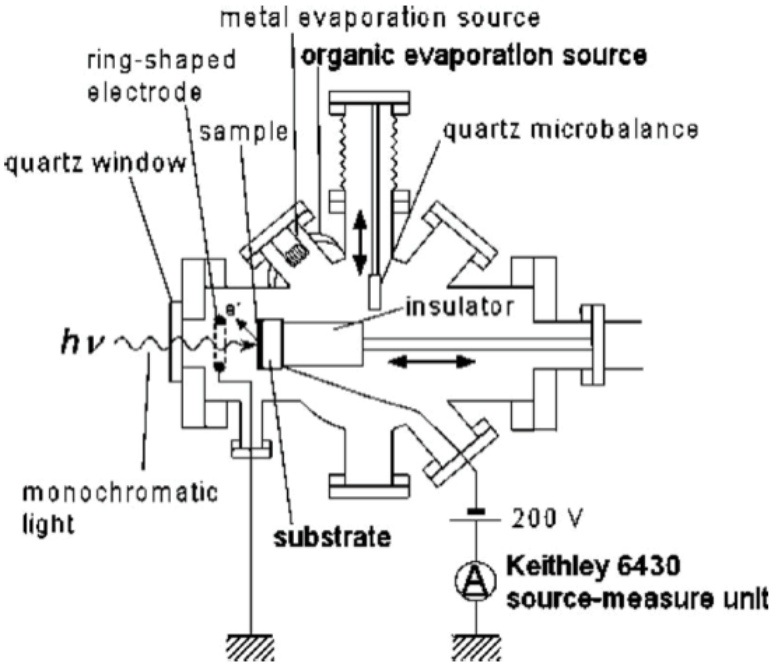

FIGURE 2.9: Experimental setup of an atmospheric PYS system developed by Honda et al. [57].

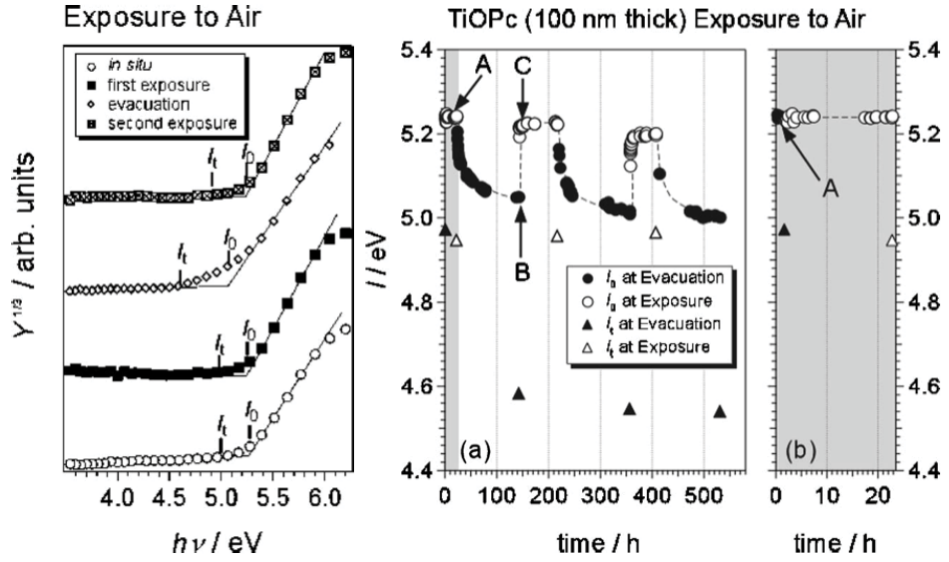

FIGURE 2.10: Atmospheric PYS spectra of Phthalocyanine films upon repeated exposure to air and evacuation of the vacuum chamber. Honda et al. identified two separate photoelectron emission thresholds, and observed an increase in the ionisation potential upon exposure to air [57].

2.6 Atmospheric photoelectron yield spectroscopy

Atmospheric PYS is a recently developed technique that employs a similar experimental setup to the PYS, but can operate at atmospheric pressure or in low vacuum environments due to the electron collection mechanism. The detectors used for these instruments are called "open counters", or thick gas electron multipliers, and consist of narrowly spaced parallel grids, between which Townsend gas cascades can be generated at atmospheric pressures. There are several papers that have reported using this technique [57, 77–80]. The collection mechanism is a gas cascade amplification process similar to that used in an EPYS. A high voltage electrode accelerates low energy electrons, causing ionisation of gaseous molecules, thus generating more low energy electrons and amplifying the initial current. This gas cascade process is described briefly in the following section, and a more rigorous derivation of a mathematical description of it can be found in Appendix A. Unlike EPYS, which operates in the range of 0.1-10 Torr, atmospheric PYS operates at atmospheric pressure, and has thus far not been used with gas species other than those found in air. In addition, these instruments have not included any temperature resolved capabilities, and are thus limited to investigating the effects of air on photoelectron emission from various materials.

Figure 2.9 shows a schematic of the atmospheric PYS system developed by Honda et al. [57]. They used the atmospheric PYS to study the ionisation potential of Phthalocyanine films upon exposure to ambient air. The ionisation potential was observed to increase upon exposure, as shown in Figure 2.10. Further, it was found that certain changes were reversible upon repeated exposure-evacuation cycles. However, there was also a slow irreversible decrease in the ionisation potential that occurred over time. These reversible and irreversible changes were attributed to physisorption and chemisorption respectively of molecules from the gas phase.

A final application of atmospheric photoelectron yield spectroscopy worthy of note is implementation of a commercial product named PESA (photoelectron spectroscopy in air) by Nakayama et al. [81]. This system employs an open-air electron counter developed in the 1990s as the electron collector in an atmospheric PYS setup [81, 82]. Spectra from several organic materials were collected in air. These spectra were used to determine the ionisation potential by use of the cube root law which is described in section 2.4.2, and the effective density of states by differentiation of the yield curve.

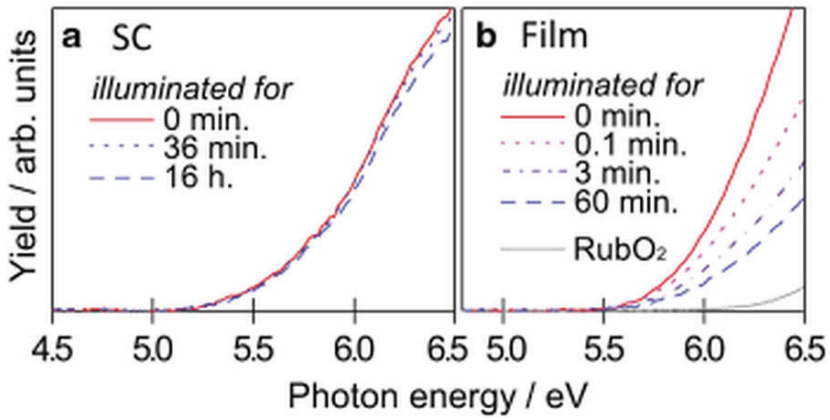

FIGURE 2.11: Atmospheric PYS spectra collected by Nakayama el al. showing an increase in the ionisation potential of single crystalline ruberene during photo-oxidation [81]. The increase in the ionisation potential was attributed to generation of polar oxide molecules and reversible physisorption of H_2O.

The technique has primarily been used to characterise the surface ionisation potential of organic semiconductors that are commonly used in optoelectronic device development. An example of the spectra gathered with this system is shown in Figure 2.11.

2.7 Townsend gas capacitance model

The Townsend gas capacitance model describes an exponentially increasing current-voltage relationship in a gaseous discharge between two plates [83, 84]. Amplification of gaseous charge carriers that occurs in EPYS can be approximated by Townsend's model. Theory relating to the Townsend gas capacitance model is found in standard text on ionised gases and gas discharge physics [83, 84]. Townsend's theories have been extended and improved to describe detection of electrons in environmental scanning electron microscopy (ESEM) [85–87] and are equally applicable to EPYS. Amplification and detection of backscattered electrons (BSE), secondary electrons (SE) and primary electrons (PE) have been studied and described over a range of pressure, detector biases, beam currents and sample-detector gap distances.

The theory models electron multiplication that occurs as electrons are accelerated under an electric field in the presence of gaseous molecules via electron impact ionisation. However, there are numerous collision processes and reactions that may occur in a partially ionised gas that are also capable of generating additional gas excitation phenomena or avalanche electrons. These phenomena include multiple ionisation events from which

two or more electrons are ejected from an atom or molecule [88]; generation of long lived meta states which de-excite and emit free electrons or photons [89]; and recombination reactions where positive ions (PIs) capture electrons and the excitation energy is released in the form of an auger electron or photon [83, 86, 90]. Cross-sections for these interactions play an important role in the amplification characteristics of gases because they determine amplification efficiency (α), optimal pressures for amplification and the maximum amplification achievable before the cascade becomes self-perpetuating and leads to discharge.

2.8 Limitations of existing knowledge

Photoelectron emission has been used extensively in the past to elucidate electronic properties of a wide variety of materials, using techniques that differ slightly in their excitation and electron detection methods. UHV techniques have demonstrated enormous utility for studying the surface electronic properties of materials, quantitatively revealing the energetic structure of defects and impurities, and the effects of such defects on intrinsic band structure. PYS has shown itself to be particularly apt for probing relatively low lying energetic states such as inter-bandgap defects, and conduction and valence band structure with very high spectral resolution. However, UHV techniques are unable to answer pressing modern questions about the processes that take place at solid-gas interfaces, which are arguably far more relevant questions in the context of solid state device development and technological progress.

The atmospheric PYS techniques that have been developed to begin bridging the pressure gap between UHV, ideal material properties, and the properties of materials in dynamic and gaseous environments are still limited in their capabilities. The EPYS developed as a part of this study is unique among other techniques in its ability to investigate in-situ and real-time, high pressure and temperature resolved material surface processes in reactive gaseous environments.

Chapter 3

EPYS development

3.1 Overview

The environmental photoelectron yield spectroscopy (EPYS) system is a completely unique, custom built instrument that has been developed to serve as a real-time characterisation tool for dynamic surface processes that occur in low vacuum environments. Each component of this system has been built from the ground up as a part of this project. The light and gas delivery systems were built specifically for this instrument. The sample stage has been machined in-house and the sample holder assembly including the heating element, electrical connections and liquid nitrogen feedthroughs have been developed and assembled as a part of this project. The photoelectron detector and EPYS signal output circuit were designed and built, and the measurement methodology and automation were developed in-house. The hardware has undergone many iterations before reaching a level of performance that allowed for implementation of the EPYS as an accurate and reliable scientific instrument.

This chapter details the hardware developed as a major part of this project, and describes the operational procedures of the EPYS instrument.

3.2 Introduction

The EPYS probes the surface electronic structure of the upper valence band, mid-bandgap defects and conduction band, and reveals the effects of adsorbate composition

and coverage on these properties. The system consists of a broadband UV light source (deuterium lamp) and monochromator; a vacuum chamber with gas delivery system; and a gaseous electron detector (GED). Monochromatised light is delivered through a chamber window onto the sample and incrementally increased in energy from 4 to 7 eV. At each increment the relative intensity of photoelectrons is measured with the GED.

Additional functionality has been built into the system by incorporating a temperature-controlled sample-stage, residual gas analysis, automated data collection, vacuum environment control and data analysis tools. The sections in this chapter detail the apparatus, function and methodology of each component in the system: the vacuum chamber; sample stage; detector; light delivery; gas delivery; and automation and control.

A photograph of the instrument and its components is shown in Figure 3.1. The light source and monochromator sit atop the system, feeding light through an optic fibre to the vacuum chamber. Precursor gas ampules and delivery lines with flow regulators are situated on the shelf that also holds the detector HV supply. The chamber itself is fixed to the primary bench with the TMP and backing lines extending from the opposite side, shown in Figure 3.1. The primary bench also supports the data acquisition board for measuring pressure and temperature and controlling gas flow rates; and the laptop used to control the monochromator and record gas cascade currents measured by the Keithley electrometer.

A series of more detailed photographs of the chamber is shown in Figure 3.2. Figure 3.2 (a) shows the back side of the chamber, where the TMP is located, and two flanges for a pressure gauge and nitrogen gas flow. The top of the chamber is shown in Figure 3.2 (b): electrical feedthroughs for applying voltage to the detector and measuring gas cascade current pass through the chamber lid; there is also a coaxial thermocouple flange that measures the stage temperature; the ambient gas inlet and a low vacuum manometer for monitoring pressure during operation. The optic fibre is held above the chamber window with a clamp, and its position can be adjusted according to sample position. The excitation light spot is shown in Figure 3.2 (c), and Figure 3.2 (d) shows the underside of the chamber lid with a gas injection needle positioned directly above where the stage sits, and a Teflon ring that holds the detector in place directly below the chamber window.

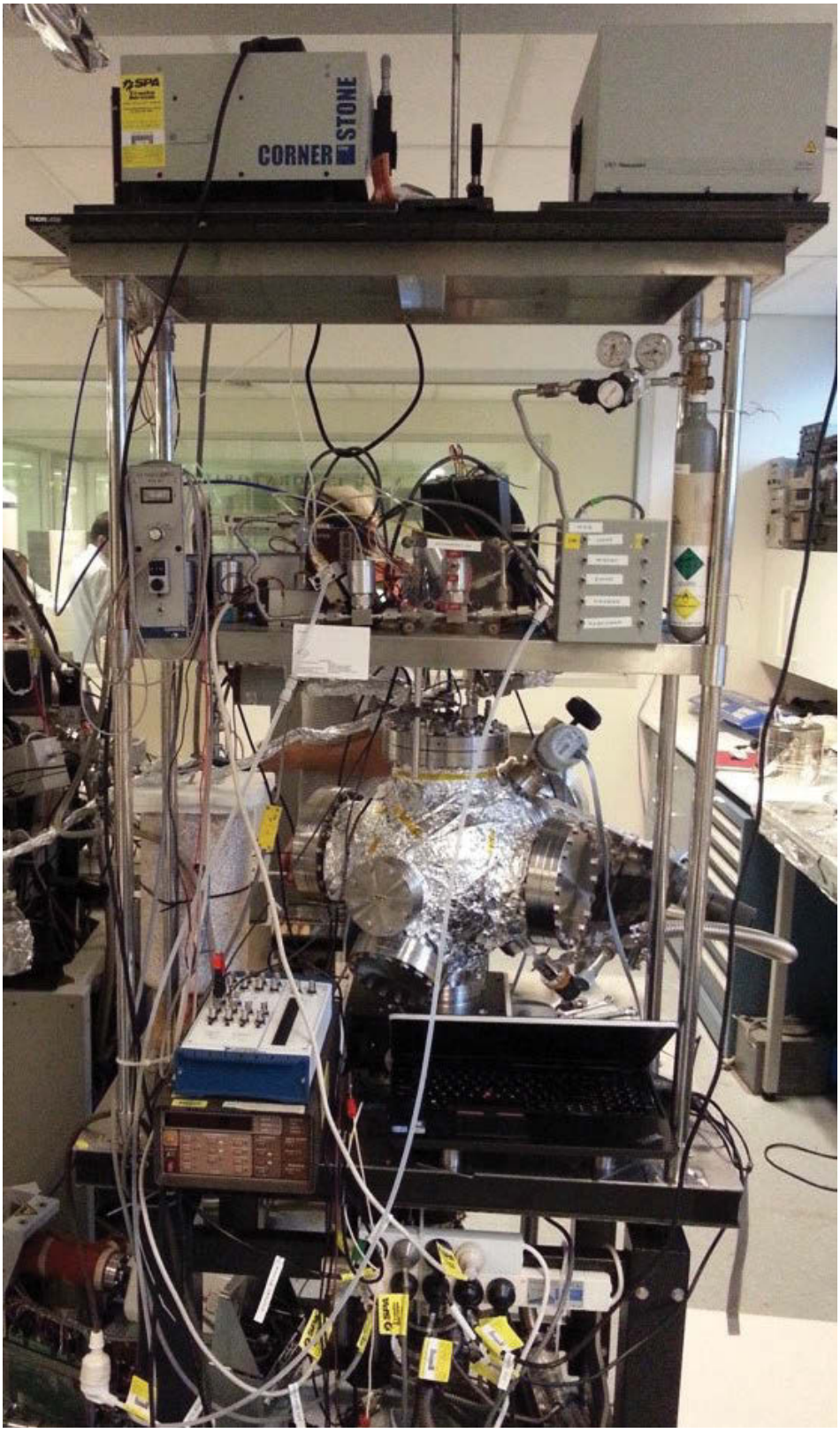

FIGURE 3.1: Photograph of the complete EPYS instrument.

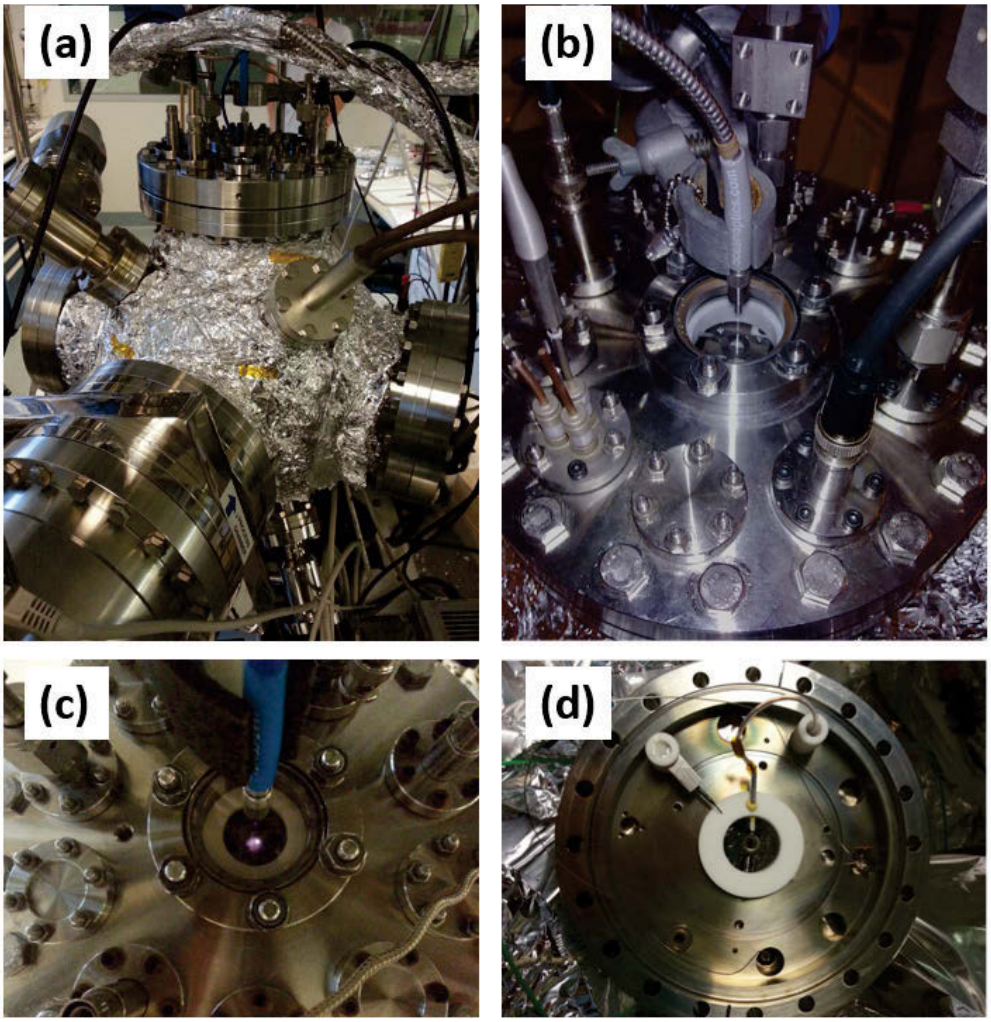

FIGURE 3.2: Photographs of the EPYS system showing: (a) The EPYS chamber, wrapped in foil to enable uniform heating of the inner side walls, with a TMP connected to the front 8" port and a variety of feedthroughs for electrical connections and gas delivery; (b) The top flange that hosts the majority of feedthroughs and a sapphire window that is positioned above the sample and detector; (c) Light being directed through the sapphire window onto the sample inside the chamber. The diameter of the irradiated spot is 5 mm; (d) The vacuum side of the top flange which consists of an annular GED held in place with a Macor ring and a gas injection needle pointing towards the centre.

During an EPYS measurement, the vacuum chamber is held at a constant steady state pressure in the range of 0.1 to 10 Torr by means of adjusting both gas delivery and pumping rate to achieve the desired net pressure and flow rate. Monochromatised light is directed through a sapphire window into the chamber in the desired wavelength increments over the range of 350 to 180 nm (3.54 to 6.88 eV respectively). When the energy of incident light is sufficient for a sample-bound electron to surmount the energetic solid-vacuum interface barrier, photoelectrons may be liberated from the sample, and accelerated towards a detector anode.

The photoelectrons are accelerated under the influence of an electric field set up by the detector anode, held at approximately 500 V and at a distance of approximately 15 mm from the sample surface (roughly 33.3 $V.m^{-1}$). As the photoelectrons gain enough kinetic energy within their mean free path to ionise gaseous molecules between the sample and anode, collisions produce additional free electrons that amplify the initial photoelectron current. The positive ions produced during this process drift towards the grounded sample stage where they recombine, thus producing a current that is proportional to the total number of photoelectrons initially emitted from the sample. This positive ion current is measured with an electrometer as a function of photon energy.

EPYS is only able to interrogate continuous electrically conductive surfaces, and the irradiated area must have electrical contact with the stage. Emission of photoelectrons from the sample leads to a positive charge build up if bulk electrons are unable to replenish the surface rapidly. Charge build-up reduces the potential difference between the sample and detector, leading to decreased field strength. A varying field strength causes the photoelectron amplification factor to change, so that relative photoelectron currents are not proportional, and spectral shapes are no longer representative of the true electronic structure. Charge build-up can also result in fluctuations of the gas cascade that increases electrical noise in the measured ion current

It is difficult to characterise porous films and powders due to spurious photoelectron emission from the substrate layer contributing to the photoelectron current. These types of samples must be prepared on an insulating substrate that will not emit photoelectrons at the photon energies used. In addition, they must be densely packed to form an electrical path across the surface to where contact may be formed with the stage.

3.3 Vacuum chamber

The main EPYS chamber is shown in Figure 3.3. The spherical vacuum chamber is connected to the gas delivery and pumping system. It has electrical feedthroughs for the detection system and sample temperature control, and a sapphire window through which excitation light is passed. The pumping system consists of a series of roughing scroll pumps and a Pfieffer turbo molecular backing pump (TMP). A base pressure of 1×10^{-8} Torr is reached after pumping the closed chamber for several hours. The

FIGURE 3.3: Photograph of the (a) back and (b) front of the EPYS chamber.

pumping rate can be controlled over a higher pressure range by closing a gate valve to the TMP and pumping the chamber through a variable flow valve with the roughing pump.

Heating cables blanketed with foil keep the chamber at approximately 50°C to increase the desorption rate of residual contaminants from the chamber walls and hence pumping efficiency. Gas can be delivered through a variable flow control valve into the chamber via a gas injection needle. The gas injection needle (shown in Figure 3.2 (d)) is positioned above the sample stage to ensure maximum exposure to, and replenishment of, gaseous atoms and molecules.

A schematic of the inner chamber is shown in Figure 3.4 with its various components. A sample stage is positioned at the top centre of the vacuum system and electrically isolated from the chamber. The stage is heated by a ceramic joule heating plate from beneath, and contains a bore through which cooled nitrogen gas can be fed. The heater is controlled with a current source outside of the chamber and can reach temperatures up to 900°C. The stage can be cooled to -190°C by passing cold nitrogen gas through it. The temperature is monitored by a platinum resistance thermometer encased in a ceramic cylinder to avoid forming electrical contact with the stage. A wide range gauge (WRG) and a 10 Torr capacitance manometer are used to monitor the chamber pressure at high and low vacuum respectively. The sample is clipped to the stage and sits directly beneath the GED, and a gas injection needle is positioned to guide gas into the sample-detector gap. Light is delivered from an optic fibre through a chamber window and the

centre of the detector to the sample. Current amplified by cascading photoelectrons is measured through the sample stage with a Keithley electrometer outside of the chamber.

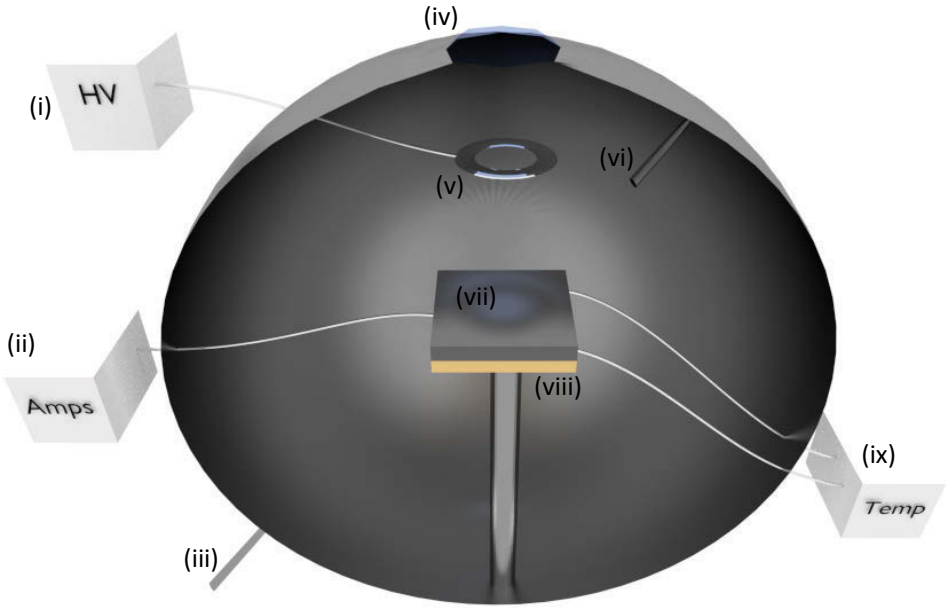

FIGURE 3.4: Schematic of the EPYS system showing: (i) a high voltage power supply connected to the detector; (ii) a Keithley electrometer that measures the current through the sample stage generated by the cascading photoelectrons; (iii) the controllable-flow pumping outlet for operating in low vacuum; (iv) the chamber window through which UV light is passed to the sample; (v) the detector; (vi) the controllable flow inlet from gas delivery lines; (vii) the sample stage, electrically grounded through the electrometer; (viii) the sample heater; and (ix) the current supply for temperature control.

The 304 stainless steel chamber shown in Figure 3.5 hosts four 8", two 6", one $2\frac{3}{4}$", and three $4\frac{1}{2}$" CF flanges. The TMP is mounted on a 8" side flange that can be isolated with a gate valve and bypassed to the scroll pump through a needle valve mounted on a $2\frac{3}{4}$" flange. Another $2\frac{3}{4}$" flange is used interchangeably to supply nitrogen to the cold stage or to pump residual gas to a mass analyser for compositional analysis. A stage holder that can be translated in three dimensions, rotated and tilted is mounted on the bottom $4\frac{1}{2}$" flange. The chamber lid is mounted on the top 8" flange, and contains two electrical feedthroughs to supply a voltage to the detector and to measure the current flowing through the stage; a gas feedthrough that leads to the gas injection needle; a port for a 10 Torr capacitance manometer and the sapphire window above the sample and detector. One 6" port is used for electrical feedthroughs that control and measure the temperature of the heating plate beneath the stage, and one $2\frac{3}{4}$" flange holds a wide range gauge monitoring high vacuum pressure.

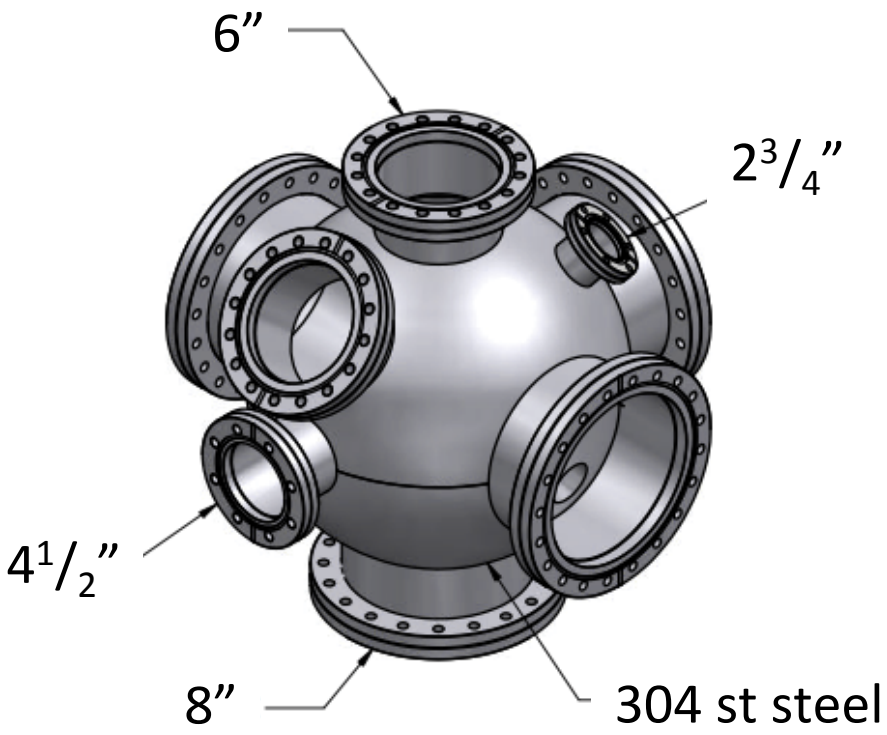

FIGURE 3.5: Schematic of the chamber used in the EPYS instrument.

3.4 Sample stage

The sample stage (50 x 30 x 10 mm) has been machined in-house from 316 stainless steel. Beneath the stage is a boroelectric joule heater. The heating and sample stage assembly is held inside the vacuum chamber atop a translating and rotating mechanical feedthrough that is able to position the sample holder assembly in x, y, and z dimensions. The ability to position the stage serves several purposes: one is the ability to optimise the gas cascade amplification by translating the stage in the vertical direction; a second is to allow loading of multiple samples to be analysed (the excitation source and detector is static); and, thirdly, it allows the stage to be moved far away from sensitive components for high temperature annealing.

The sample stage must remain electrically isolated except for a single connection to ground, as the current flowing through the stage is the output signal from the EPYS system. The grounding connection is a wire spot welded to the stage that passes to the air-side through a feedthrough in the EPYS chamber lid, and connects to a Kiethley electrometer. The grounding cable is insulated with ceramic beads to prevent shorting to the chamber walls or stray wires inside the chamber.

Two high-current carrying wires are connected to the boroelectric heater beneath the steel stage, and control the sample holder assembly temperature. These wires are also insulated with ceramic beads, and must be positioned so as to electrically couple as little as possible to the signal wire and the steel stage. For high temperature operation, the signal to noise ratio can begin to drop as electrical noise from the boroelectric heater current source (which is typically on the order of an Ampere) couples from these wires to the stage, and superimposes over the comparatively weak signal current (which is typically in the pA to nA range). The temperature is measured with a ceramic-encased platinum resistance thermometer (PTD) that is embedded into the steel stage. The insulated PTD probe extends 25 mm into the stage, and is 2.8 mm in diameter. the ceramic casing ensures electrical isolation and prevents surface modification of the sensor by exposure to gaseous environments.

The sample itself is held in position with steel clips that can be fastened to the stage. Care must be taken when aligning the excitation source not to irradiate the steel clips so as to avoid spurious photoelectron emission. For samples that are on an insulating substrate, such as powders, thin films and nanostructures, the steel clips also serve to form an electrically conducting pathway to the stage. This is important for optimising the EPYS signal, but also for preventing charge build-up which can reduce the gas amplification and result in discharge-related electrical noise.

A hole has also been bored through the length of the stage to flow cooled nitrogen gas. This allows cooling of the sample holder assembly to liquid nitrogen temperatures. Swage tube fittings have been welded to the bore hole that connect Teflon tubes carrying the cooled nitrogen gas. The tubes are fed into and out of the chamber across a gas feedthrough flange. The air-side tubing consists of an outflow tube that exhausts the nitrogen gas to the ambient air, and the tube carrying nitrogen into the chamber that passes through a dewar filled with liquid nitrogen. The temperature is monitored by the platinum resistance thermometer and controlled by regulating the nitrogen gas flow rate.

3.5 Detector

The detection system consists of an anode held at positive voltage in the range of +200 to +600 V above the electrically grounded sample stage. It is similar to a gaseous electron detector (GED) used in ESEM in that the influence of its electric field on low energy electrons at the sample leads to the formation of a gas cascade. The gas cascade linearly amplifies the initial electron population generating a proportional number of positive ions that recombine with the stage (theory of the cascade is discussed more thoroughly in Section 3.6). The measured quantity is the positive ion current generated by the cascade, and is proportional to the photoelectron current.

The amplification factor depends on environmental conditions such as the sample-detector gap distance, detector voltage, pressure and gas type or mixture, and thus would require calibration with a known number of electrons to be quantitatively determined. Within a steady state environment, however, the amplification will remain constant and directly proportional to the initial photoelectron population. The positive ion current can therefore be used to qualitatively determine photoelectron thresholds and to analyse the lineshape of spectra in terms of the initial energetic positions of photoelectrons.

The final configuration of the detector is a 316 stainless steel annulus - shown in Figure 3.6 - supported approximately 15 mm directly above the sample by a Macor ring. The Macor ring is held in place below the chamber window and also serves to insulate the detector from the chamber lid. Multiple variations on the sample-detector geometry were implemented to identify the optimal form and position of the detector. These included rectangular plates and pin-head detectors held by ceramic rods attached to the stage and Teflon push-fit rings attached to the chamber lid. These geometries were found to be more or less suited to different environments. A pin-head detector operated more efficiently at higher pressures due to a pinching of electric field lines about the pointed end which leads to greater amplification close to the anode, and decreases the feedback by dispersing positive ions further from the irradiated spot. A rectangular plate proved to be stable at lower pressures and was particularly practical when interrogating multiple samples; however, its off-axis position led to lower collection efficiency. The annular geometry was selected because of its collection efficiency and amplification stability in

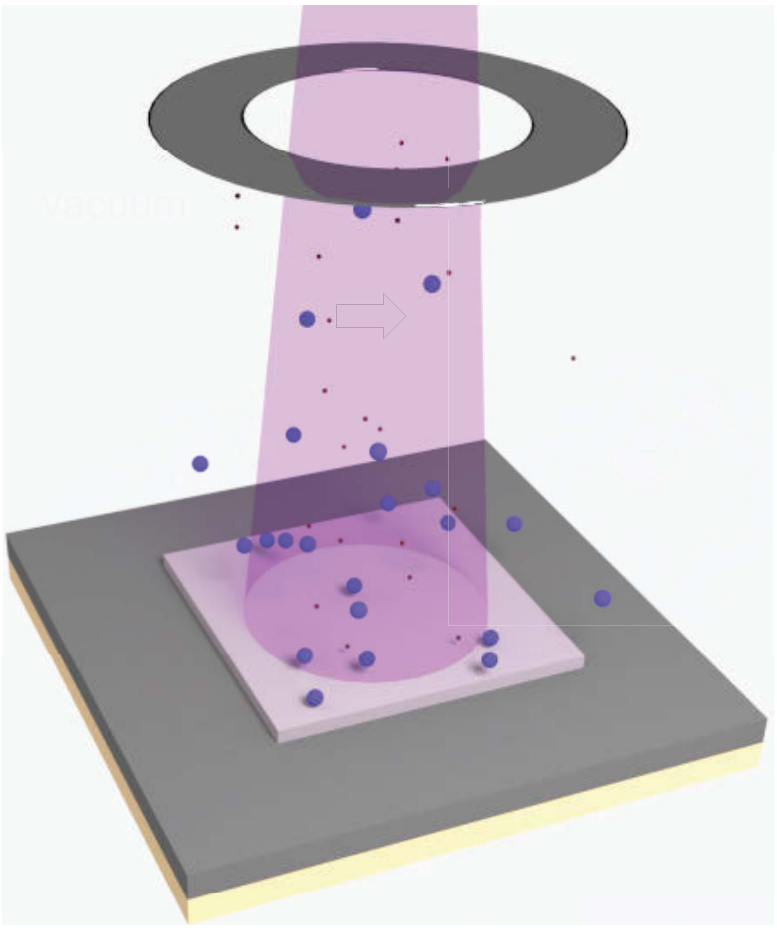

FIGURE 3.6: Diagram of the EPYS detector-sample geometry with the excitation source directed through the centre of the detector, onto the sample. Neutral gas molecules between the sample and detector are ionised by photoelectrons moving under the influence of an electric field.

the range of 0.5 to 5 Torr, due to the uniformity of field lines between the sample-detector gap surrounding the irradiated spot.

The quality of data gathered with EPYS depends largely on the signal to noise ratio. The signal depends on the photoelectron emission yield of the sample surface, the number of incident photons and the amplification efficiency of the gas, and can vary significantly. The positive ion current measured by the electrometer is subject to electrical noise induced by a number of sources. The stage heater can contribute significantly to electrical noise in the sample stage and can engulf weak signal in a poor amplifying gas at temperature in excess of 300 °C.

Other sources of electrical noise overlaying the positive ion current include: the influence of stray electric fields on current passing through the cabling outside the vacuum chamber; amplified shot noise of the photoelectrons and shot noise in the gas cascade itself;

noise associated with poor electrical contact from the sample to stage, stage to grounding cable, and grounding cable to chamber feedthrough; charging effects in poorly conducting materials; piezo/triboelectric effects in the cables to the electrometer and mechanical vibrations caused by operating vacuum pumps. The noise level during measurements at room temperature is approximately ±20 fA. Reducing this noise may require building air-side shielding for cables, and using high quality electrical contact material such as gold.

3.6 Light delivery

Excitation light from a deuterium lamp is monochromatised by a Czerny-Turner monochromator before passing through an optic fibre and the chamber window to the sample. A diagram of the light path from the source through to the optic fibre is shown in Figure 3.7.

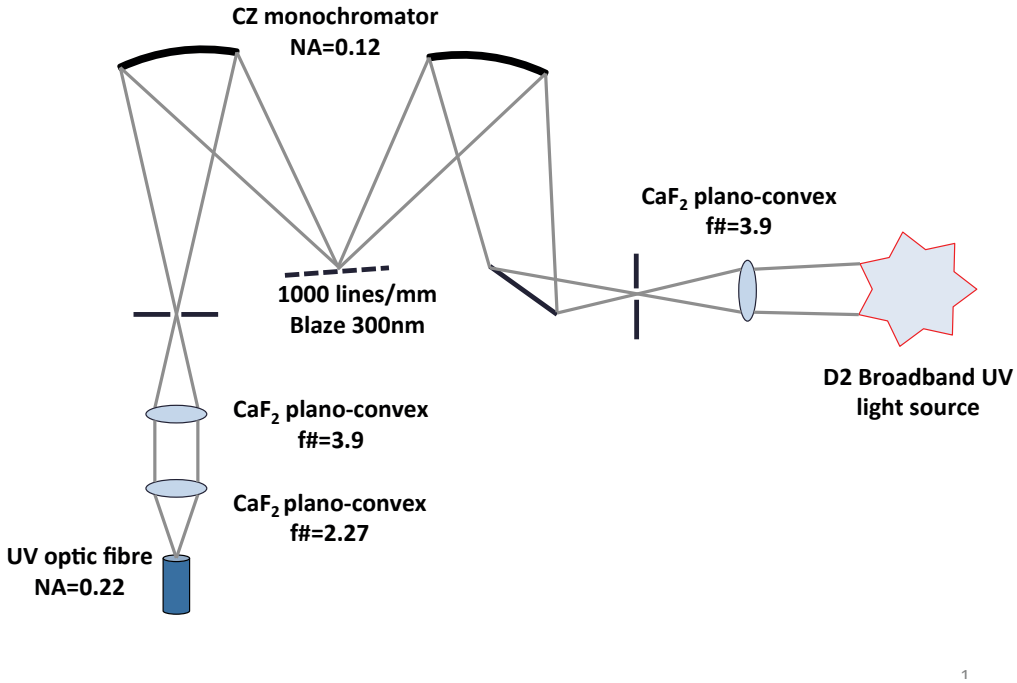

FIGURE 3.7: Diagram of the path of light from the deuterium lamp, focused into a Czerny-Turner monochromator with a CaF_2 lens, then collimated and re-focused with CaF_2 lenses onto the delivery optic fibre.

The number of photoelectrons generated per incident photon ($Y(h\nu)$) is constant for a given energy of light. Thus, the total number of photoelectrons generated increases linearly with the intensity of light reaching the sample. Therefore, ensuring maximal

transmission of light from the source to sample is necessary for increasing the EPYS dynamic range.

The light is generated by a 30 W deuterium lamp that produces a broad spectrum of light ranging from around 700 nm to 170 nm. The high energy limit of this light source corresponds to approximately 7 eV. For ensuring that the maximum amount of light available reaches the sample, careful alignment of the monochromator with the optic fibre at the exit aperture and collection of collimated light from the source into the entrance aperture of the monochromator is of great importance. Furthermore, selecting appropriate optical elements, including lenses, chamber window, monochromator grating and the optic fibre, that have high transmission in the UV range, is necessary. CaF_2 lenses have been selected as the focusing and collimating lenses for the EPYS system, while a 1 m SUV optic fibre is used to transfer light from the monochromator to the chamber window. The chamber window is a sapphire window that begins to absorb light below 180 nm, and the monochromator grating is blazed at 300 nm.

Second order peaks in the UV range also pass through the monochromator when scanning in the violet spectral range. This unintended UV transmission will cause a small amount of photoelectron emission to occur when scanning a low energy region of the EPYS spectra. To overcome these artefacts, a rotating optical filter wheel is attached to the exit aperture of the monochromator. The high-bandpass filter prevents transmission of light below 270 nm passing to the sample when scanning the range of 350 - 300 nm. Scanning across wavelengths shorter than 300 nm no longer requires the filter, as second order diffraction occurs at wavelengths shorter than what the deuterium lamp generates.

3.6.1 System response

As the total number of photoelectrons scales linearly with the intensity of light, the collected current measurements must be rescaled by dividing the current with the relative intensity of light at the corresponding wavelength. This correction factor (system response) is determined by collecting the spectrum of light after having passed through all optically absorbing/dispersing materials before reaching the sample. A photomultiplier tube (PMT) has been used to collect this spectra, which must also be corrected for its own response. The corrected EPYS system response is shown in Figure 3.8.

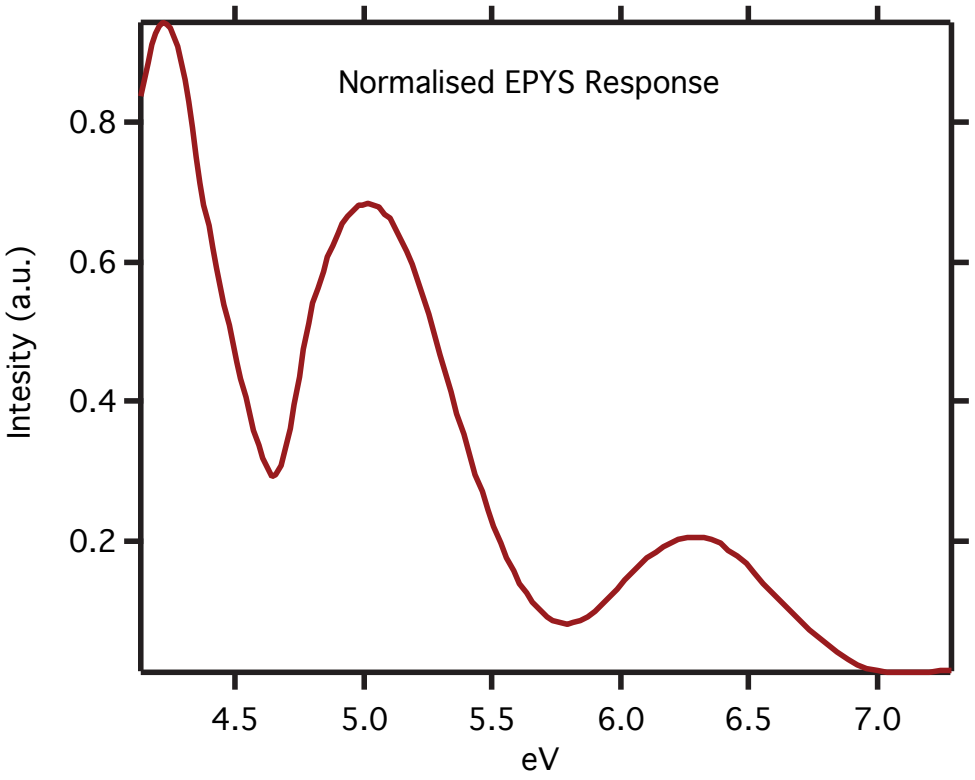

FIGURE 3.8: Normalised intensity spectrum of light that is incident on the sample.

There are a number of minima in the correction curve which are due to absorption of UV light by O_2 in the monochromator and the transmission efficiency of the optic fibre. These minima may be eliminated by flooding the monochromator with N_2 while operating, and removing the optic fibre by placing the exit aperture from the monochromator directly into the chamber window. However, due to the impracticality of effectively implementing such improvements, these steps to increase light transmission were not taken in this work.

3.7 Gas delivery

A steady state pressure is maintained by flowing gas into the chamber through a mass flow controller at 1-3 sccm, while pumping out through a needle valve that is manually adjusted to match the inflow at the desired pressure. The optimal pressure will depend on several factors including gas type (or gas mix), sample emission strength and sample-detector gap distance.

A diagram of the gas delivery system that was built specifically for the EPYS system is shown in Figure 3.9. Each gas source may be interchanged for a different species, but the existing setup caters for delivery of H_2O, C_3H_6O, H_2, Ar, O_2, N_2, NH_3 and NF_3.

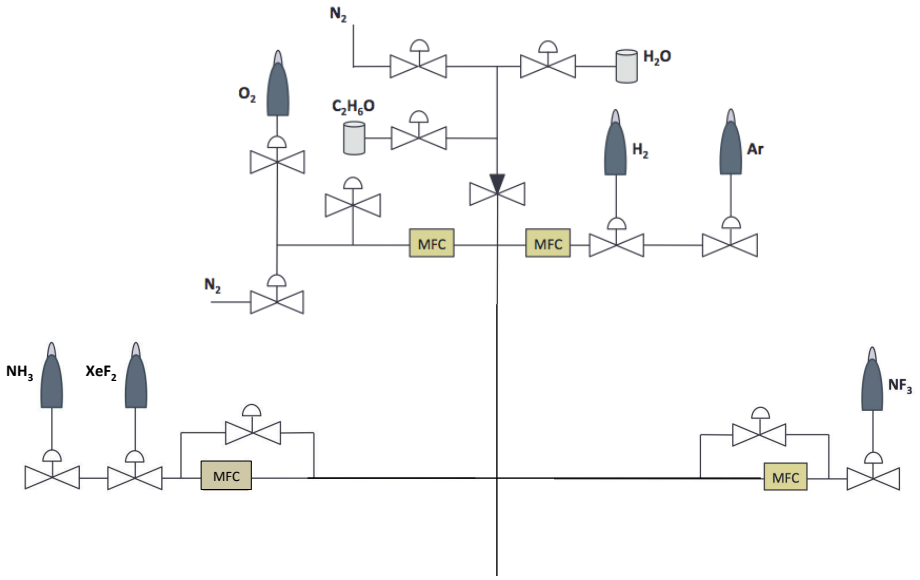

FIGURE 3.9: Diagram of the EPYS gas delivery system. MFCs are used to control the flow of pressurised gaseous sources, while a manual needle valve is adequate for liquid sources like H_2 and C_3H_6O.

3.8 Automation and control

LabView software developed previously to control a monochromator was modified to include automated scans and amplified photoelectron current reading at designated wavelengths. LabView programs were also developed in-house to monitor the temperature and pressure of the stage and vacuum respectively. A LabView PID controller using chamber pressure to regulate gas flow is used to maintain the desired dynamic pressure by increasing or decreasing the flow rate according to the difference between the desired and measured pressure.

A single EPYS measurement involves raising the chamber pressure of a specific gas or gas mix to the desired level, then irradiating the sample with monochromatised light (typically in 1 nm increments) from 350 nm to 170 nm, while a potential difference generated across the sample detector gap and current flowing through the stage is measured at each wavelength increment. A period of 1 second per wavelength interval is given to allow the cascade current to stabilize before a reading is taken.

Rotation of the monochromator grating takes an additional 0.5 seconds between intervals and a UV filter is rotated into place between 350 and 300 nm to prevent transmission of second order short wavelength peaks. The minimum time required to acquire a full spectrum is approximately 3.5 minutes. To increase the signal to noise ratio in spectra, the ability to perform multiple scans in an unchanging environment has been built into the control program so spectra may be combined in post-processing for effectively increased integration time.

For real-time characterisation of surface processes, spectra can be set to collect continuously while the sample temperature is slowly increased or decreased, or reactive gas species are introduced to the environment. Such experiments can take several hours to perform so it is desirable that the pressure is monitored and controlled automatically to prevent pressure drift.

Chapter 4

Application of EPYS: gas cascade amplification

4.1 Summary

This chapter demonstrates an application of EPYS to elucidate a feature of gaseous molecules that can be used as additional criteria for selection of appropriate gas species for high quality ESEM imaging. EPYS is used to identify that ethanol vapour (CH_3CH_2OH), used as an imaging gas in environmental scanning electron microscopy (ESEM), is superior to water vapour (H_2O) and ammonia (NH_3) in its ability to generate topological and electronic structure contrast. The cascade amplification of low energy electrons in the absence of primary and backscattered electrons is examined using EPYS, and it is proposed that ethanol achieves both higher breakdown currents and greater amplification in weaker electric fields because of its larger inelastic scattering cross section due to the group additivity rule. Considering the effect of molecular complexity on both ionising and non-ionising inelastic scattering processes also leads to a qualitative explanation for the optimum amplification pressure of different gas species.

4.2 Introduction

ESEM is a common tool for imaging insulating materials that accumulate charge during electron irradiation and cannot be studied using conventional, high vacuum electron

microscopy [86, 91, 92]. The use of different gas species has enabled ESEM studies of dynamic processes. For example, H_2O vapour, the most common ESEM imaging gas, can be used to study water droplet formation and the wettability of surfaces [93–97]; nanoparticle self-assembly during condensation [93–98]; humidity-induced swelling [99]; water transport through carbon nanopipes [100]; electrodeposition performed using aqueous liquid growth precursors [101, 102]; and chemical etching of carbon films, nanowires, nanotubes, graphene and diamond [103–107].

The most attractive feature of ESEM is the ability to image these processes in real time with SEM spatial resolution. However, the gas employed in ESEM plays a central role in secondary electron (SE) image quality, and wider applicability of ESEM is limited by the fact that only a handful of gases have favourable electron imaging characteristics. Numerous gases have been evaluated, including air, CO_2, N_2O, N_2, He [91] and NH_3 [106]. However, all of these except for NH_3 have been shown to be inferior to H_2O at generating high quality SE images. We note that SEs constitute one of a multitude of SEM imaging signals. However, SE imaging is the most common SEM imaging mode because it yields high resolution topographic contrast (on the order of one nanometer) [108, 109], and electronic structure contrast [110–112].

EPYS is used as a correlative characterisation technique to identify ethanol vapour (CH_3CH_2OH) as an excellent ESEM imaging gas. Quantitative ESEM measurements and complimentary quantitative EPYS [56, 57, 113] data is used to show that ethanol is superior to H_2O and NH_3, the only two high performance imaging gases reported to date. The superior imaging properties of CH_3CH_2OH cannot be explained by standard ESEM theory. The current model of ESEM imaging is improved to better account for the role of gas molecule size on electron image formation. The ability to image with ethanol is attractive because it paves the way to ESEM studies of dynamic phenomena such as the wetting behaviour of organic liquids and ethanol-water mixtures [114, 115], ethanol-based chemical vapour deposition [116–118] and catalytic reactions [119–121].

4.2.1 Gas amplification model

Low vacuum SEM uses a gas cascade current initiated by electrons to generate an image [122]. Primary electrons (PEs) and backscattered electrons (BSEs) contribute to the total cascade current; however, only the contribution from SEs (I_δ) supplies topological

contrast information [91, 123]

$$i_\Sigma = I_0 + I_\eta + I_\delta \tag{4.1}$$

where i_Σ is the total current measured across the sample-detector gap in ESEM while I_0 and I_η are the contributions initiated by PEs and BSEs respectively.

Image and electronic structure contrast is determined by the value of I_δ, which is difficult to measure directly with ESEM due to the presence of higher energy PEs and BSEs. However, it is quite simple to determine the value of $I_\delta + I_\eta$ (herein denoted by $I_{\delta+\eta}$) , which can be used as a guide for the study of gas amplification efficiency.

This value can be compared with the amplified photocurrent generated in EPYS (I_ξ), which is devoid of any contributions from high energy electrons, and directly measured as the positive ion (PI) current through the specimen stage.

$$I_P = I_\xi \tag{4.2}$$

Differences between the two values $I_{\delta+\eta}$ and I_ξ can be attributed to variations in the inelastic scattering cross-sections of each gas, which are a function of electron energy.

4.2.2 Positive feedback and breakdown

In the Townsend gas capacitance model, the breakdown current depends on the positive feedback coefficient of the imaging gas, k. Positive ions and neutral molecules can undergo collisions with the sample surface that eject an additional electron via an auger or photoelectron emission process [83].

$$I_\Sigma = i_\Sigma k = k(I_0 + I_\eta + I_\delta) \tag{4.3}$$

where I_Σ is the total cascade current due to contributions from all initial electrons and feedback ions. Considering the total number of electrons liberated from the sample by cascade generated ions and photons per ionisation collision in the gas (Second Townsend ionisation coefficient), γ, it may be shown the feedback amplification factor [91]

$$k = \frac{1}{1 - \gamma(e^{\alpha d} - 1)} \tag{4.4}$$

where d is the gap distance and $e^{\alpha d}$ is the cascade gain derived from the proportion of electrons produced (dN^-) to pre-existing electrons (N^-) at spacial increments in the beam axis ($dN^- = N^-(z)\alpha dz$) [83]. This feedback serves to increase the cascade current by generating additional electrons so long as the convergence criterion is met

$$\gamma^2(e^{\alpha d} - 1)^2 < 1 \tag{4.5}$$

When the gain becomes high enough for a single electron to initiate a cascade producing sufficient PIs that the probability of an auger or photoelectron being ejected equals 1, cascade breakdown and arcing occurs. For low γ, the gas cascade will sustain higher amplification, and hence I_δ, before the runaway feedback causes arc discharge.

4.3 Experimental methods

This study was focused on the gas cascade amplification characteristics of H_2O, ethanol and NH_3, and the sample used to generate secondary electrons and photoelectrons in ESEM and EPYS respectively was polycrystalline platinum foil. The foil was cleaned with an ultrasonicator in isopropanol, acetone and then water for 15 minutes in each solution then baked at 160 °C for 1 hour prior to loading into the ESEM and EPYS chamber.

4.3.1 ESEM

The gas cascade amplification efficiency of H_2O, NH_3 and CH_3CH_2OH was evaluated by measurements of the specimen stage current (see Figure 4.1 (a)) versus gas pressures and detector anode bias (which controls the electric field that drives the gas ionisation cascade), performed using a variable pressure FEI XL-30 ESEM. The electron beam energy current was fixed at 20 keV and 2.1 nA, and the sample-anode gap was 13.5 mm. A polycrystalline platinum foil sample and a Faraday cup were used to measure the total gas-amplified electron signal, and the component generated by amplification of the electron beam (before it strikes the sample surface), respectively. The difference between these two values is the gas-amplified electron emission current ($I_{\delta+\eta}$), which is initiated by secondary and backscattered electrons that are emitted from the sample.

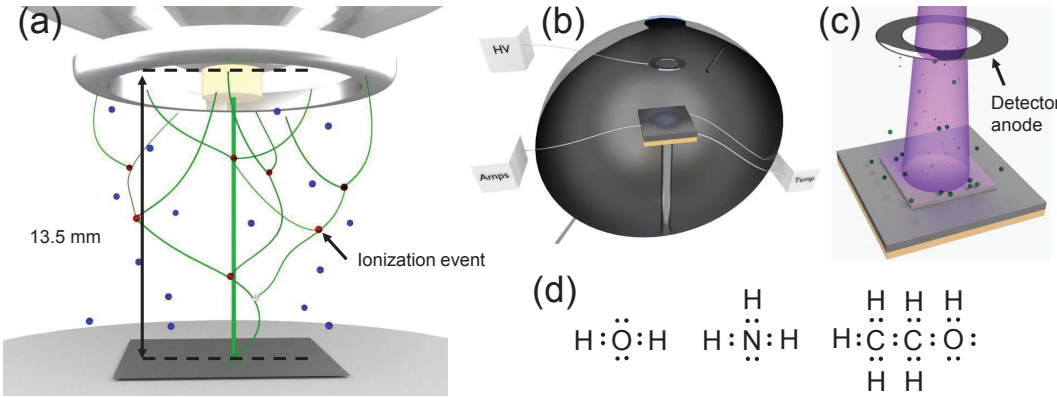

FIGURE 4.1: Schematic illustration of (a) an ESEM setup and secondary electron amplification in a gas ionisation cascade, (b) an EPYS vacuum chamber and (c) the EPYS measurement process. In both methods, emitted electrons are accelerated by an electric field between the sample and a detector anode, and are multiplied by ionising gas molecules. The EPYS chamber consists of a pumping system (not shown), gas inlet and outlet, specimen stage, heater, gas cascade detector, and an optical window. (d) Shows Lewis diagrams representing the number of valence electrons contributing to the interaction cross sections of H_2O, NH_3 and CH_3CH_2OH

Firstly, $I_{\delta+\eta}$ was determined in ESEM for each gas over the range of pressures 0.1-10 Torr (shown in Figure 4.2 (a)). Secondly, amplification as a function of detector bias in each gas was measured by recording the specimen current over the range 0-800 V at pressures of 0.1, 0.5, 1, 5 and 10 Torr during panchromatic illumination of the sample. Panchromatic illumination was achieved by rotating the monochromator's diffraction grating to a mirror that enabled the broadband light to pass through the monochromator. Beam and sample parameters were identical in both experiments (20 keV beam energy, 2.06 nA beam current with a sample-detector gap of 13.47 mm). $I_{\delta+\eta}$ was determined by measuring I_{Σ}^{S} while irradiating a polycrystalline platinum foil sample and subtracting I_0 which was measured while irradiating the inside of a Faraday cup to suppress secondary and backscatter electron emission.

4.3.2 EPYS

Complimentary measurements were performed using EPYS to study gas amplification in the absence of primary or backscattered electrons. EPYS enabled examination of low-energy electron amplification behaviour in sample-detector configurations identical to ESEM, but in the absence of high-energy electron amplification inherent in ESEM studies.

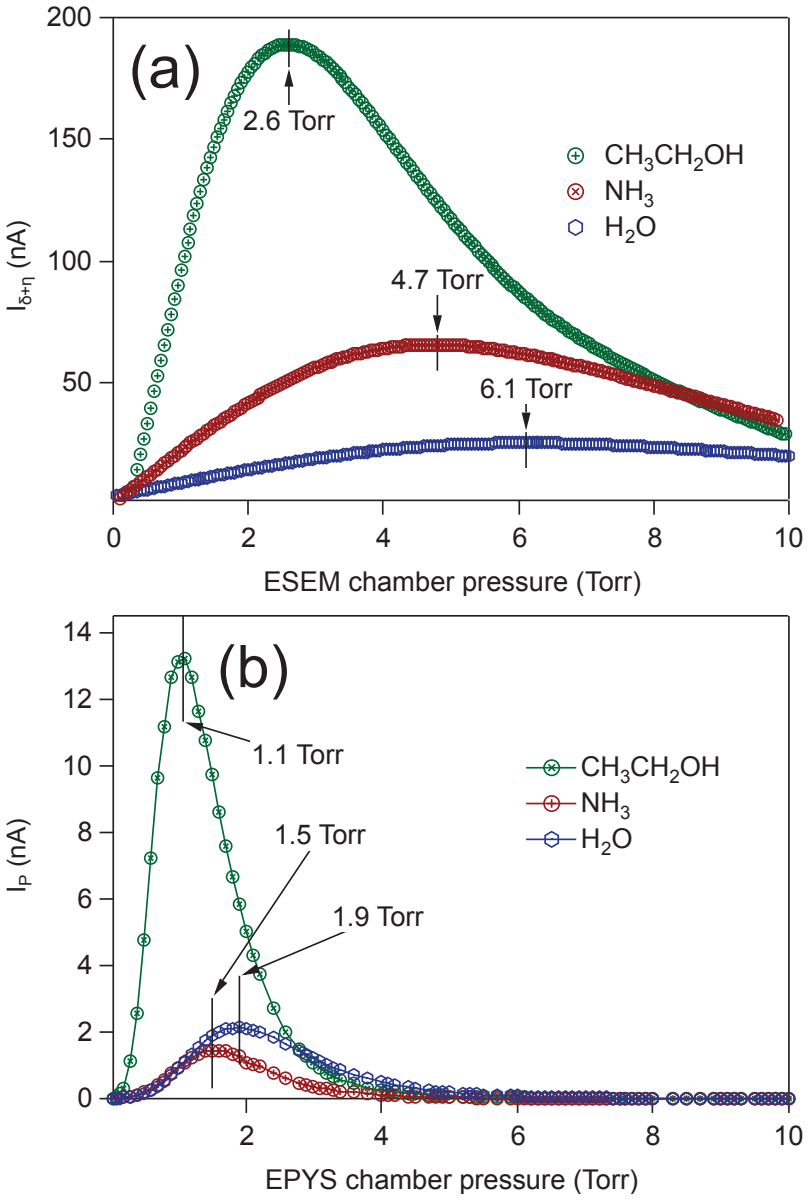

FIGURE 4.2: Gas-amplified electron emission current measured versus pressure using ethanol, NH_3 and H_2O. (a) In ESEM, the current is a sum of two components ($I_{\delta+\eta}$) that correspond to cascade-amplified, low energy ($\lesssim$ 20 eV) secondary electrons and high energy (keV) backscattered electrons. (b) In EPYS the current (I_p) is generated purely by low energy ($\lesssim$ 7 eV) photoelectrons. The detector anode bias was 400 V in both cases.

Correlative EPYS experiments were performed with each gas over the same pressure range as ESEM experiments with a sample detector gap of 12 mm. I_P was measured as a function of pressure over the range 0.1-10 Torr. EPYS spectra were collected as a function of detector bias in each gas at identical pressures to the ESEM measurements. in addition, I_P generated upon panchromatic illumination up to 7 eV has been plotted as a function of detector bias in Figure 4.4 for comparison with ESEM data.

4.4 Results

$I_{\delta+\eta}$ as a function of pressure in the ESEM is shown in Figure 4.2 (a). The greatest amplification is achieved using ethanol vapour, which occurs at 2.6 Torr. Optimum amplification in NH_3 and H_2O occurs at 4.7 and 6 Torr respectively.

Figure 4.2(b) shows equivalent EPYS data, revealing the same trend for gas-amplification of the low energy photoelectrons ($\lesssim 7$ eV) emitted from the sample in our EPYS setup. Ethanol is the most efficient amplifier at pressures smaller than ~ 2.5 Torr, and optimum amplification in ethanol, NH_3 and H_2O occurs at 1, 1.5 and 1.9 Torr respectively. The differences between the ESEM and EPYS data (i.e. the EPYS curves are shifted to lower pressures) arises from the contribution of backscattered electrons to the ESEM signal. Backscattered electrons have significantly higher energy than secondaries, and optimal amplification therefore occurs at higher pressures [86, 111].

Figure 4.3 shows plots of both I_Σ and $I_{\delta+\eta}$ obtained for ethanol, NH_3 and H_2O using an ESEM at gas pressures of (a) 0.5, (b) 1 and (c) 5 Torr, respectively. Each curve is plotted up to the breakdown voltage which marks the onset of dielectric breakdown and hence the maximum useful amplification efficiency of the gas. Ethanol is able to sustain the highest breakdown current I_Σ^{max} at all pressures, while $I_{\delta+\eta}^{max}$ is very similar to NH_3 and H_2O at 5 Torr.

I_P upon panchromatic illumination yields complimentary data to the ESEM measurements in that we have a constant initial electron energy distribution triggering the gas cascade that may be plotted as a function of detector bias. Logarithmic plots of the values from panchromatic EPYS data are shown at 0.5, 1 and 5 Torr in Figure 4.4 (a), (b) and (c) respectively. The values of I_p were collected in 40 V increments until breakdown occurred.

The greatest I_P achieved was over 60 nA in 1 Torr of ethanol vapour at 440 V, surpassing the optimised 30 nA and 28 nA produced in H_2O and NH_3 respectively. The efficiency of ethanol diminishes rapidly as the pressure is increased; however, H_2O becomes a more desirable amplification medium beyond $\sim$5 Torr.

All three gasses were examined for the possibility of carbonaceous deposition resulting from electron beam induced dissociation of ethanol on the sample. Sequences of images

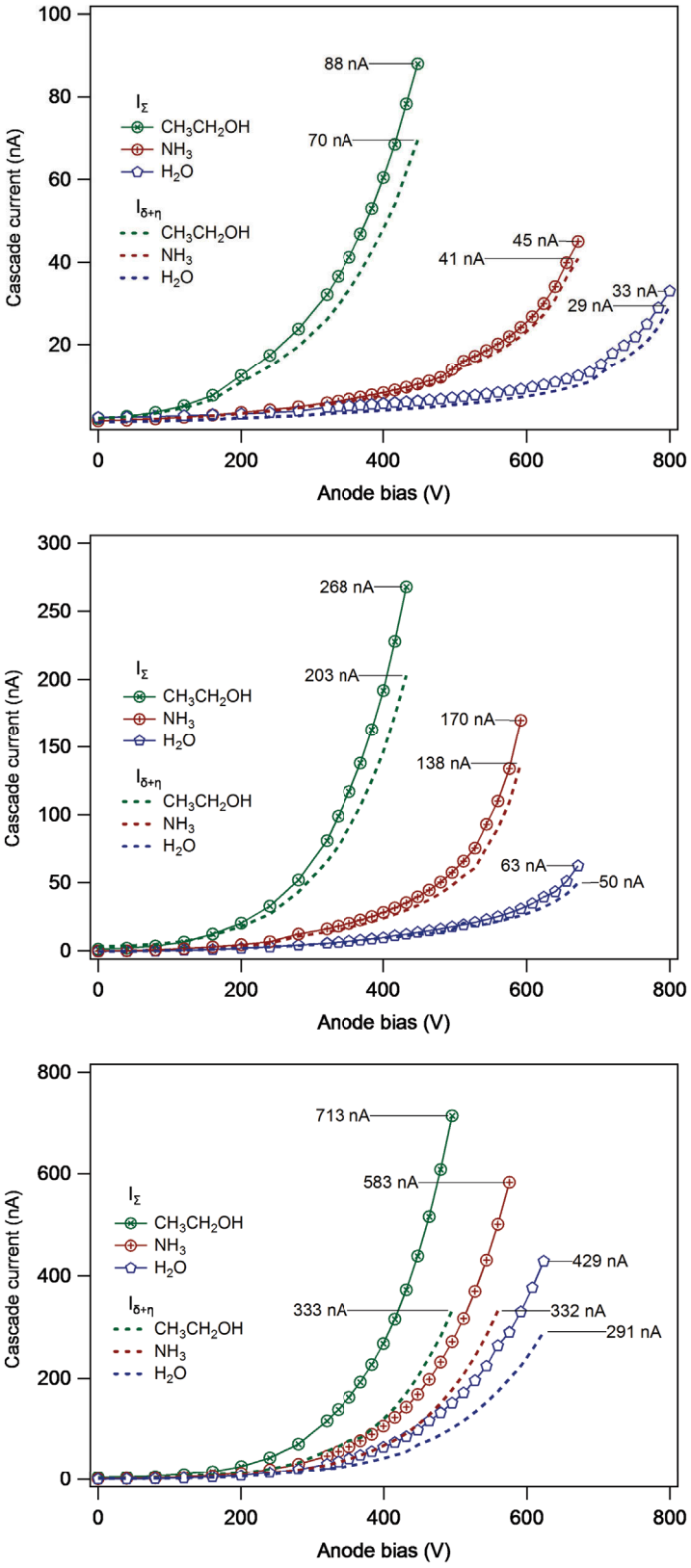

FIGURE 4.3: Gas-amplified electron emission current (I_Σ) and ($I_{\delta+\eta}$) measured versus ESEM detector anode bias using ethanol, NH_3 and H_2O, at gas pressures of (a) 0.1 Torr, (b) 1 Torr, and (c) 5 Torr. The maximum $I_{\delta+\eta}$ reached at the onset of dielectric breakdown of each gas is shown for each pressure on the plots.

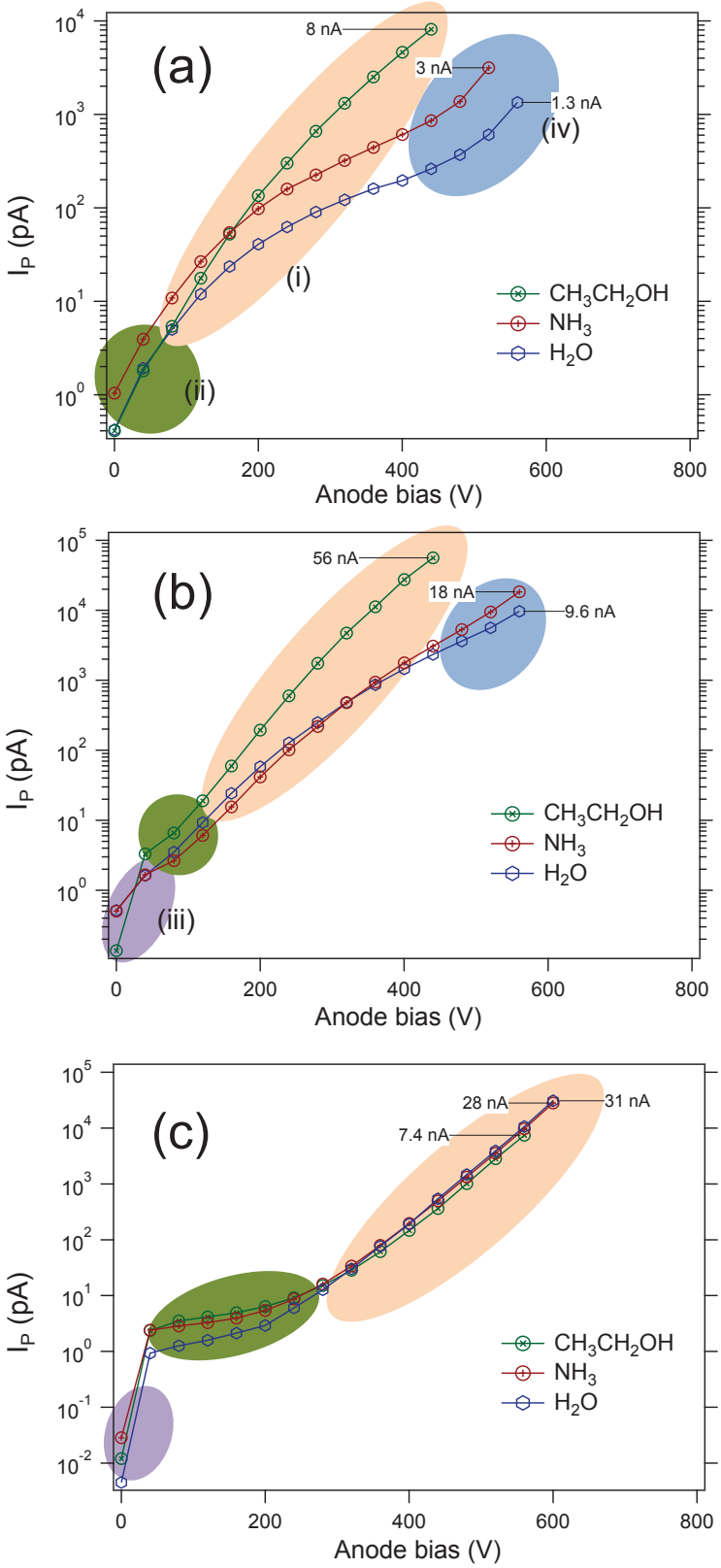

FIGURE 4.4: Gas-amplified photoelectron emission current (I_p) measured versus EPYS detector anode bias using ethanol, NH_3 and H_2O, at gas pressures of (a) 0.1 Torr, (b) 1 Torr, and (c) 5 Torr. The maximum current reached at the onset of dielectric breakdown of each gas is shown for each pressure on the plots. The three amplification regimes (i, ii and iii) labelled on the plots are discussed in the main text.

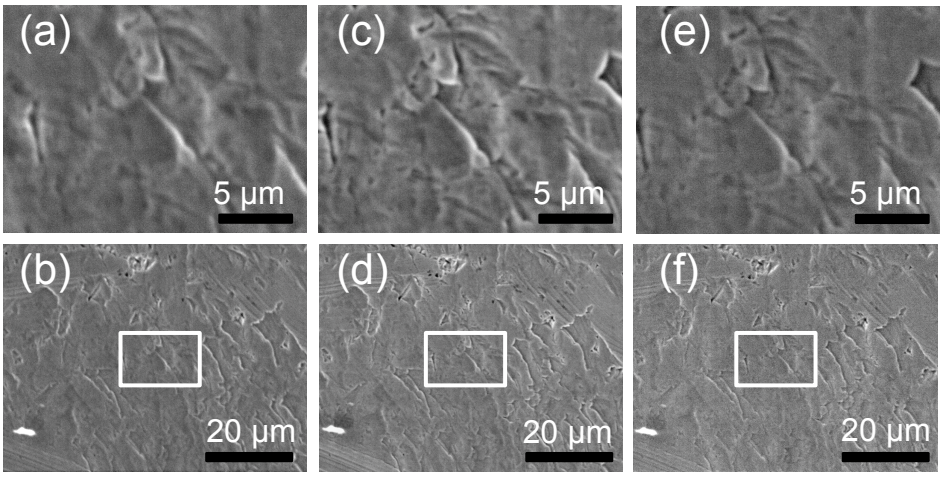

FIGURE 4.5: Images taken at high and low magnification in (a) and (b): H_2O, (c) and (d): NH_3, (e) and (f): ethanol vapour. The sequences verify that little to no carbon deposition occurs during electron beam irradiation in the presence of ethanol.

were taken first at high, then at low magnification. The mag-out sequences are shown in H_2O, NH_3 and ethanol in Figure 4.5 (a)-(b), (c)-(d) and (e)-(f) respectively. No contrast change arose from irradiation at high magnification in ethanol which indicates there is little to no carbon deposition occurring.

4.5 Discussion

Our results show that ethanol is a more efficient gas amplification medium than NH_3 and H_2O under the conditions that are typically used in ESEM and EPYS, and comparable at pressures greater than $\sim$ 5 Torr. In order to explain the amplification properties of the three gases, we must consider the electron energy loss and gain mechanisms in the gas cascade. The rate of change of energy of an electron in the gas cascade ($\partial E/\partial s$, where s is the electron trajectory between the sample and the detector anode) can be described by:

$$\frac{\partial E}{\partial s} = \Gamma - \Omega - \Lambda \tag{4.6}$$

where:

- Γ is the rate at which electrons gain energy under the influence of the electric field between the sample and the detector anode.

- Ω is the rate at which energy is lost through ionising collisions that increase the cascade current. It is determined by the inelastic cross-sections for electron-gas scattering processes that lead to ionisation.

- Λ is the rate at which energy is lost via non-ionising inelastic scattering events. It is determined by the inelastic cross-sections for scattering processes that do not lead to ionisation (e.g. those corresponding to vibrational and rotation modes of gas molecules).

4.5.1 Dependence of amplification on pressure

In Figure 4.2, amplification increases with pressure, reaches a maximum, then begins to decrease beyond the optimum pressure for each gas. The rate of increase is governed by Ω which is greatest for ethanol, followed by NH_3 and lowest for H_2O. The rate of decrease with pressure is governed primarily by Λ, which is also greatest for ethanol, followed by NH_3 and H_2O. Ω and Λ determine the optimum pressure at which the gas amplification efficiency is greatest for each gas. The difference between the amplification intensity of water and ammonia in ESEM and EPYS is due to the high ionisation efficiency of water by high energy primary electrons.

The general shape of the curves in Figure 4.2 is well understood [86, 124]. At very low pressures, amplification is low because the electron mean free path is long, the number of electron-molecule collisions between the sample and the anode is small, and amplification increases with pressure as the number density of gas molecules increases. However, the increase in the collision rate causes a decrease in the mean electron energy, and a decrease in the amount of energy gained by electrons between collisions. This trend eventually causes amplification to decrease with increasing pressure because non-ionising collisions dominate at low electron energies, particularly as it falls below the ionisation threshold of the gas (E_0). Thus, $1/E_0$ typically correlates with amplification efficiency [124], and often serves as an indicator of the relative gas amplification efficiency of different gases.

However, ethanol, NH_3 and H_2O have ionisation thresholds of 10.5, 10.1 and 12.6 eV [125–127], which cannot be used to explain why ethanol is a more efficient amplifier than NH_3 and H_2O. This can, however, be explained by the valence orbital structures of the gas molecules, and in particular the number of outer shell electrons with a binding

energy that is similar to E_0, schematically illustrated by the Lewis structures in Fig 4.1 (d). The contribution of valence orbitals to interaction cross-sections is described by a basic additivity rule [128, 129], which builds a total cross section by summing the number of valence electrons (and nuclei) of a molecule's constituent atoms. Modified additivity rules have been developed to account for molecular geometries and the redistribution of atomic electrons due to molecular binding [130, 131]. However, as a general rule, molecules composed of a greater number of atoms have larger scattering cross sections [132, 133], thus, they possess a relatively large Ω for high electron energies. The ionisation energy and number of valence electrons for ethanol, NH_3 and H_2O are shown in Table 4.1.

Molecular structure can also be used to explain why Λ is greatest for ethanol, followed by NH_3 and then by H_2O. Energy imparted to a molecule by inelastic scattering events may be dissipated though vibrational and rotational modes available to the molecule, which serve to decrease the probability of electronic relaxation via ionisation. Although the absolute single ionisation cross section for ethanol is greater than both H_2O and NH_3, the non-ionising inelastic scattering cross section is also larger, which leads to a greater Λ.

Molecule	Ionisation energy (eV)	Number of valence electrons
H_2O	12.3	8
NH_3	10.1	8
CH_3CH_2OH	10.5	20

TABLE 4.1: Table of ionisation energies and number of valence electrons for the gaseous molecules: H_2O; NH_3; and CH_3CH_2OH.

4.5.2 Dependence of amplification on detector bias

The plots in Figure 4.4 demonstrate a benefit of using EPYS to characterise the gas cascade. The emitted photoelectrons have a narrow energy distribution concentrated below the ionisation threshold of each gas. All electrons must therefore be accelerated beyond E_0 before they can contribute to the gas cascade; and subtle variations in amplification behavior are therefore resolved as changes in the scaling of I_p with anode bias. Four distinct scaling regimes, labeled (i)-(iv), are indicated on the plots (we note that at low anode biases, when $I_p \lesssim 30$ pA, absolute differences between the curves should

be ignored since they are on the order of variations in the direct current offset of each dataset).

In regime (i) gas cascade amplification scales approximately exponentially with anode bias. Exponential scaling is expected from the ideal Townsend gas capacitor model [83] (ie: a straight line, as seen on the logarithmic plot in Figure 4.4c). It is observed under conditions of high pressure and high anode bias, whereby the electron energy distribution is in a steady-state throughout the vast majority of the sample-anode gap (ie: $\Gamma = \Omega + \Lambda$). That is, the system is in the so-called 'swarm-condition' [86]. At reduced pressures (Figure 4.4a-b), the scaling in regime (i) is not exponential because $\Gamma \neq \Omega + \Lambda$, and changes in anode bias alter the energy distribution of electrons in the gas [134].

At low voltages, regime (ii), electron-ion recombination in the gas is significant and the scaling of I_p with bias is modified by the effects of the voltage on the recombination/separation efficiency. At very low voltages and high pressures, regime (iii), some electrons are never accelerated beyond E_0, and a subtle increase in bias causes an abrupt increase in amplification (Figure 4.4c).

At high voltages and low pressures, regime (iv), super-exponential scaling is observed in some cases, just before the onset of breakdown. This is attributed to an amplification feedback effect that is discussed below. The super-exponential scaling is observed when amplification is relatively low, and changes slowly as the voltage is increased. When the amplification factor is large (and increasing quickly with bias) and the feedback coefficient is low, the contribution to I_Σ from feedback rises very quickly over a small voltage range close to breakdown, and is not resolved in the curves in Figure 4.4.

4.5.3 Ultimate amplification efficiency and dielectric breakdown

Ultimate amplification efficiency is limited by dielectric breakdown of the gas, governed by a positive feedback coefficient (k). The coefficient is non-zero due to electron ejection from the sample caused by positive ions and excited neutral gas molecules that are generated in the gas cascade and come into contact with the sample surface. The electron ejection is typically attributed to potential rather than kinetic energy transfer

to the sample, i.e. emission of Auger and photoelectrons induced by ions and excited neutrals that neutralise and de-excite at the surface [83, 86].

In this framework, larger, more complex molecules have smaller feedback factors due to a large number of vibrational and rotational modes through which they are able to dissipate energy gained by electron capture from surfaces [83]. This is consistent with ethanol possesing the largest maximum breakdown current (I_Σ) in ESEM and EPYS over the pressure range studied, and the trend of diminishing breakdown currents for the gases ethanol, NH_3 and H_2O, as shown in Figure 4.3 and Figure 4.4.

However, k also varies with gas pressure, as evidenced by the significant variation of amplification achieved at breakdown over the pressure range studied. Although there is unlikely to be a simple relationship between k and pressure, mechanisms leading to ion/molecule induced electron ejection at the surface will vary as the ion density and energy distribution at the sample surface changes. Feedback arising from kinetic energy transfer will increase at low pressures due to an increased mean free path, as ions are able to gain energies exceeding a secondary electron emission threshold ~300 eV [135]. At higher pressures, swarm conditions for the gas cascade are met at much smaller distances from the sample such that incident ion density at the sample is higher, increasing k.

The effect of incident ion density on k is also suggested in the differences between I_Σ^{max} and $I_{\delta+\eta}^{max}$ observed in Figure 4.3. As the gas pressure is increased, a greater proportion of the total amplified current is initiated by high energy primary electrons that will generate multiple ions along their path at significant distances from the sample surface. A result of the ion generation occuring mid-gap is dispersion of the ions over a larger area, where they still contribute to the measured current but are less likely to generate feedback electrons that subsequently initiate a gas cascade. This enables the high energy primary electrons to generate a larger portion of ions that contribute less to feedback.

4.6 Conclusion

Ethanol vapour has been identified as a very efficient electron amplification medium and therefore ESEM imaging gas. Using quantitative ESEM and EPYS measurements, the amplification behaviour of ethanol, NH_3 and H_2O has been characterised and compared.

Ethanol performs best at lower pressures than NH_3 and H_2O, which we attribute to energy loss from greater inelastic electron scattering by ethanol at higher pressures. It is capable of maintaining much greater cascade currents than both NH_3 and H_2O due to smaller feedback that arises from PI-surface interaction. This is consistent with a greater number of non-ionising excitations and vibrational modes in ethanol that may dissipate energy non-radiatively and without electron ejection. That also gives rise to greater non-ionising inelastic scattering at higher pressures.

In ESEM, the PE contribution to the gas amplified current becomes much larger in ethanol as the pressure increases resulting from a greater fraction of PEs scattering in the gas phase, reducing the total contrast information-carrying SE yield and increasing the background signal via SEs generated by the beam skirt.

Also noteworthy of note the effect that adsorbates have on the sample surface density of states and escape barrier. Changing these properties directly affects the SE yield and energy distribution in ESEM, and should be considered when selecting an imaging gas for optimal dynamic range.

4.7 Implications

The implications of this study are largely in the realm of low-vacuum charged particle detection. This is increasingly becoming an important tool to bridge a gap between conventional, ideal surface physics and the dynamic processes that occur in chemical and biological systems. Physical processes that have been unobservable previously with vacuum-based instruments including surface wetting behaviour, formation of liquid overlayers and real time analysis of catalytic chemical reactions can be monitored with systems that are based on low vacuum electron detection.

Gaseous charged particle detection enables a variety of technological systems to be used in environments that have previously been inaccessible to vacuum-based analytical instrumentation. Examples of such systems include mass spectrometry for environmental field testing and portable security devices.

This application also identifies a characteristic of gaseous molecules that can be used to identify their presence and concentration in gas detection systems.

Chapter 5

Application of EPYS: characterisation of subsurface defects and sensitivity to ambient gas

5.1 Summary

Environmental photoelectron yield spectroscopy (EPYS) has been used as a correlative characterisation method in a broader study of ZnO. Specifically, EPYS was used to correlate defect electronic structure and surface stoichiometry with electrical and optical properties of ZnO. A self-consistent model of the surface band structure has been proposed, based on EPYS measurements that invoke space charge effects arising from the presence of intrinsic point defects near the ZnO surface. High surface conductivity and green luminescence (GL) are attributed to V_O defects, low electrical conductivity and yellow luminescence (YL) to deep lithium acceptors, and red luminescence (RL) to V_{Zn}-V_O complexes.

In addition, the capacity for EPYS to monitor real time changes in electronic structure due to adsorption of NH_3 onto ZnO is demonstrated by presenting time-resolved photoelectron emission profiles while increasing the partial pressure of gaseous NH_3.

5.2 Introduction

Zinc oxide (ZnO) has a central role in the ongoing development of semiconductors for lighting [136–139], solar energy harvesting [140–142], spintronics [143–145] and pietzo-electronics.

The following sections provide a brief background to ZnO and an overview of the advantages and current limitations of ZnO in the development of optoelectronic devices. In the past two decades ZnO has generated significant interest in the research community due partially to its large exciton binding energy, 60 meV, which offers the potential for high lumen/kWh solid state lighting devices [138, 146]. It is also due to the fact that ZnO has a direct and wide bandgap of 3.37 eV at 300 K, large piezoelectric constants, strong luminescence, high radiation hardness, and high thermal resistance [137, 142].

It has recently become readily available in high quality bulk crystal due to the advances in growth methods [147–150]. ZnO has also been predicted to exhibit induced magnetic properties from dilute transition metal impurities at room temperature [141, 151, 152], a promising attribute for potential spintronic device materials. Zinc oxide has a number of advantages over its primary competitor in the lighting industry, GaN. Among these are non-toxic growth methods [153]; low refractive index; stability under UV and high energy radiation [154, 155]; and bulk substrates that can be grown, allowing fabrication of homeoepitaxial layers [148, 156, 157].

More recently, sensitivity of both electrical and optical properties of ZnO to the presence of gases have been identified as potential flags to be used in gas sensing devices [158]. In particular, a strong electrical response to gaseous NH_3 has been reported [157, 159–161]. The presence of adsorbates at the ZnO surface can alter its electrical conductivity by redistributing electrons at the solid-gas interface, generating depletion regions that are able to locally accumulate or deplete charge carriers in significantly larger concentrations than in the bulk structure. However, the response of ZnO surface conductivity to NH_3 depends also on its initial state, which is established by the formation of subsurface intrinsic and extrinsic defects.

The samples used in this study were hydrothermally grown nanorods. The hydrothermal method, also more generally known as the solvothermal method (when H_2O is not used as the solvent), is used for mass production of many crystals including quartz, GaN and

ZnO [149, 162–164]. In this process, water is used as a polar solvent for ZnO, which is then placed in an autoclave. Roughly 70-90% of the autoclave volume is filled with the solvent. The nutrient, composed of sintered ZnO pellets, is dissolved in the hotter region located at the bottom section of the autoclave. The saturated aqueous solution in the lower region is transported by convective motion of the solution to the upper region housing the ZnO seed crystals suspended by platinum wires. The hydrothermal growth of ZnO is usually performed in a temperature range from 300 to 430°C at pressures from 70 to 250 MPa [162].

The doping effects in ZnO fall into three subgroups. These are:

1. unintentional n-type doping, with defects and impurities from crystal growth;
2. intentional n-type; and
3. intentional p-type doping with purposeful incorporation of impurities.

Defects are a fundamental part of the study of semiconductors. Defects are always present as intrinsic point defects, dislocations and impurity atoms. They alter the electrical and optical properties of semiconductors. In the past, sub-bandgap luminescence and electrical conductivity had been attributed to numerous defects that are now known to be unlikely to have been responsible [19, 154, 165]. There are still a number of problems currently preventing the identification of these defects. Intrinsic point defects in ZnO are discussed in detail below.

5.2.1 Intrinsic point defects in ZnO

While n-type doping can be easily achieved, the unintentional, native n-type state results in a background carrier concentration that can negate the effect of incorporating acceptor states as a means of producing p-type material. Controllable conductivity paves the way for short wavelength optoelectronic devices with ZnO. However, this includes fabricating high quality ZnO with either electron or hole majority carrier concentrations in excess of 10^{17} cm^{-3} [166–168]; and there has been great difficulty attaining bipolar carrier doping in wide band-gap semiconductors, especially ZnO due to the p-type compensation from native donors [168–171].

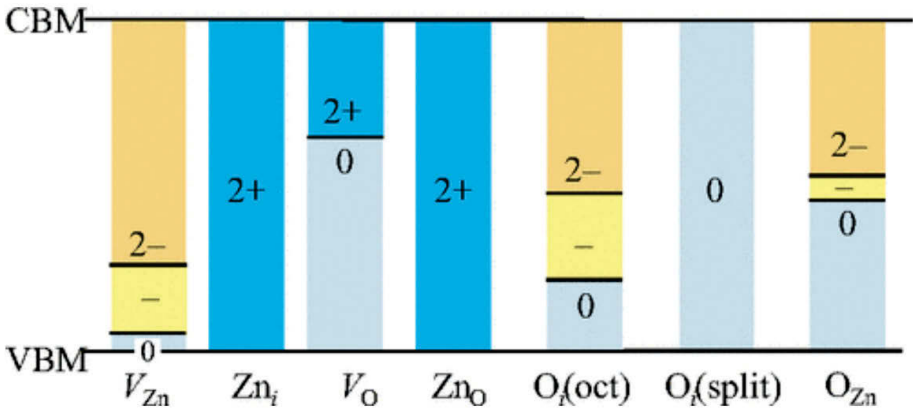

FIGURE 5.1: Charge states and transition levels of intrinsic point defects in ZnO. The charge states depend on value of the Fermi level. Figure adapted from Janotti and van der Walle [172].

N-type doping has been established through substitution of a group IIIA element (group 13 - Al, Ga, In etc.) on the Zn site, producing highly conductive ZnO. However, efforts to obtain p-type ZnO have been unsuccessful, as native defects in unintentionally doped ZnO compensate the potential acceptors for p-type conductivity [157, 172–174]. Native point defects in zinc oxide include Zn vacancies (V_{Zn}), Zn interstitials (Zn_i), oxygen vacancies (V_O), oxygen interstitials (O_i), and zinc and oxygen anti-sites (Zn_O and O_{Zn}). Figure 5.1, taken from Janotti and van der Walle [172], shows the charge states and relative transition levels of native point defects within the ZnO bandgap.

The concentration of a point defect depends on their formation energy. Formation energies - shown in Figure 5.2 - suggest that under thermodynamic equilibrium the dominant defects should be vacancies: V_O in p-type material and V_{Zn} in n-type material. Both vacancy sites have the lowest formation energies in zinc rich ZnO, with V_O favouring the Fermi level close to the valence band and V_{Zn} preferring the Fermi level close to the conduction band. The zinc vacancy and oxygen interstitial dominate the O-rich ZnO.

5.2.1.1 Oxygen vacancies

V_O has been reliably shown to be a deep donor, with an unstable charge state of 1+ at about 1.1 eV below the conduction band minimum (CBM) [146, 176, 177]. Under thermodynamically stable conditions, ${V_O}^{1+}$ decays into either ${V_O}^{2+}$ or ${V_O}^{0}$ and are not believed to contribute to conductivity. However, V_O are predicted to compensate p-type carriers, an impediment to producing highly conductive p-type ZnO. The calculated

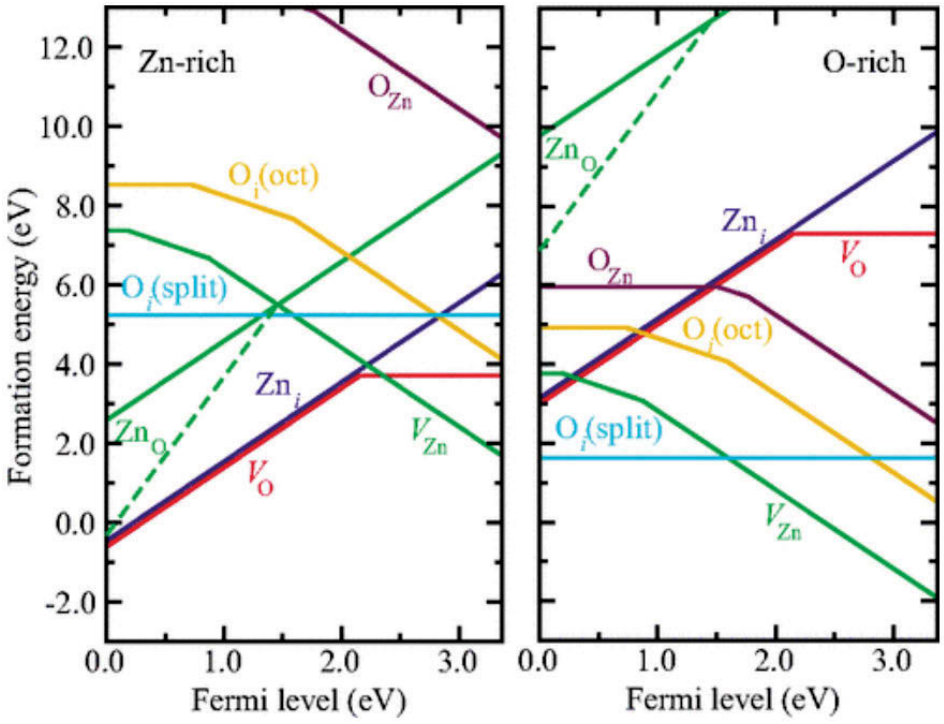

FIGURE 5.2: Formation energies of native point defects in ZnO calculated by Janotti et al. [175]. The formation energies are plotted as a function of the Fermi level position in oxygen (left) and zinc (right) rich conditions. The different slopes of the traces represent different charge states.

migration barrier is ∼2 eV [178, 179], and there has been disagreement in the literature whether V_O should be present in significant concentrations in n-type ZnO [157, 158, 170, 180–182]. The green luminescence band (2.4 eV) has been attributed to the V_O [146, 180, 183, 184].

5.2.1.2 Zinc vacancies

V_{Zn} are deep acceptors; their stable -1 and -2 charge state levels are 0.18 and 0.87 eV above the VBM respectively [156, 157, 177, 185]. These states are due to the broken bonds of the four oxygen nearest neighbours. The states are too deep in the bandgap to contribute to p-type conductivity at room temperature, and the energy of formation is too high in p-type material for sufficient V_{Zn} concentrations to be present [178, 179, 184].

ZnO nanostructures have exhibited distinctly different electrical conductivity and luminescence profiles that have been attributed to the presence of V_O, V_{Zn} and Li. These properties are discussed in more detail in the following sections.

5.2.2 Optical properties

The luminescence spectrum of zinc oxide has two dominant features - as shown in Figure 5.3 - a near-band edge (NBE) emission, which manifests as a narrow peak in the UV region (3.3 eV); and the defect luminescence, which is observed as a broad peak in the visible region (1.5-3 eV), due to transitions occurring within the bandgap. The defect luminescence is generally accepted as being the combined result of at least three deep level transitions: a green luminescence (GL) at 2.4-2.5 eV, a yellow luminescence (YL) centred at 2.1 eV and a red luminescence (RL) at 1.7 eV [158, 176, 183–185]. The following section gives a brief introduction to what is known about these features, and the effects that the incorporation of defects and impurities have on them.

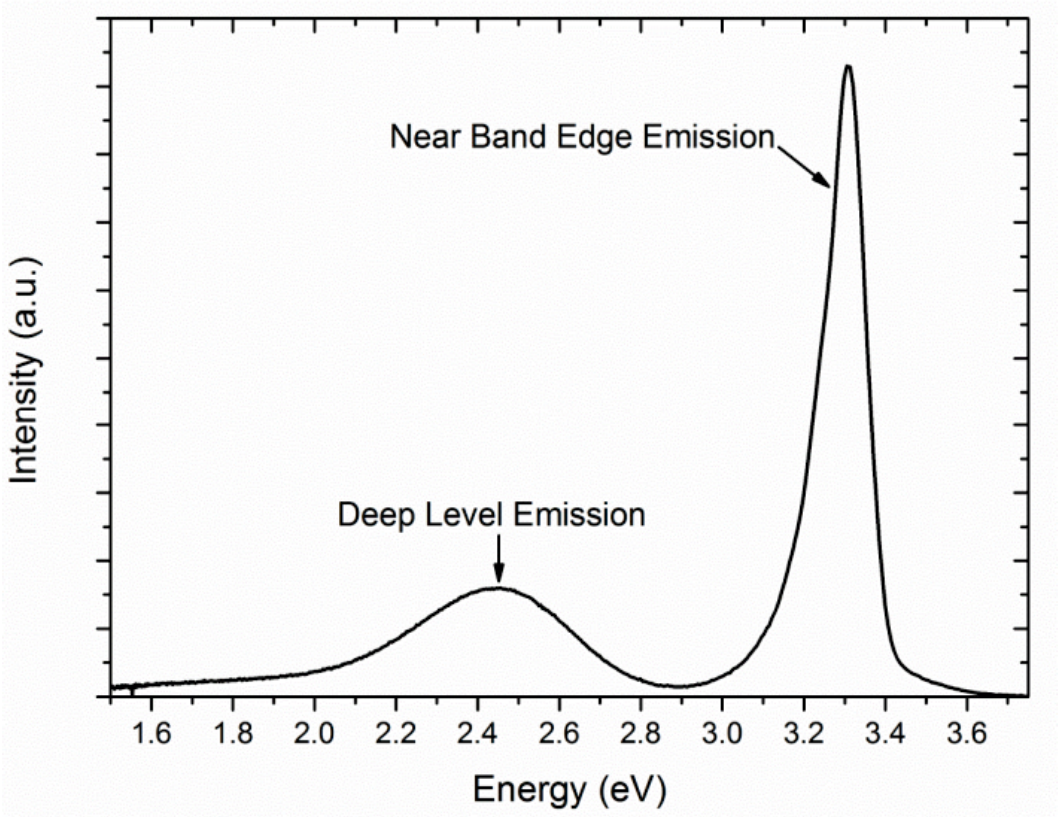

FIGURE 5.3: Characteristic cathodoluminescence profile from ZnO at room temperature showing the near band edge emission at 3.37 eV and defect related emission arising from inter-bandgap radiative recombination pathways.

5.2.2.1 Near band edge luminescence

The NBE luminescence from zinc oxide is composed of multiple spectral lines that are only resolved at cryogenic temperatures, resulting from recombinations of carriers across

the bandgap. Free exciton transitions occur at 3.377 eV, the band edge [138, 186]. The sharp spectral lines at the near-band edge, 3.36 eV, originate from bound exciton recombinations [138, 187]. Sharp lower energy emission peaks occur due to longitudinal optical phonon replicas separated by 72 meV [138, 180]. At energies from 3.31-3.34 eV, two-electron satellite recombination lines are observable due to neutral donor-bound exciton recombinations [138].

5.2.2.2 Defect luminescence

The broad defect luminescence peak of ZnO, ranging from 1.5-3 eV, has three main contributing components; the GL centered at 2.45 eV, the YL centered at 2.1 eV and the RL at 1.7 eV.

The nature of the GL, centred on 2.45 eV, remains a controversial subject. The GL has in the past been attributed to bound exciton transitions between ground and excited states of copper impurities, resulting in an emission at about 2.8 eV [146]. However, ZnO exhibits the GL with minimal Cu impurities, and also exhibits other features (such as dramatic changes in luminescence upon annealing [188]) ruling out the involvement of Cu. The GL has more recently been attributed to intrinsic defects in zinc oxide, such as the V_O, Zn_i and zinc antisites [146, 183, 184, 189].

The YL contributes to the mid range of the defect luminescence. Its peak is centred at 2.1 eV with a FWHM of 0.5 eV. At low temperatures it has been attributed to donor-acceptor pair (DAP) recombinations between shallow donors and Li_{Zn} impurities that exist as deep acceptor levels (0.8 eV above VBM) in the bandgap [183, 185, 190, 191]. It was suggested that the YL may be a result of free to bound transition associated with the Li_{Zn} acceptor [138]. The YL is frequently observed in hydrothermally grown ZnO that has been unintentionally doped by Li during the growth process.

The RL is a luminescence peak centered at 1.7-1.9 eV. This luminescence has been previously attributed to O_i and Zn_V, as it has been observed in Zn rich ZnO samples [185, 192, 193]. It has also been strongly linked with surface states, as it can be removed by de-hydrogenation of the ZnO surface [142, 157]. Recently the RL has been attributed to defect complexes such at O_i-H and Zn_i-V_O [142, 183].

5.2.3 Electrical properties

The conductivity of bulk zinc oxide is determined by the growth procedure due to the introduction of native defects and/or extrinsic impurities. Hydrothermally grown ZnO exhibits highly resistive electrical behaviour. Alternative growth methods produce relatively less resistive ZnO. The respective carrier concentrations and resistivities are typically around $\rho = 1000\ \Omega$cm and $n = 10^{17}$ cm^{-3} [167, 168, 171]. Defects and impurities incorporated in each method are the source of carriers that determine the carrier concentration, and hence conductivity.

High electrical surface conductivity is proposed to arise from downward band bending at the surface due to the formation of an accumulation layer in the case of a dominant near-surface V_O population [184, 194].

5.3 Experimental methods

The ZnO samples used in this study were provided by, and optically and electrically characterised by Suranan Anantachaisilp of the University of Technology, Sydney. ZnO nanorods 50-60 nm in diameter were hydrothermally grown at 90°C. The low temperature growth was achieved by seeding sapphire substrates in 0.025 M zinc nitrate hexahydrate ($Zn(NO_3)_2 \cdot 6\,H_2O$) and 0.025 M hexamethylenetetramine ($C_6H_{12}N_4$) for three hours. The samples were annealed at 650°C for 30 minutes in one of two different environments composed of ambient Zn vapour or gaseous O_2. As-grown, O_2 annealed and Zn annealed samples were characterised with X-ray diffraction (XRD), scanning electron microscopy (SEM), cathodoluminescence spectroscopy (CL) and electrical surface conductivity measurements. Cathodoluminescence measurements were conducted in a FEI Quanta 200 SEM with a 5 kV, 0.2 nA beam illuminating an area 50 μm$\times$ 43 μm. The maximum photon generation depth was calculated to be 37 nm using CASINO simulations [195].

One each of the ZnO nanorod samples were studied with EPYS. Each sample was thermally conditioned in high vacuum prior to measurement by heating to 100 °C at 5×10^{-8} mBar for one hour to remove residual water and other contaminants. EPYS spectra were then collected in a dry Ar environment (1.3 mBar) by introducing Ar to the chamber

through a cryogenic trap that prevents the introduction of residual water from gas delivery lines into the chamber. Ar was selected as the ambient gas to observe the native surface state in the absence of adsorbed gas species. 50 Spectra were collected over the wavelength range 325-215 nm (3.8-5.8 eV) in 1 nm increments from each sample, and averaged in post-processing to increase the signal to noise ratio by increasing the effective collection time. Conductive pathways across the sapphire substrates were formed with silver paint at corners of each 10×10 mm sample to prevent charging.

5.3.1 Sensitivity to NH_3

Electrical sensitivity of the ZnO nanorod samples to gaseous NH_3 was investigated with conductivity measurements. These measurements were performed at room temperature and atmospheric pressure, inside a chamber though which NH_3 vapour flowed, using dry air as a carrier gas. The chamber was pumped lightly while drawing in air from the precursor vessel that contained liquid NH_3. A second inlet could be opened that allowed pure air to flow into the chamber while the NH_3 delivery line could be closed for baseline conductivity measurements. Furthermore, the concentration of NH_3 could be controlled by regulating the flow rates through each line using mass flow controllers. The sensitivity measurements were performed by monitoring the electrical current across each sample, while maintaining a constant potential across them of 1 V. These measurements were performed as a function of time over the period of 100 minutes.

Correlative EPYS measurements were performed to observe the effects of exposure to gaseous NH_3 on the ZnO nanorod photoelectron emission profile. The samples were initially characterised in a dry argon environment at 2 Torr and a temperature of 40°C. The gas cascade amplification was optimised at a detector voltage of 200 V. After several measurements, argon in-flow was stopped and the pumping rate decreased while NH_3 was slowly introduced to the chamber to maintain a constant pressure of 2 Torr. EPYS spectra were collected continuously as the NH_3 concentration increased over the course of 1 hour.

Due to the increasing partial pressure of NH_3 and decreasing argon partial pressure, the gas cascade amplification also decreased. The cascade amplification drops as NH_3 molecules have larger non-ionising electron scattering cross sections than argon atoms, and thus require high electric fields to achieve equivalent amplification. However, NH_3

also has more mechanical modes to dissipate energy than argon, and is thus able to continue increasing its amplification at higher voltages without electrically discharging across the sample-detector gap.

To compensate for the decreasing amplified photoelectron current, the detector voltage was reset to 400 V after 1 h. To achieve a stable gas cascade, argon partial pressure also needed to be minimized so as not to produce positive ion feedback and cause the cascade to become unstable. During the period in which the detector voltage was being reset, the chamber was purged by evacuating to 0.1 Torr, and the NH_3 flow rate subsequently increased to bring the chamber pressure back to 2 Torr, at which point the experiment resumed. The low vacuum environment was now dominated by gaseous NH_3 and the cascade amplification was much higher than in the argon and argon-NH_3 gas mix. EPYS spectra were then continuously collected over the period of 1 hr while the coverage of ZnO with NH_3 molecules reached a steady state.

5.4 Results

SEM images of the as-grown nanorods are shown in Figure 5.4. The samples are of high density and uniform hexagonal $\langle 0001 \rangle$ crystalline orientation, approximately 50-60 nm in diameter. Contact between rods that are aligned at slightly differing angles to the substrate allows for electrical conductivity measurements to be performed across the length of the substrate, and also enables EPYS characterisation. The XRD - shown in Figure 5.4 (d) - profiles were indexed to the wurzite phase of ZnO (P63mc, a=0.3249 nm and c=0.5207 nm). No significant change was observed in XRD following treatment in Zn or O_2 environments, indicating that no microstrain or extended defects were induced during the treatment process. Slight changes in the relative peak heights, however, indicate that the relative orientation of nanorods to the substrate were altered during the treatment process.

Figure 5.4 shows SEM images of the O_2 annealed (a) and Zn vapour annealed (b) ZnO nanorods. The structure and diameter of thermally treated nanorods is preserved, while a slight difference in the variation of orientation with respect to the substrate can be observed between the two samples, as is confirmed by XRD measurements.

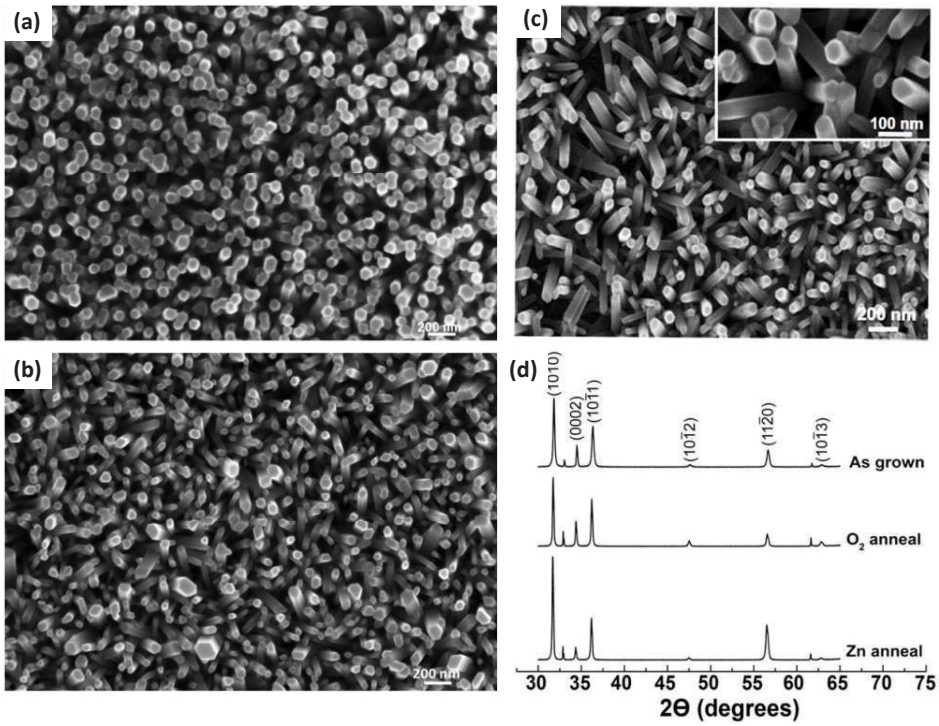

FIGURE 5.4: SEM images of nanorods thermally annealed in (a) O_2 environment (b) Zn vapour environment. The mean diameter and hexagonal structure of the nanorods remains unchanged; however, a slight reorientation with respect to the substrate can be observed. (c) As-grown nanorods (inset highlights high density hexagonal $\langle 0001 \rangle$ growth) and (d) shows XRD patterns of as-grown, O_2 annealed and Zn annealed nanorods. Changes in the relative peak heights arise from a reorientation of the nanorods with respect to the substrate. Data collected by Suranan Anantachaisilp.

A CL spectrum of each sample is shown in Figure 5.5. Each sample possesses a unique CL emission profile, with dominant defect related emission occurring in the frequently observed YL, RL or the GL bands. As-grown nanorods exhibit a strong YL at 1.9 eV and a quenched NBE emission at 3.3 eV. O_2 annealed nanorods emit predominately in the RL region (1.7 eV) with a small contribution to the emission profile from GL at 2.5 eV, and with a relatively small peak observed at the NBE. CL defect emission from Zn vapour annealed nanorods is dominated by the GL at 2.5 eV and a relatively strong NBE emission is observed at 3.3 eV. The differences between these CL profiles indicate clearly that the post-growth annealing process in different environments (O_2 and Zn vapour) are resulting in the incorporation, formation or activation of point defects that facilitate radiative carrier recombination.

As-grown nanorods exhibited the lowest conductance at 2.9×10^{-9} Ω^{-1} , while O_2 annealed nanorods possessed a conductance two orders of magnitude higher than as-grown at 3.1×10^{-7} Ω^{-1} and the Zn vapour annealed nanorods exhibited the greatest

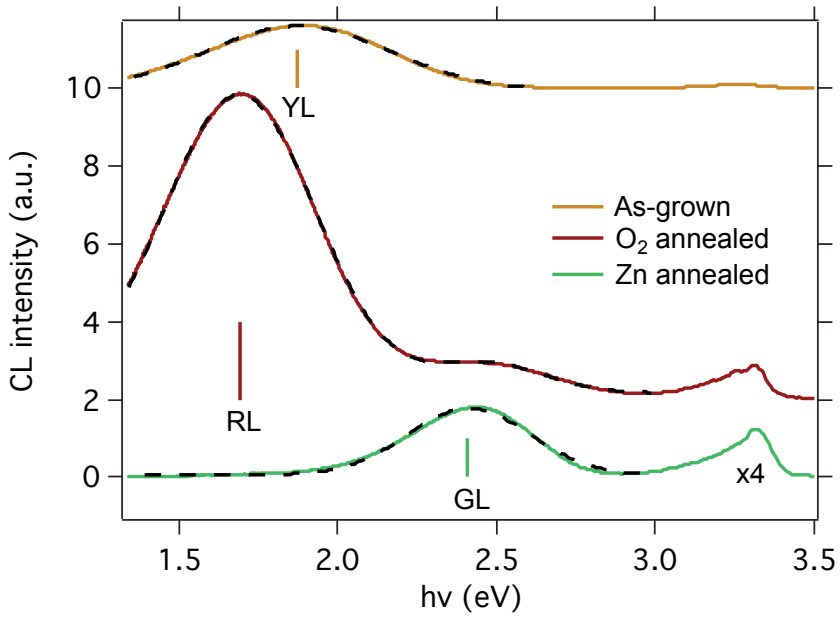

FIGURE 5.5: Cathodoluminescence spectra of ZnO nanorod samples. The yellow trace is a CL profile from as-grown ZnO nanorods and is dominated by the YL at 1.9 eV. The red trace is a CL profile from O_2 annealed nanorods and shows a large defect emission in the RL band (1.7 eV) and a smaller contribution from the GL (2.5 eV). The green trace is a CL profile from Zn vapour annealed nanorods (magnified by 4) and exhibits GL defect emission and a relatively strong NBE emission. Data collected by Suranan Anantachaisilp.

conductance at 3.4×10^{-6} Ω^{-1}.

The EPYS spectra of the clean dry ZnO nanorods in argon - displayed in Figure 5.6 - reveal two main differences in the photoelectron emission profile induced by the ambient annealing treatment of as-grown samples. Firstly, the photoelectron emission current near threshold of both O_2 and Zn vapour annealed samples were larger than as-grown samples by approximately two orders of magnitude. Secondly, the Zn vapour annealed samples also exhibited a significantly lower photoelectron emission threshold (4.12 eV) than both O_2 annealed and as-grown samples (4.47 and 4.61 eV respectively). The changes in surface electronic structure that would result in these differences in photoelectron emission characteristics are presented in the discussion, but it is worth noting the correlation between integrated area of the EPYS spectra and the electrical conductance of the ZnO samples.

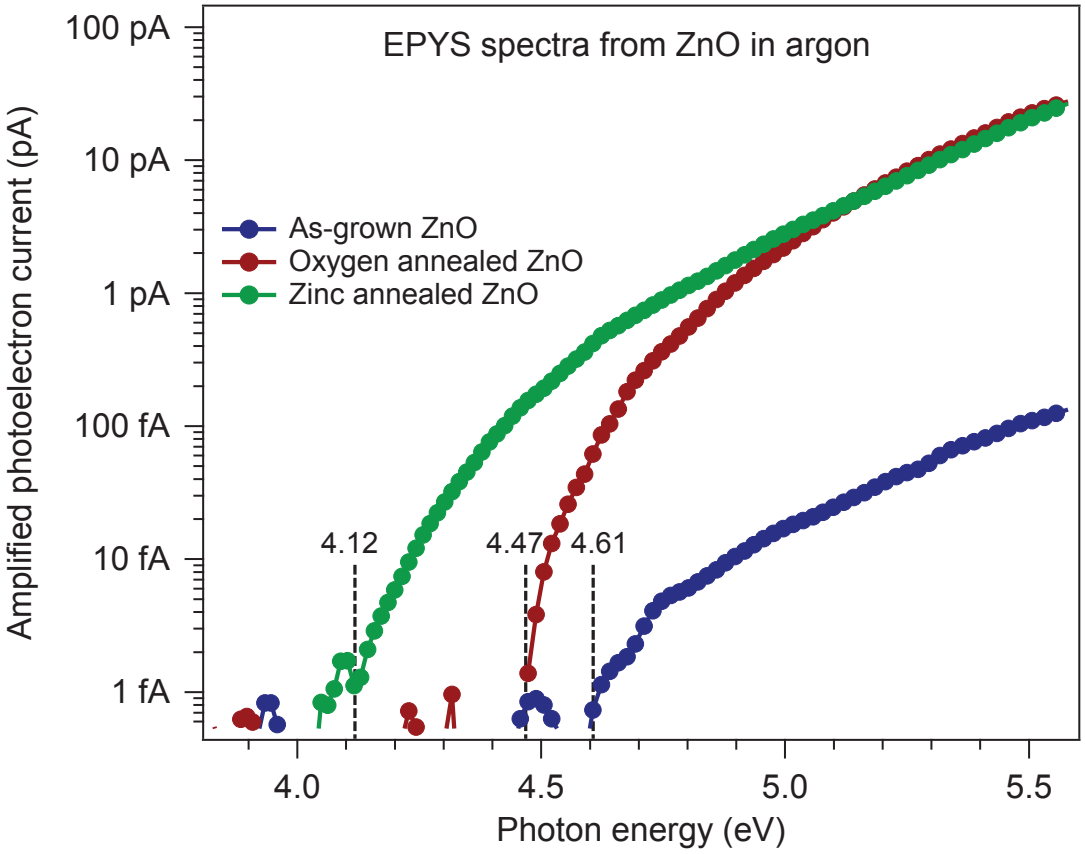

FIGURE 5.6: EPYS spectra of ZnO nanorods. The red trace shows an EPYS spectrum from as-grown nanorods, the green trace is from O_2 annealed nanorods and the blue trace is from Zn vapour annealed nanorods. Both thermally treated samples (O_2 and Zn vapour annealed) exhibited a significantly greater photoelectron emission current than as-grown nanorods. While as-grown and O_2 annealed nanorods both began to emit photoelectrons at 4.5 eV, the Zn vapour annealed nanorods exhibited a lower photoelectron emission threshold at 4.2 eV.

5.4.1 Sensitivity to NH_3

Measurements of the sensitivity of ZnO nanorod electrical conductivity to NH_3 are shown in Figure 5.7. The figures on the left are the ratio of a continuously monitored current I_g to the initial current, I_i, flowing across the samples with potential difference of 1 V applied, as a function of time during which NH_3 was introduced at increasing concentrations. The figures on the right hand side plot the maximum electrical sensitivity ratio as a function of NH_3 concentration.

In each case, the ZnO samples exhibited a reversible increase in electrical conductivity when exposed to NH_3. The strongest response was from O_2 annealed ZnO, which increased in conductivity by a factor of 23 when exposed to an ambient 100 ppm of

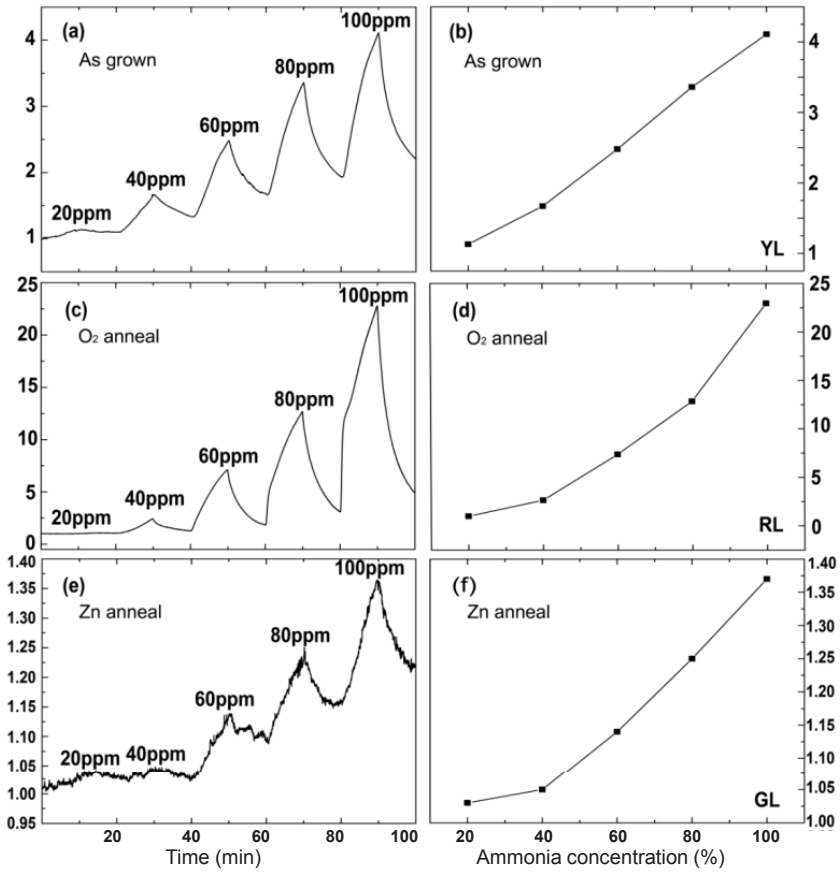

FIGURE 5.7: Electrical conductance sensitivity of ZnO nanorods to gaseous NH_3 for (a) as-grown; (c) O_2 annealed; and (e) Zn vapour annealed samples. Figures (b), (d) and (f) show the corresponding ratio of the chance in conductivity as a function of NH_3 concentration. Data collected by Suranan Anantachaisilp.

NH_3. Zn vapour annealed ZnO exhibited a comparatively small change in conductivity, increasing by a factor of 1.37, while as-grown ZnO increased by an intermediate factor of 4.1.

EPYS spectra collected continuously during the introduction of NH_3 into the chamber are shown in Figures 5.8, 5.9 and 5.10 for as-grown, oxygen annealed and zinc annealed ZnO respectively. The inset of each figure shows a log-linear plot of the EPYS spectra. In the case of all three samples, the presence of NH_3 resulted in a decrease of the photoelectron emission threshold. Photoelectron emission threshold began to decrease at the point when NH_3 was introduced into the chamber and was present in a relatively low concentration compared to argon. The decrease continued for each sample as the NH_3 concentration increased, until after the chamber was purged and the amplification gas completely replaced by pure NH_3, at which point the threshold began to converge to a steady state value.

The photoelectron emission threshold for as-grown ZnO began (in argon) at 4.61 eV and decreased to 4.02 eV in a majority NH_3 environment. O_2 annealed ZnO, which exhibited a native photoelectron emission threshold at 4.47 eV, showed a strong response to the presence of NH_3 as its photoelectron emission threshold decreased to 4.21 eV and its photoelectron emission strength increased significantly in comparison to the other samples, given the environmental conditions in which the spectra were collected were identical. The photoelectron emission threshold of Zn vapour annealed samples, initially 4.12 eV in argon, decreased to 3.97 eV in when in a majority NH_3 environment.

5.5 Discussion

Changes in surface electronic structure, and optical and electrical properties can be understood by considering the roles of native defects and impurities on the band structure of ZnO. High electrical resistivity and strong YL exhibited by the hydrothermally

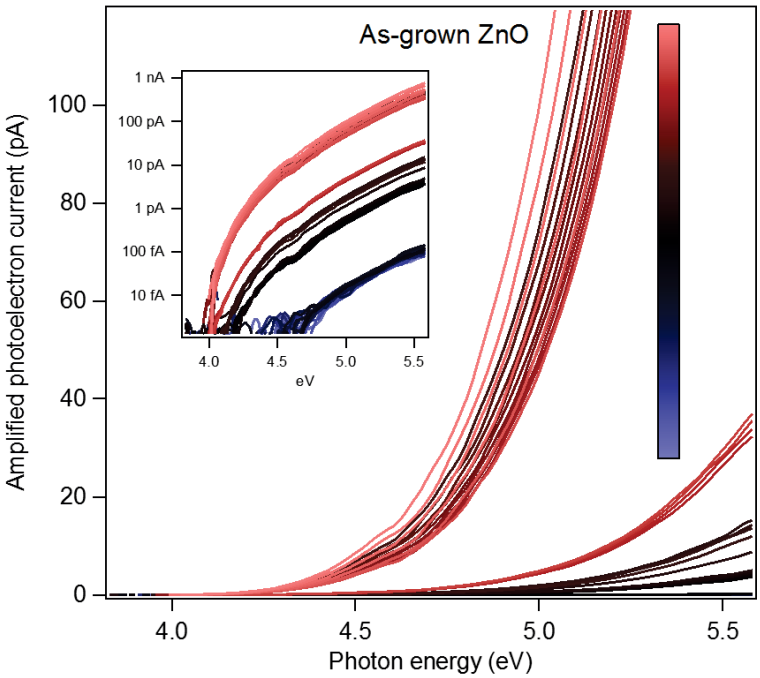

FIGURE 5.8: EPYS spectra from as-grown ZnO nanorods collected in an environment transitioning from argon into gaseous NH_3. The blue traces were collected initially in a dry, argon environment, and the pale red traces were collected in a NH_3 environment. Inset shows the spectra on a log-linear scale. As the partial pressure of NH_3 increases, the photoelectron emission threshold decreases. The gaps in the spectra are periods during which NH_3 is introduced to the chamber: spectra were not collected during this period as the detector bias had to be adjusted to compensate for the changing amplification medium.

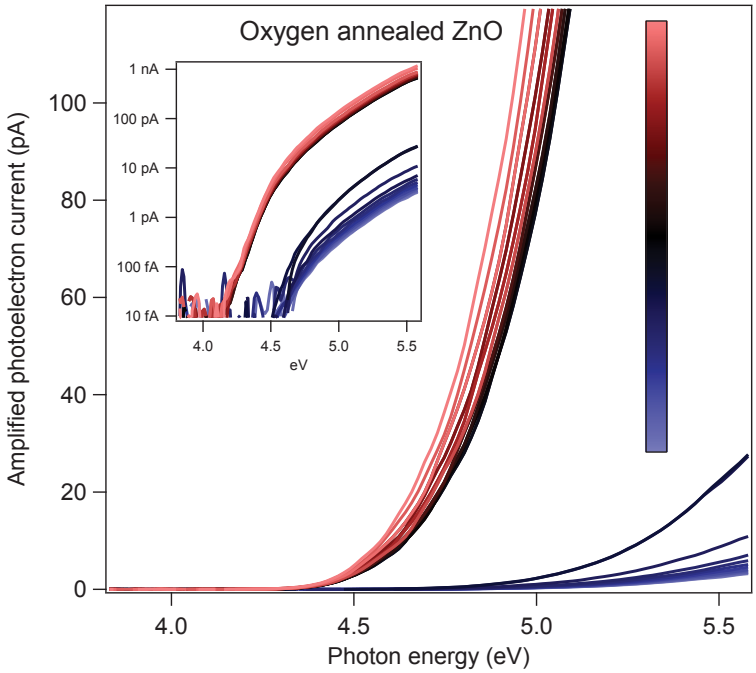

FIGURE 5.9: EPYS spectra from oxygen annealed ZnO nanorods collected in an environment transitioning from argon into gaseous NH_3. The blue traces were collected initially in a dry, argon environment, and the pale red traces were collected in a NH_3 environment. Inset shows the spectra on a log-linear scale. As the partial pressure of NH_3 increases, the photoelectron emission threshold decreases.

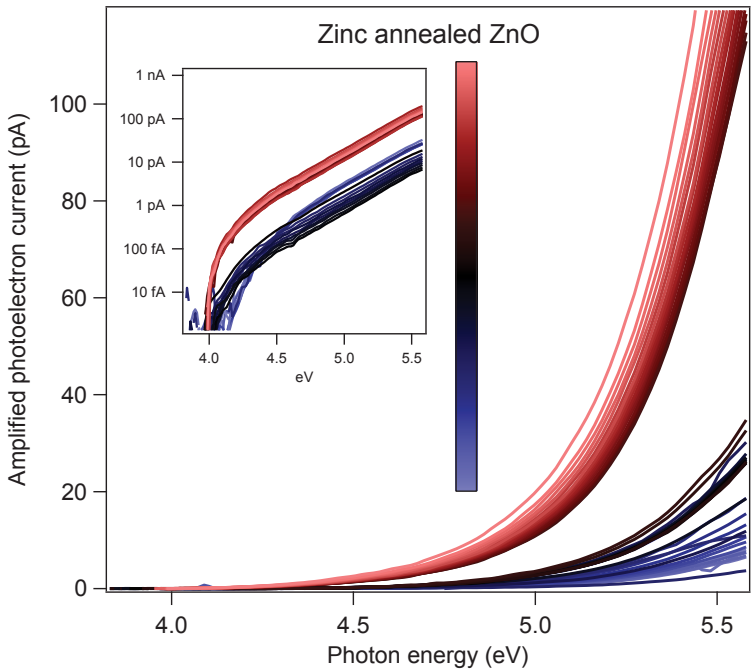

FIGURE 5.10: EPYS spectra from zinc annealed ZnO nanorods collected in an environment transitioning from argon into gaseous NH_3. The blue traces were collected initially in a dry, argon environment, and the pale red traces were collected in a NH_3 environment. Inset shows the spectra on a log-linear scale. As the partial pressure of NH_3 increases, the photoelectron emission threshold decreases.

as-grown nanorods is consistent with the presence of Li acceptor states incorporated during growth. The YL has previously been attributed to DAP recombination, in which Li plays the role of a deep acceptor facilitating the recombination pathway [138, 191, 196]. Li acceptors compensate their donor counterparts - such as H - decreasing the native background free carrier concentration and leading to a high electrical resistivity. It is thought that annealing ZnO post-growth at 650°C causes the breakup of Li based complexes such as Li-H, eliminating the DAP recombination pathway and allowing the shallow donors to contribute free n-type carriers to the conduction band. The result of breaking Li-donor complexes is a removal of the YL and an increase in electrical conductivity, which is consistent with the results of both CL and electrical characterisation by Suranan Anantachaisilp [158, 195].

It is inferred that annealing the nanorod samples in O_2 and Zn vapour leads to a change in stoichiometry of the ZnO surface by incorporating oxygen (or depleting zinc) and incorporating zinc into the crystal lattice respectively. Oxygen rich (i.e. O_2 annealed) ZnO possesses a relatively high concentration of V_{Zn} at the surface (which are more likely to occur than O_i due to the lower formation energyof V_{Zn}). Zinc rich ZnO (i.e. Zn vapour annealed) will most likely contain a relatively high concentration of V_O due to the incorporation of excess Zn into the lattice near the nanorod surface.

The O_2 annealed samples exhibited a distinct absence of the YL, a strong RL and small contribution from the GL. Furthermore, an increase in the electrical conductivity by two orders of magnitude from the native, as-grown state was observed. The strong RL is believed to arise from formation of V_{Zn} defects or, to a lesser extent, O_i, which have the lowest formation energies of intrinsic defects in n-type, oxygen rich ZnO. V_{Zn} is a deep acceptor and would thus only be expected to affect the conductivity by compensating local shallow donors. The GL present in O_2 annealed samples is comparable to the strength of the NBE emission, similar to the zinc-vapour annealed samples. The GL is proposed to arise from radiative recombination associated with V_O defects by the majority of recent investigations into defect luminescence of ZnO.

Zinc-vapour annealed ZnO exclusively exhibited GL and NBE emission, whilst possessing the highest electrical conductivity of the three samples. The formation of V_O near the surface is expected to induce a slight downward band bending, due to the addition of

donor states to the bandgap, and thus locally increase the n-type carrier density in the form of an accumulation region.

The photoelectron threshold observed in these cases marks the ZnO work function, which has been shown to vary from 4.4 to 3.5 eV with increasing carrier density [16, 197]. Several values for the ZnO work function have been reported in different studies, varying with dopant type, concentration [194, 198] and surface termination [199, 200] ranging from 3.5 and 6 eV. The ionisation potential of ZnO has been reported to be 7.68 eV, as measured using UPS, with a corresponding room temperature band gap and electron affinity of 3.37 and 4.35 eV respectively [201]. Variations in the work function are typically attributed to the Fermi level shifting with free carrier density, while electron affinity and ionisation potential have been shown to vary in some cases due the presence of surface states and chemisorbed species generating surface dipole fields. The energy difference between the conduction band minimum and the Fermi level is given by

$$E_C - E_F = \phi - \chi = k_B T ln\left(\frac{N_D}{n_e}\right) \tag{5.1}$$

where k_b is Boltzmann's constant, T is temperature in Kelvin, N_D is the effective density of states of the conduction band ($\sim 3 \times 10^{18}$ cm^{-3}) and n_e is the conduction band electron density. Assuming the electron mobility is relatively similar between the ZnO nanorod samples, which is reasonable considering the consistency of reported mobility in variously doped ZnO [137] - approximately 150 cm^{2}V^{-1}s^{-1} - a change in electrical conductivity will primarily be due to a difference in free carrier concentration. Changes in free, n-type carrier density of two orders of magnitude (for the purpose of providing an example - from 10^{15} to 10^{17} cm^{-3}) as observed in these samples correspond to a Fermi level shift of approximately 0.13 eV, from 0.2 eV to 0.07 eV below the conduction band minimum. This corresponds extremely well with the difference between the photoelectron threshold of as-grown and O_2 annealed ZnO nanorods, 4.61 and 4.47 eV respectively. The difference in work function of these samples, as measured by EPYS, is therefore attributed to a Fermi level shift arising from the significantly different carrier densities in as-grown and oxygen annealed ZnO samples.

Assuming these threshold values represent the work function, however, places the surface Fermi level at, or slightly above the conduction band minimum, for an ionisation

potential of ∼7.7 eV. This indicates that a small amount of downward band bending must be occurring at the as-grown and oxygen annealed ZnO surface, which also has been corroborated with X-ray absorption near edge structure (XANES) experiments performed on these samples [195]. The downward band bending was attributed to the adsorption of donor surface states, the most likely of which, although not conclusively identified, have been suggested to be chemisorbed H_2O and OH molecules [195]. A band diagram representing the relative Fermi levels and work functions of the ZnO samples is shown in Figure 5.11.

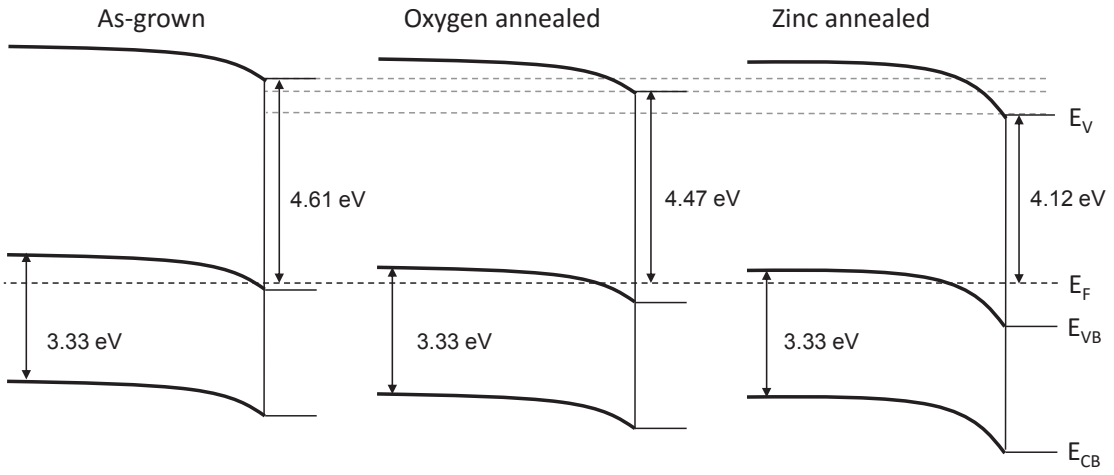

FIGURE 5.11: Band diagrams for the as-grown, oxygen annealed and zinc annealed ZnO samples. The Fermi level sits higher with respect to the conduction and valence bands in oxygen annealed and zinc annealed samples, and the zinc annealed ZnO exhibits greater downward band bending due to the presence of V_o.

The zinc annealed sample possessed a photoelectron threshold of 4.12 eV, much lower than both the as-grown and the oxygen annealed sample. This decrease in work function is not unexpected, though, for such high conductivity ZnO. This is especially in the zinc rich case, where the intrinsic, near-surface defect population is supposed to be dominated by V_O. The presence of V_O defects near the ZnO surface would lead to further band bending due to the dipole field generated by the presence of excess charge carriers, free or donor bound. The band diagram representing the zinc annealed ZnO case is also shown in Figure 5.11, and while the Fermi level is situated at the same energetic position with respect to the bulk conduction band minimum as in oxygen annealed ZnO, the extent of downward band bending at the zinc annealed ZnO surface is greater by 0.35 eV.

The model of band bending proposed and schematically represented in Figure 5.11 is consistent with CL, electrical conductivity and EPYS measurements performed as a part

of this study. The downward band bending occurring in as-grown and oxygen annealed ZnO has been corroborated with XANES. It follows from consideration of the n-type nature of V_O defects that ZnO samples annealed in a zinc-vapour environment should exhibit downward band bending to a greater extent than both as-grown and oxygen annealed samples.

5.5.1 Sensitivity to NH_3

Electrical sensitivity measurements demonstrated a clear increase in conductivity of ZnO when exposed to gaseous NH_3. The respective sensitivity of as-grown, oxygen annealed and zinc vapour annealed samples did not appear to correlate with their corresponding native conductivity. Specifically, the sample exhibiting the strongest electrical response to NH_3 (oxygen annealed ZnO) possessed an intermediate native conductivity, while the most resistive (as-grown) and the most conductive (zinc annealed) responded to NH_3 to a significantly lesser extent. Of note is the reversibility of the electrical conductivity, in particular, for the O_2 annealed ZnO sample - a promising characteristic for use in gas sensing devices.

The physical mechanism generally proposed to result in an electrical response of ZnO to NH_3 is a gas-adsorbate reaction leading to the donation of electrons from adsorbates to the ZnO surface. The reaction proposed is as follows: $4\,NH_3 + 3\,O^- \longrightarrow 6\,H_2O + 2\,N_2 + 3e^-$. However, this model is inconsistent with the CL analysis of ZnO defects in this study. It is widely accepted that the presence of V_O enhances oxygen adsorption via dissociative chemisorption of O_2 molecules [202, 203]. One would expect, in this case, that zinc annealed ZnO, containing a relatively high concentration of V_O - evidenced by its GL - would also exhibit the highest O^- coverage and subsequently the strongest electrical sensitivity to NH_3.

Time-resolved EPYS measurement of the photoelectron emission profile in the response of NH_3 shows a decrease in the photoelectron emission threshold with increasing NH_3 concentration. This strongly suggests that the presence of NH_3 results in electron donation to the ZnO surface, although the exact mechanism facilitating this process remains elusive. Due to the fact that all three samples (as-grown, oxygen annealed and zinc annealed) exhibited a decrease in photoelectron emission threshold to approximately 4 eV, it appears most probable that the reason for the decrease is Fermi level pinning at the

ZnO surface to the chemical potential of NH_3. This would explain the similar thresholds of all three samples, as their respective Fermi levels would be referenced to the same chemical potential in each case. The greatest hurdle faced by EPYS in this case - for continuous monitoring of changes in the environmental composition - was the changing partial pressures of the two amplification gases, both of which exhibit significantly different amplification characteristics.

The ability to monitor this process in real-time - despite a requirement to change detector settings midway in this case - is an example of an application of EPYS in the characterisation of surface electronic structure responding dramatically to different species of ambient gas. These types of experiments, specifically employing photoelectron emission spectroscopy, are completely novel and the first of their kind.

There are a number of simple considerations that would overcome the issues associated with photoelectron amplification in future studies of this kind. These include characterisation of a variety of gases that would be suitable for such an experiment, so that one may have the criteria for selecting gas mixes that would have similar gas cascade characteristics. Increasing the effective collection time for these measurements would serve to increase the dynamic range by decreasing the electrical noise, and thus normalising EPYS spectra post-processing would allow quantitative comparison of threshold values, even in cases where amplification or photoelectron emission strength varies dramatically between gas species.

5.6 Conclusion

EPYS has been employed as a correlative technique for the characterisation of ZnO in a broader study of its defect structure, optical and electrical properties. It has been used to identify different work functions of ZnO samples that, when correlated with electrical and optical properties, has led to the development of a self-consistent model of subsurface defects and their effects on the band structure of hydrothermally grown ZnO nanorods.

As-grown ZnO nanorods contain deep Li acceptors that facilitate the YL and result in low conductivity. A low concentration of n-type carriers is corroborated with the highest work function of all samples as measured by EPYS, and slight downward band

bending at the surface places the Fermi level close to the conduction band minimum. Annealing ZnO nanorods in oxygen breaks up Li-donor pairs, causing an increase in the conductivity and a loss of the YL, while the formation of V_{Zn} introduces the RL. A slight decrease in the work function corresponds highly with an upward Fermi level shift arising from the increased n-type carrier concentration (which is also suggested by an increased photoelectron emission strength). Annealing ZnO nanorods in zinc vapour results in the highest electrical conductivity, and an exclusively green defect related luminescence. The lowest work function was observed in zinc annealed ZnO, and it has been attributed to downward band bending at the ZnO surface arising from the presence of near-surface V_O donor states which also explains the strong GL and high conductivity.

ZnO has been shown to have a strong, electrical response to the presence of NH_3 vapour, increasing in conductivity upon exposure to the gas. This sensitivity has been probed using real-time EPYS measurements, demonstrating a completely novel capability of the EPYS system that had never previously been performed. The photoelectron emission threshold was observed to decrease with increasing NH_3 partial pressure, to approximately 4 eV for all samples, indicating a surface Fermi level pinning to an adsorbate chemical potential - most likely NH_3.

5.7 Implications

ZnO is a promising candidate for a variety of impending technologies based in optoelectronics, such as solid state lighting, solar energy harvesting, UV lasers and many other applications for radiation hard, visibly transparent and electrically conductive material. Gas sensing has more recently been identified as another application of ZnO, and this study has identified specifically that it is capable of identifying the presence of NH_3 to levels below 20 ppm in atmosphere. Understanding the defect and electronic structure of ZnO nanostructures brings these technologies one step closer, enabling predictive device design for future development projects.

Another aspect of this study that has implications for the future of solid-gas interface characterisation is the realisation of real-time photoelectron emission yield spectroscopy

in changing environments. A capability of the EPYS system to probe the surface electronic structure of ZnO, as the gaseous environment around it changes, has been demonstrated. This capability is of great interest to the nanoscience community, and should prove to be of great value in the future of materials physics, chemistry and in the biological sciences.

Chapter 6

Application of EPYS: in-situ study of surface functionalisation

6.1 Summary

In the following chapter, EPYS is used to elucidate a spontaneous exchange reaction that takes place between chemisorbed hydrogen and physisorbed fluorine on diamond. A result of this reaction is the charge state switching of near-surface nitrogen-vacancy (NV) defects from neutral to negative, which has significant implications for the development of diamond based quantum technologies. Using the reaction identified by EPYS, an electron beam-directed technique for controlling the charge states of near-surface NVs in diamond was developed. The electron beam fluorination process is highly localised and can be used to control the emission spectrum of individual nanodiamonds and surface regions scanned by the electron beam.

6.2 Introduction

Diamond is a dense face-centred cubic lattice of carbon atoms (a member of the Fc3m space group). Diamond typically contains impurity substitutional atoms (e.g. Ni, Co, N, and Br [204]) depending on its growth or formation process. Impurities may also be intentionally incorporated during growth and by ion implantation [205, 206]. A complex point defect composed of a substitutional nitrogen atom adjacent to a carbon vacancy is

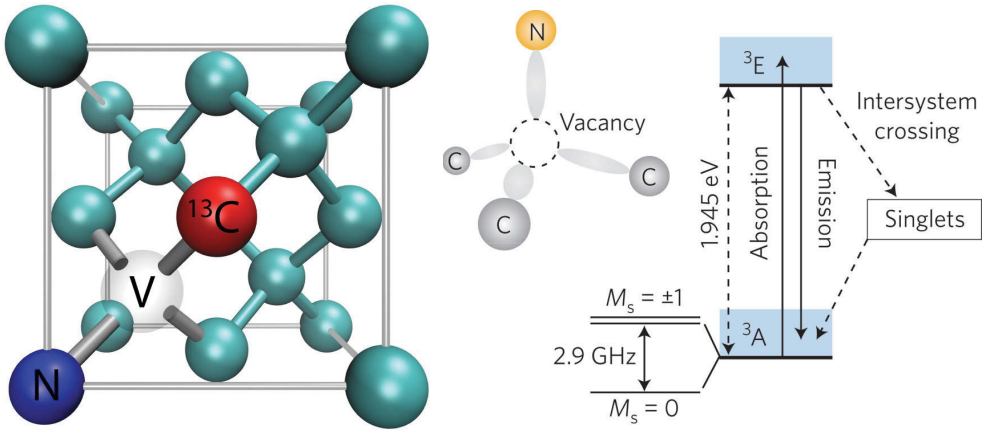

FIGURE 6.1: The diamond crystal lattice structure (left) containing a NV defect and the electronic structure of the NV^- in diamond (right) [211].

known as a nitrogen-vacancy (NV) centre. A NV centre may exist in one of two charge states - neutral or negative - with a single unpaired electron or two unpaired electrons respectively. The electronic structure of the negatively charged NV centre is of C3v symmetry, containing triplet ground and excited states and a non-radiative metastable singlet state shown in Figure 6.1 (right) [207–210].

The diamond NV centre, comprised of a substitutional nitrogen atom adjacent to a carbon vacancy, is the subject of intense research into qubits for use in quantum computing [212], markers for live cell imaging [213–215], and sensors of extremely weak electric and magnetic fields [216–218]. These applications are made possible by the fact that the spin states of individual NV^- centres can be manipulated deterministically and read out optically at room temperature [212, 216–220], and that diamond is a non-toxic bio-compatible material [221–224]. However, the charge state of NV^- centres can be unstable, and must be controlled to enable optimal exploitation in photonic and spintronic applications [225–227]. Shallow NV^- centres located near a diamond surface are particularly significant for coupling NV centres to on-chip waveguides and cavities, and sensors that have high spatial resolution [228, 229].

6.2.1 Nitrogen-vacancy centre in diamond

The discovery of single negatively charged nitrogen-vacancy (NV^-) colour centres marked a critical point in the evolution of diamond-based quantum technologies [208, 230, 231]. The detection of single centres soon enabled demonstrations of photostable single photon generation [232, 233], which highlighted the NV^- centre for implementation in quantum

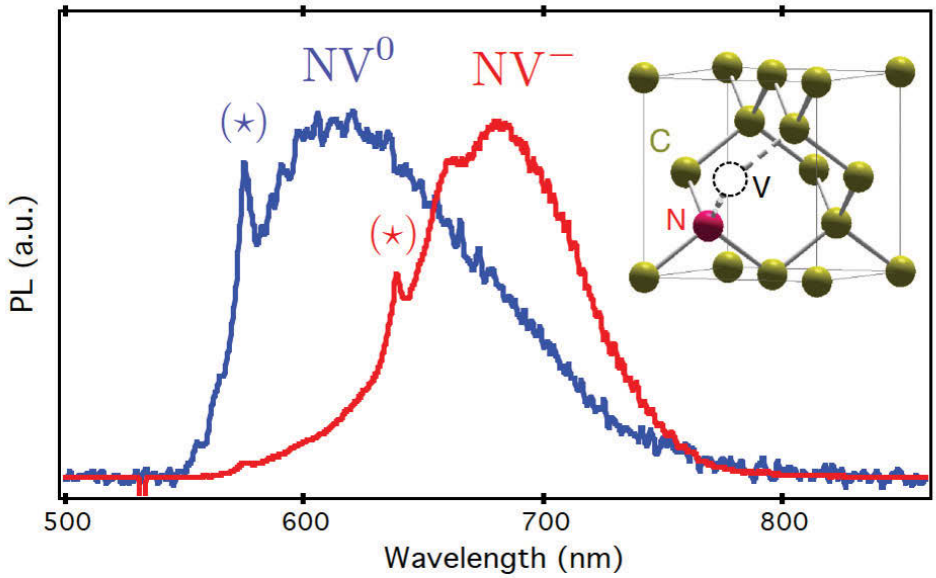

FIGURE 6.2: Characteristic photoluminescence spectra of the NV^- (red) and NV^0 (blue) defects in diamond.

optical networks, as well as demonstrations of optical preparation and readout of the centre's electronic spin [210, 234–237]. This identified the NV^- centre as a possible solid state spin qubit suitable for quantum information processing and quantum metrology devices [230, 238]. Following these demonstrations, the growth of research into the NV^- centre and the development of applications of the centre have been incredibly rapid and a number of important milestones have been reached [207, 208, 231, 236, 239].

NV^- ground state can be prepared by optical pumping of the defect, due to an efficient spin-flipping, non-radiative recombination from the $m_s = \pm 1$ excited state to the $m_s = 0$ ground state [210, 234]. Continuous, high flux irradiation of a NV^- by photons of energy greater than 1.95 eV populates the $m_s = 0$ state, as excited $m_s = 0$ states can only undergo spin preserving recombination, while $m_s = \pm 1$ excited states may relax via a spin-flipping metastable state to the $m_s = 0$ ground state. Furthermore, deterministic, resonant spin-flipping between the $m_s = \pm 1$ and $m_s = 0$ ground state has been demonstrated using radio frequency magnetic fields [210, 234, 237, 240]. Identification of the ground state spin resonant frequency of NV^- was enabled by the ability to infer initial ground state spin based on the strength of its photoluminescence. The ground state spin can be read out optically; the strength of NV^- photoluminescence is directly proportional to the relative populations of its ground state spin levels.

The NV^0 does not possess this stable, optically observable, magnetic sensitivity, and

is thus not a desirable charge state of NV centres for the development of spin-based technologies [210, 231, 241, 242]. However, they are typically present near the diamond surface due to upward band bending, which shifts the energy level of NVs well above the Fermi level where they are far less likely to accept an electron from the valence band.

The identifying features of NV^- and NV^0 are their optical zero phonon lines (ZPLs) at 1.945 eV (637 nm) and 2.156 eV [173, 243], respectively, and associated vibronic bands that extend from their ZPLs to lower energy in emission, shown in Figure 6.2. The sharp ZPLs and well defined vibronic bands of NV^- and NV^0 indicate that the optical transitions occur between discrete defect levels that are deep within the diamond bandgap. Both charge states have sufficiently strong fluorescence to be detected as single centres using scanning confocal microscopy [173].

6.2.2 Hydrogen and fluorine terminated diamond

6.2.2.1 Hydrogen terminated diamond

Intrinsic diamond, with a band gap of 5.5 eV, is an insulator in the bulk phase [244–246]; however, hydrogen terminated diamond exhibits a very high surface conductivity [247, 248]. This high p-type electrical conductivity has previously been attributed to hydrogen related defects acting as acceptor states [246], although more recently, experimental evidence has been presented demonstrating that hydrogen is a requirement for surface conductivity but that exposure to air was also necessary [248]. The proposed mechanism for this behaviour was a redox reaction with adsorbed water overlayers that facilitates a p-type accumulation layer at the diamond surface. A brief overview of this work is presented below.

Surface conductivity in diamond has been confirmed many times over the years [247, 249–251]. The carrier concentration and Hall mobility of carriers was found to vary little with temperature, and the mobility was always similar to B-doped diamond, indicating a conductive surface pathway. The surface conductivity was only observed in H-terminated diamond and disappeared after dehydrogenation or oxidation of the surface.

As a result, the conductivity was attributed directly to the presence of hydrogen, as an unidentified shallow acceptor [249, 252]. Maier et al monitored the conductivity and

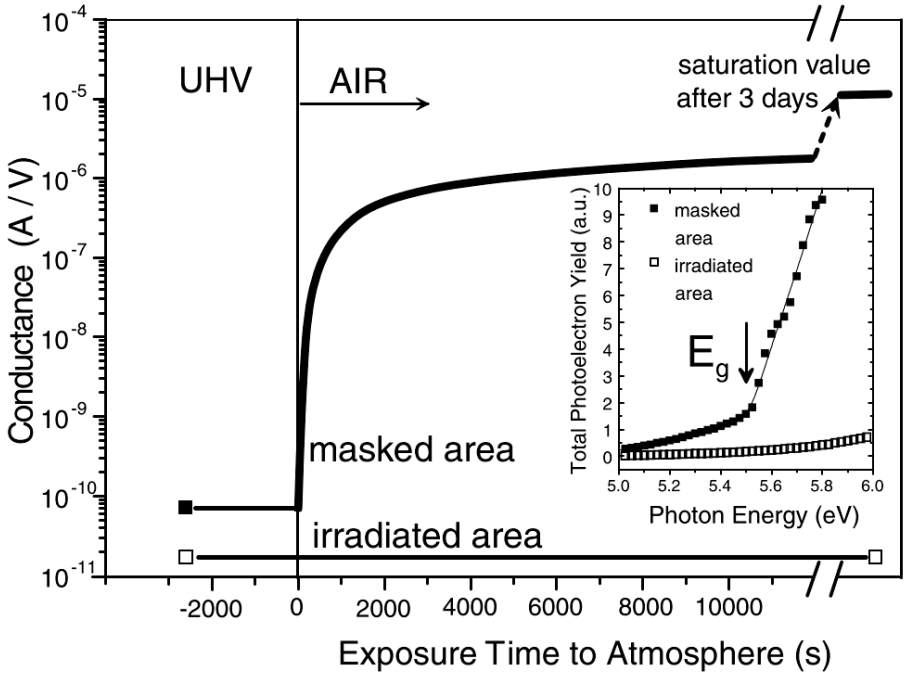

FIGURE 6.3: Electrical conductivity data from Maier et al. [248] showing the change in surface conductivity when hydrogen terminated diamond is exposed to air.

electron affinity of a variety of diamond samples in air and in UHV conditions while thermally treating and dehydrogenating by electron bombardment in UHV [248]. The experiments were performed as follows. The conductance of diamond in air was measured and found to be in agreement with the high conductance previously observed while the NEA characteristic of hydrogen terminated diamond was confirmed with photoelectron emission spectroscopy. The sample was then annealed at 100 °C in UHV for 20 minutes during which period the conductance dropped by 6 orders of magnitude.

However, thermal desorption of hydrogen does not begin below 700 °C. Localised dehydrogenation was performed by irradiating a selected area with an electron beam and then confirmed, using photoelectron emission spectroscopy to observe the loss of NEA in the irradiated region. The sample was subsequently exposed to air while the conductivity of both hydrogen-terminated and dehydrogenated regions were monitored and the surface conductivity only returned to the unirradiated (hydrogen terminated) region. The conductivity data are shown in Figure 6.3

It was found that the UHV annealing step was required for the drop in conductivity to occur, indicating that an additional ingredient from the air is necessary for the formation of surface conductivity, and that it desorbs above approximately 100 °C in UHV.

Further characterisation of annealed and unannealed hydrogen terminated diamond was performed with IR spectroscopy that identified the C-H stretching modes in unannealed diamond that progressively vanished by annealing at higher temperature and for longer periods.

Direct electron transfer into atmospheric adsorbates is highly unlikely due to the low electron affinities of molecular adsorbates (2.5-3.7 eV) relative to the VBM of diamond, which sits at 4.2 eV below the vacuum energy of free electrons. However, the presence of acceptors in a water overlayer, which forms naturally on all surfaces in atmosphere, is able to facilitate electron exchange from the diamond surface due to the chemical potential of electrons in a liquid phase (μ_e) falling below the diamond VBM. Due to the CO_2 content in the air, the water overlayer develops an excess of H_3O^+ ions, causing the pH to drop. The lower pH decreases μ_e according to the Nernst's equation:

$$\mu_e = \mu_0 - (kT/2)ln\left[\frac{([H_3O^+]/[H_3O^+]_{SHE})}{([H_2]/[H_2]_{SHE})}\right] \tag{6.1}$$

where μ_0 is the chemical potential for electrons under Standard Hydrogen Electrode (SHE) conditions. This relationship leads to a chemical potential of the aqueous wetting layer, μ_e of -4.26 eV. With a NEA of hydrogen terminated diamond of -1.3 eV, μ_e is positioned approximately 50 meV below the VBM; thus, electron transfer to the aqueous H_3O^+ acceptors may take place and the Fermi level pinning results in upward band bending at the diamond surface. A schematic for this process is shown in Figure 6.4

6.2.2.2 Fluorine terminated diamond

Hydrogen terminated diamond is renowned for its unique NEA [113, 253–255]. Termination of the diamond surface by oxidative species such as fluorine, however, results in the formation of a surface dipole field that causes downward band bending, and leads to a positive electron affinity [256–260]. This effect has been reported with both fluorine and oxygen termination. Typically oxygen termination is achieved by exposing the sample to oxygen plasma [252, 261], while fluorine termination has reportedly been achieved in a number of ways - including spontaneous dissociative chemisorption upon exposure of the surface to both elemental and molecular fluorine [93, 259, 260]. Fluorination has also

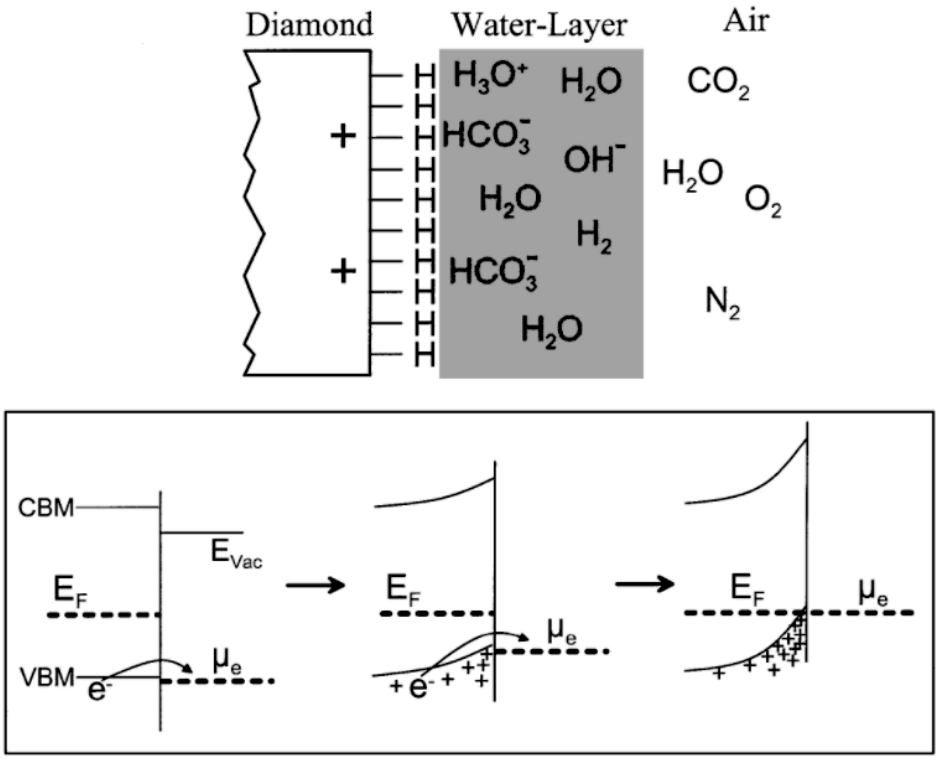

FIGURE 6.4: Top: Schematic of the hydrogenated diamond surface in contact with a H_2O overlayer taken from Maier et al. [248]. Bottom: Evolution of the band bending during the electron transfer process at the interface between diamond and the H_2O overlayer.

previously been observed to occur upon exposure of hydrogen terminated diamond to elemental fluorine by way of a spontaneous exchange mechanism between the chemisorbed hydrogen and ambient fluorine [262].

An increase in the electron affinity, χ (accompanied by an increased ionisation potential, ζ) is the result of dipole field setup in the $C^{\delta+}$-$F^{\delta-}$ surface bond [263]. The downward band bending that results from this highly polar bond also shifts near-surface defect energy levels downward with respect to the Fermi level [225]. As defect states shift from above to below the Fermi level, the defect may undergo a change in their charge state. This effect has been demonstrated in the case of both fluorine and oxygen terminated diamond [252, 264–266].

This study employs a spontaneous exchange reaction between chemisorbed hydrogen and molecular fluorine that can be inhibited by a water overlayer to locally control the charge state of near surface defects in diamond.

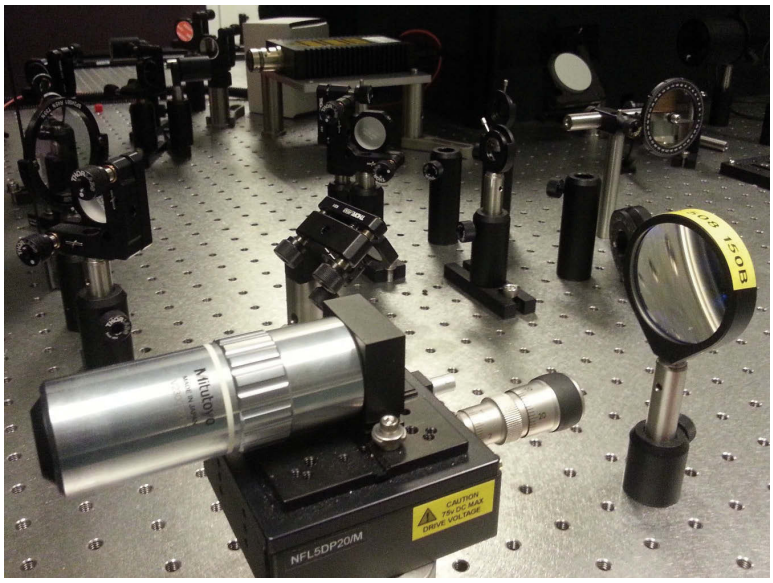

FIGURE 6.5: Photograph of the confocal photoluminescence setup used in this study. The lens in the foreground focuses excitation light into a 0.5 μm^2 spot on the sample, and also collects the photoluminescence from the sample.

6.3 Experimental methods

This following section presents a thermally activated method and an electron beam-directed technique for switching the surface termination and charge states of shallow NV centres in diamond. Specifically, fluorination of the surface of H-terminated diamond is facilitated by removal of a H_2O overlayer by annealing the diamond in vacuum then exposing to NF_3 or by electron beam irradiation in the presence of NF_3 respectively. The relative population of NV charge states were identified by the strength of their characteristic photoluminescence spectra.

A boron doped polycrystalline diamond film was used in the EPYS measurements to avoid spurious photoelectron emission from a substrate, while Type IIb nanodiamonds, 35 nm in diameter, dispersed onto a Si substrate were used for confocal photoluminescence measurement. Both samples were first treated in oxygen plasma for one hour (30 W, 0.3 mBar, 13.42 MHz) to remove residual hydrocarbon contaminants, and subsequently exposed to hydrogen plasma for one hour (30 W, 0.3 mBar, 13.42 MHz) to ensure a H-terminated surface. H-termination of the diamond film was verified with EPYS, by way of observing the low photoelectron threshold and strong photoelectron emission strength characteristic of NEA surfaces, while the H-terminated nanodiamonds were characterised with photoluminescence measurements.

6.3.1 Thermally activated fluorination

EPYS spectra were first obtained from boron doped polycrystalline H-terminated diamond in a H_2 environment at 2 Torr. The chamber was then evacuated of H_2 and the diamond sample heated to 100 °C at a pressure of 6×10^{-8} mBar for one hour. NF_3 was subsequently introduced into the chamber, bringing it to a pressure of 2 mBar. EPYS spectra were then collected from the diamond sample in the presence of NF_3.

Critically, to investigate the importance of the annealing step, similar experiments were performed in which H_2 was replaced by NF_3 without thermally annealing in high vacuum, and also when H_2 is re-introduced after the annealing step instead of NF_3.

The nanodiamonds underwent the sample exposure cycles as the diamond film, both with and without the thermal annealing step, carried out in the EPYS chamber, although EPYS spectra were not collected due to unwanted photoelectron emission from the Si substrate. The nanodiamonds were then characterised ex-situ with a confocal photoluminescence (PL) setup (photograph shown in Figure 6.5 and schematic of the setup in Figure 6.6). PL spectra were collected in air using a 532 nm excitation laser with a spot size of 0.5 μm^2.

6.3.2 Electron beam induced fluorination

Analogous measurements to thermally activated fluorination were performed on both polycrystalline diamond film and the nanodiamond samples, replacing the thermal annealing step with electron irradiation in the presence of NF_3. The fluorination was verified ex-situ using EPYS in the case of polycrystalline diamond, and PL in the case of nanodiamonds.

EPYS spectra were first collected from the polycrystalline diamond in a H_2 environment. The EPYS chamber was then vented, and the sample loaded into a variable pressure electron microscope. A region 3mm × 3mm was rastered with a 20 kV, 142 nA defocused electron beam for five hours (corresponding to a primary electron fluence of $1.8 \times 10^3 nm^{-2}$) in 0.13 mBar of NF_3. The sample was subsequently loaded back into the EPYS chamber, and EPYS spectra were collected from the electron-irradiated region in an NF_3 environment at 2 mBar.

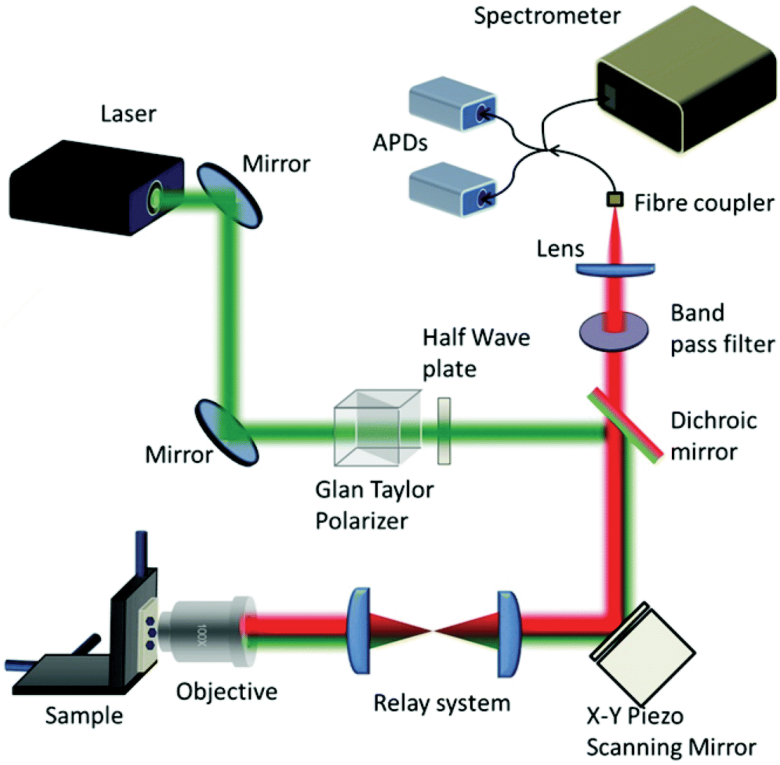

FIGURE 6.6: A schematic of the confocal photoluminescence setup used in this study. A 532 nm excitation laser is directed onto the sample, and its x-y position at the sample surface scanned using a piezoelectric scanning mirror. Emitted and reflected light returns along the path of the excitation laser until they are separated at a dichroic mirror. The photons generated by the sample are allowed to pass through the dichroic mirror, where they are detected by avalanche photodiodes for panchromatic mapping, and/or a spectrometer.

Similarly, PL spectra were collected from the hydrogen plasma treated nanodiamonds, then loaded into a variable pressure electron microscope. The electron beam process used to switch the charge state of NV centres is shown schematically in Figure 6.8 (a). A 20×20 μm^2 region containing the nanodiamonds was then rastered with a 20 kV, 0.51 nA electron beam for one hour beam (corresponding to a primary electron fluence of 2.9×10^4nm^{-2}) in a 5 mBar, NF_3 environment. Confocal PL spectra were then collected from nanodiamonds inside and outside of the electron irradiated region, and panchromatic PL maps were also collected from the electron irradiated regions.

6.4 Results

The EPYS spectra (Figure 6.7) from polycrystalline diamond show that H-terminated diamond had an electron emission threshold of 4.55 eV, and that it increased to 5.84 eV

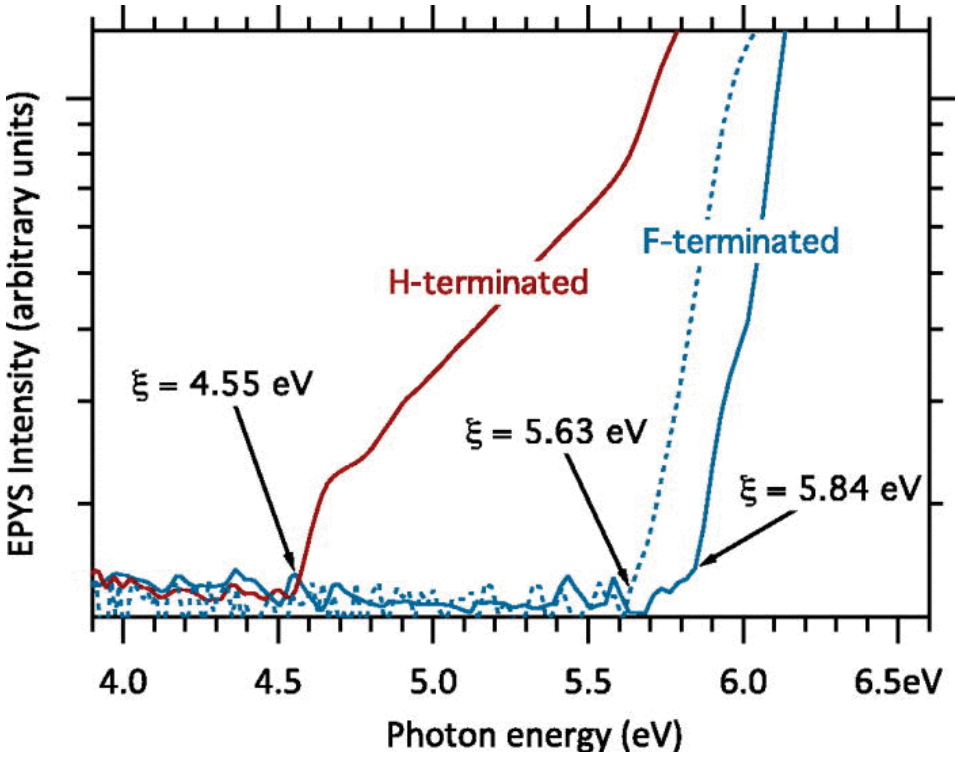

FIGURE 6.7: Normalised photoelectron yield spectra of H-terminated diamond (acquired in a H_2 environment) and F-terminated diamond (acquired in NF_3 vapour). The latter were generated by thermal (solid line) and electron beam (dashed line) induced fluorination.

after annealing and exposure to NF_3. Importantly, the threshold remains at 4.55 eV if the annealing step is skipped and H_2 is simply replaced with NF_3. The threshold also does not change when the water overlayer is removed and H_2 is re-introduced; however in this case an increase in the photoelectron emission is observed.

The dashed blue line in Figure 6.7 shows the EPYS spectra collected ex-situ from the region irradiated by an electron beam in NF_3. This region exhibited sightly lower photoelectron threshold than the sample studies in-situ by thermally activated fluorination.

Photoluminescence spectra taken from unexposed and electron-irradiated regions of the sample are shown in Figure 6.8 (c), along with a panchromatic photoluminescence map of the sample (d). The spectra shown in Figure 6.8 (c) are also representative of the PL profiles from H-terminated nanodiamonds and those that were exposed to NF_3 after thermally annealing in high vacuum (red and blue, respectively). The spectra show that, in the electron-irradiated region (as in the thermally annealed nanodiamonds), the intensity of the NV^- zero phonon line is greater than that of the corresponding NV^0 emission. Conversely, in the unexposed region (and hydrogen plasma treated nanodiamonds), the

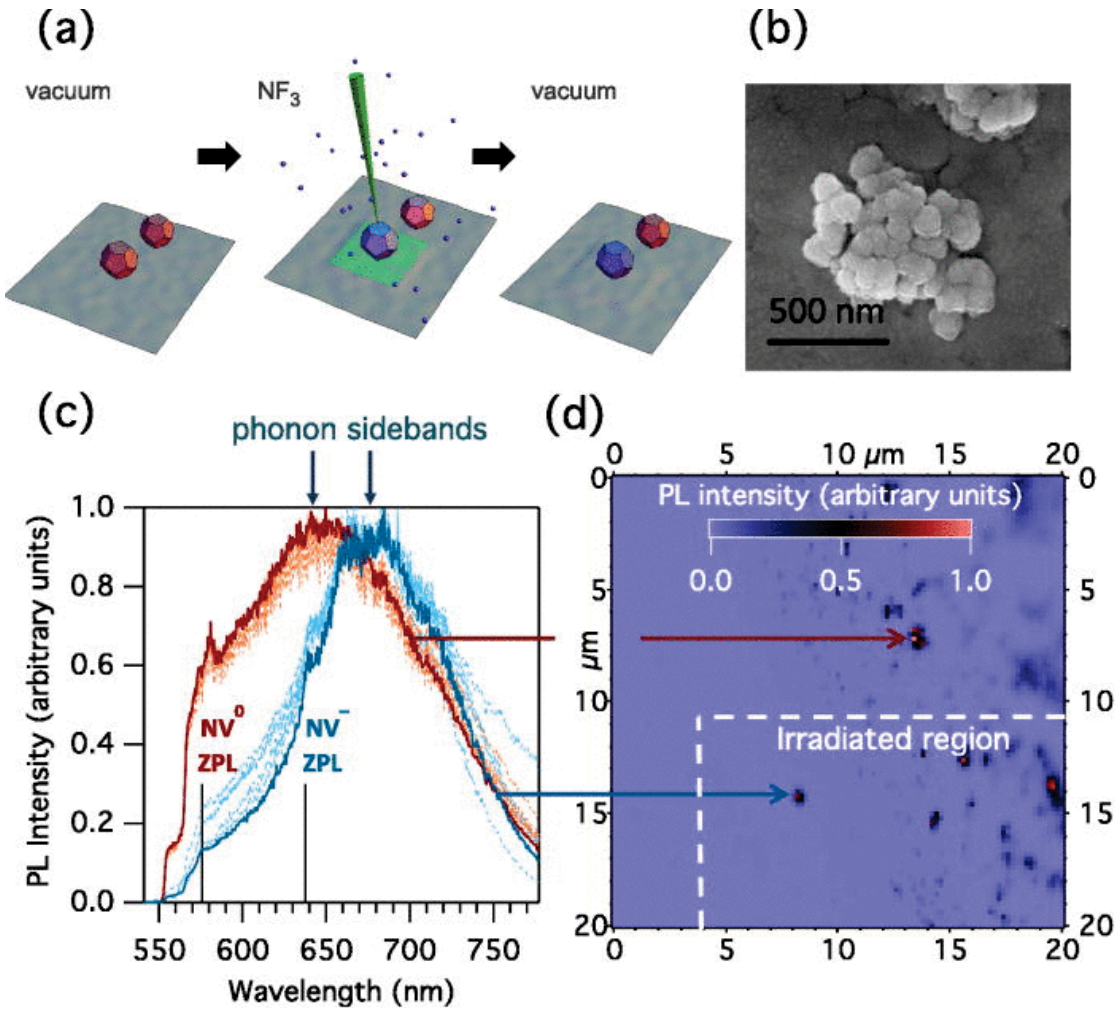

FIGURE 6.8: (a) Schematic illustration of nanodiamonds before, during and after electron beam irradiation in NF_3 vapour. (b) SEM image of a cluster of nanodiamonds. (c) PL spectra collected from virgin, H-terminated, and irradiated nanodiamonds (solid lines). (d) PL map showing the sample region that was irradiated by an electron beam. The dashed traces in (c) show 5 additional spectra acquired from the virgin and irradiated sample regions, illustrating the consistency of data collected from H-terminated and irradiated nanodiamonds.

intensity ratio is inverted. This difference correlates perfectly with clear shifts in the EPYS spectra observed from the polycrystalline diamond film, with the NV^0 emission corresponding to the low photoelectron emission threshold, and NV^- corresponding to the high photoelectron emission threshold.

The fluorinated surface is stable upon exposure to air at room temperature. However, the photoelectron emission threshold returns to 4.55 eV after heating to 100°C under vacuum, cooling to room temperature, and exposure to H_2. This behavior corresponds to thermal desorption of fluorine, which has been shown to occur over a wide temperature range, starting as low as 40°C [93].

6.5 Discussion

The changes in EPYS spectra and PL from polycrystalline diamond and nanodiamonds respectively are understood in the context of surface band bending induced by the presence of either hydrogen and H_2O, or fluorine. Strong evidence for a spontaneous exchange reaction between hydrogen and gaseous fluorine is presented; however, a H_2O overlayer typically present on the diamond surface prevents the exchange reaction from taking place - as evidenced by EPYS and PL measurements of diamond exposed to NF_3 without having undergone a thermal conditioning step that serves to remove the H_2O.

The ionisation energy (ξ) observed with EPYS of 4.55 eV is consistent with the negative electron affinity of H-terminated diamond [76, 254]. The increase to 5.84 eV is also consistent with surface fluorination due to the large electronegativity of fluorine, which inverts the polarity of the surface dipole, causing a downward bending of the bands in diamond, as shown in Figure 6.9 [253, 267]. The extent of downward band bending due to chemisorbed fluorine is smaller than that reported for F-terminated (100) diamond, shown to be upwards of 8 eV [267]. The difference is attributed to incomplete fluorination, and the possibility that some surface sites are terminated by NF_x species.

The charge state of NV centres is determined by the position of the $NV^{0/-}$ charge transition level (shown in Figure 6.9) relative to the Fermi level [225]. Near the surface, the transition level is located above and below the Fermi level in the case of hydrogen-terminated and fluorinated diamond, respectively. Therefore a downward shift of the

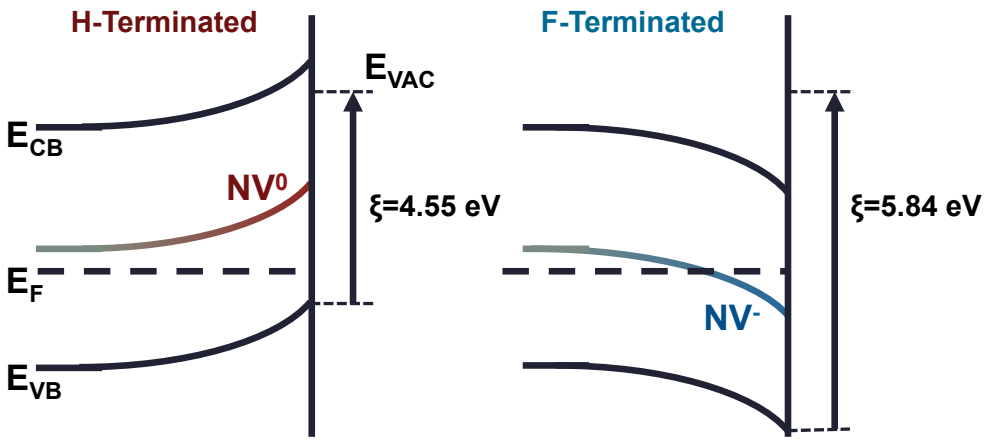

FIGURE 6.9: Simplified schematic of a diamond surface terminated with hydrogen and fluorine. [E_{CB} = conduction band minimum, E_{VB} = valence band maximum, E_F = Fermi level, E_{VAC} = vacuum level, ξ = ionisation energy]

valence band maximum relative to the Fermi level is expected to cause a corresponding switching of the charge state of near-surface NV^0 centres, as was observed by ex-situ PL of the thermally treated diamond film.

Electron irradiation of the diamond surface in the presence of NF_3 was shown to increase the ionisation potential of H-terminated diamonds with EPYS. Perhaps the most compelling evidence for a protective H_2O overlayer preventing spontaneous fluorination was a locally induced chemical switching of NV charge states on the nanodiamond sample by irradiation with an electron beam in the presence of NF_3 (illustration of this process is shown in Figure 6.10). The localised, electron beam induced version of the process was attributed to electron beam stimulated desorption of H_2O molecules and fragments from H-terminated diamond, and subsequent exchange of hydrogen with fluorine. The fluorination step takes place spontaneously at room temperature (as shown by EPYS), but was likely assisted by electron-beam-induced decomposition [268] of NF_3 adsorbates.

Prior methods for fluorinating diamond have included exposure to elemental and molecular fluorine [262], XeF_2 [93, 259, 267], CF_4 plasma [264], and CHF_3 plasma [269]. However, all of these methods are delocalised, and most are prone to the generation of

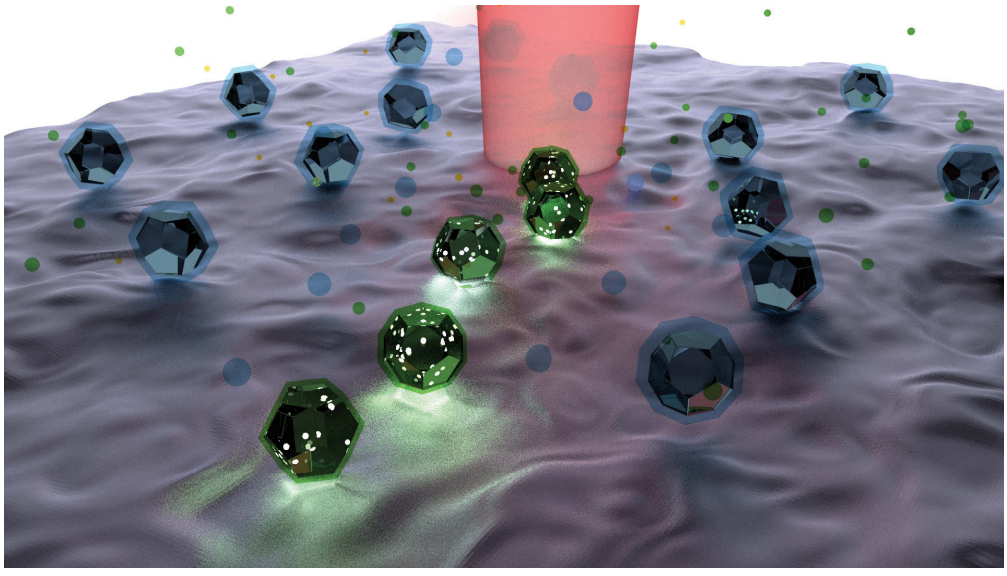

FIGURE 6.10: Illustration of the activation of near-surface NV^- defects in nanodiamonds by irradiation with an electron beam in the presence of NF_3. Electron bombardment removes a protective water overlayer, and exposed bare hydrogen terminated diamond to NF_3, which then undergoes a spontaneous exchange reaction, fluorinating the nanodiamonds.

defects that compromise the optoelectronic properties of diamond. The room temperature, NF_3-mediated, electron beam technique described here is minimally invasive and enables highly localised, direct-write processing of diamond.

6.6 Conclusion

The charge state of near-surface NV centres has been controlled by changing the electronegativity of molecules that terminate the diamond surface [225, 263, 265]. A mechanism for achieving this was identified using EPYS and corroborated with PL. A method for controlling the NV charge states was developed here and can be achieved in a single step, with high spatial resolution by irradiating H-terminated diamond with an electron beam in the presence of NF_3 vapour. It was shown that, in the absence of electron irradiation, NF_3 does not alter H-terminated diamond provided it contains a protective overlayer of H_2O molecules/fragments. Conversely, if the overlayer is desorbed (either thermally or through electron stimulated desorption), exposure to NF_3 at room temperature yields: (i) a stable change in photoluminescence caused by an increase in the ratio of negative to neutral NV centres; and, (ii) an increase in the ionisation energy of diamond. The electron beam fluorination process is highly localised and could be used to switch the emission spectrum of individual nanodiamonds and surface regions scanned by the electron beam. The observed behaviour is consistent with the effects of fluorine on band bending at the diamond surface, which are verified by measuring changes in the ionisation energy of diamond using EPYS.

6.7 Implications

This study has profound implications in the development of diamond-based quantum computing and development of magnetic measurement instruments. The highly desirable electron spin and optical properties of NV^- make it a promising candidate as a single photon emitter in quantum information processors, but also requires that the defect be active very close to the diamond surface. This limitation is also imposed on high spatial resolution magnetometers, which will be limited in their resolution by the size of the nanodiamonds that host NV^- centres. In both cases, hydrogen termination in atmosphere imposes a lower limit on the size of diamond particles due to the width

of the depletion region caused by electron transfer across the hydrogen interface into the water overlayer. This limitation can be overcome by fluorine surface termination, achieved here, activating NV^- centres at the diamond surface.

The ability to directly write fluorine termination to diamond using an electron beam also has other applications such as the generation of high spatial resolution patterns of differing surface conductivity, wetting behavior and other physical properties associated with the energetic surface structure of diamond.

Chapter 7

Application of EPYS: monitoring adsorbate coverage

7.1 Summary

Environmental photoelectron yield spectroscopy (EPYS) has been used to study the work function of platinum single crystal (110) as a function of temperature in the presence of CO. A significant decrease in the work function of platinum has been observed with increasing temperature. This is proposed to arise from dipoles generated by three different binding states of CO to platinum, which exist at different CO coverages due to adsorbate-adsorbate interactions governing their ability to rearrange binding configurations.

7.2 Introduction

CO chemisorption to platinum surfaces has played a major role in the long-standing model of heterogeneous catalysis, CO oxidation [270–273]. Catalytic CO oxidation is a reaction between CO and oxygen, producing CO_2, that would not otherwise occur unless the reactant species are co-adsorbed on a catalyst (such as Pt) [274, 275]. The general reaction steps proceed in the following way:

$$CO \rightleftharpoons CO_{ads} \tag{7.1}$$

$$O_2 \rightleftharpoons 2\,O_{ads} \tag{7.2}$$

$$CO_{ads} + O_{ads} \longrightarrow CO_2 \tag{7.3}$$

Molecular oxygen dissociatively chemisorbs to platinum, where it may then undergo a reaction with a nearest neighbouring CO molecule [120, 270, 276]. This reaction plays a large role in a variety of existing industrial applications, including the neutralisation of toxic CO exhaust in the automotive industry [274]. It is also of intrinsic scientific interest, due to questions about the physical origin of catalytic reaction pathways. Only in the last couple of decades, with the advent of low vacuum surface characterisation techniques, has this seemingly simple reaction been exposed as highly sensitive to the gaseous environment in which it takes place [23, 277, 278].

7.2.1 CO oxidation reaction

The reaction has often been viewed as ideal for investigations of fundamental catalytic reaction processes, as it involves adsorption/desorption of reactants (CO) [15, 273, 279, 280], dissociative adsorption of reactants (O_2) [281–285] and reactant inhibition (CO poisoning) [22]. The classic, high vacuum reaction pathway has been described as a Langmuir-Hinshelwood mechanism [15, 278, 286], in which the neighbouring adsorbates react with one another producing CO_2. In the idealistic conditions of UHV instrumentation, CO is known to have a high sticking coefficient on Pt, in the order of greater than 1 eV [47, 287, 288], and CO_{ads} had been shown to inhibit O_2 adsorption as a result [289, 290]. Thus at low temperatures in UHV, CO_2 production was inhibited by absorbed CO, with CO_2 production increasing with temperature. However, high temperature reactivity was observed to decrease due to lower CO adsorption and higher desorption rates.

With recent developments in high-pressure surface analysis techniques, a number of more nuanced, and contentious, reports about reactivity of platinum have been made [291–293]. These have included the formation of an oxide that greatly increases CO_2 production rate [277], a highly reactive and transient regime that is CO uninhibited [278],

and less recently - using a photoelectron emission microscope - complex, propagating reaction diffusion waves shown in Figure 7.1 [282, 294]. In each of these cases, the configuration of adsorbed CO determines the platinum superstructure phase transitions (for example $2 \times 1 \rightarrow 1 \times 1$) which in turn affect, in one case, the platinum oxide crystal structure, and in another, the reaction diffusion patterns. Furthermore, the role of the work function in catalysis is of fundamental significance, as an electron transfer to or from the catalyst is a requirement for the catalytic reaction to proceed. An example of how work function modification can dramatically affect the reactivity of a catalyst is non-Faradaic electrochemical modification of catalytic activity (NEMCA) [295].

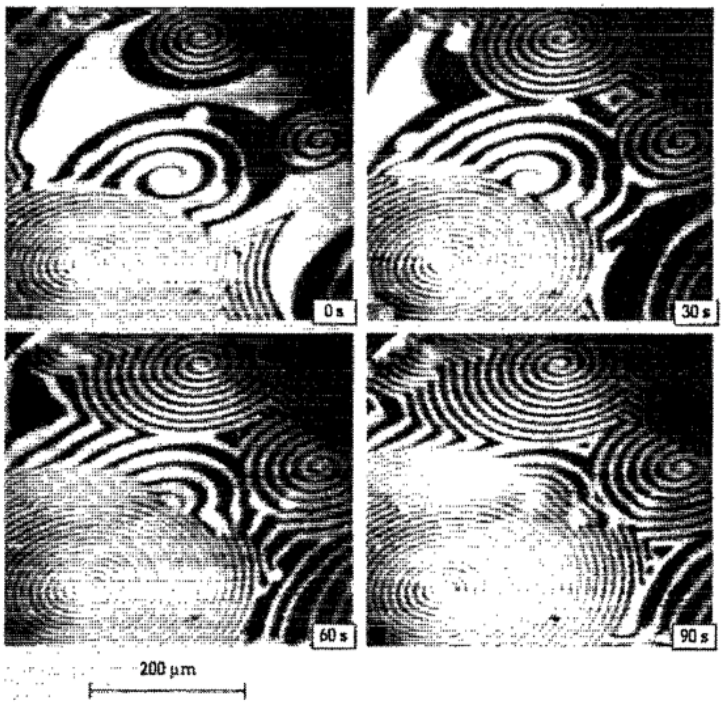

FIGURE 7.1: Temporal evolution of reaction diffusion spiral waves. The fronts of the waves are where a CO oxidation reaction is taking place with adsorbed O^- on Pt. The dark lines are O^- covered and the white spaces are CO covered [294].

7.2.2 CO on platinum

CO spontaneously chemisorbs to platinum surfaces, which is the result of charge transfer from the CO molecule to the surface [296, 297]. The carbon atom binds to one or more platinum atoms, while the positive oxygen atom faces away from the surface; this results in a dipole with its positive pole pointing outwards from the surface [273, 296, 298]. CO's binding energies to platinum have been studied extensively in the past,[15, 48, 270, 282] and three binding states of CO have been identified on platinum (110) using thermal

desorption spectroscopy (TDS) [282, 299–302]: a relatively strongly bound state (A) at low coverages with a binding energy of 1.462 eV; an intermediately bound state (B) with binding energy 1.204 eV and a weakly bound state (C) present at high coverages with a binding energy of 0.946 eV. Although some groups have reported slightly different desorption temperatures for the different states [47, 303, 304], they are generally in agreement. The desorption temperatures are not a function of coverage, and therefore are not affected by ambient pressure. They represent the average thermal energy imparted to adsorbates from the sample, beyond which, desorption rates increase exponentially. The rapid desorption beyond certain thermal energies occurs as the thermal energy exceeds the chemisorption activation energy E_A. A schematic of potential wells for each of these chemisorption states is shown in Figure 7.2.

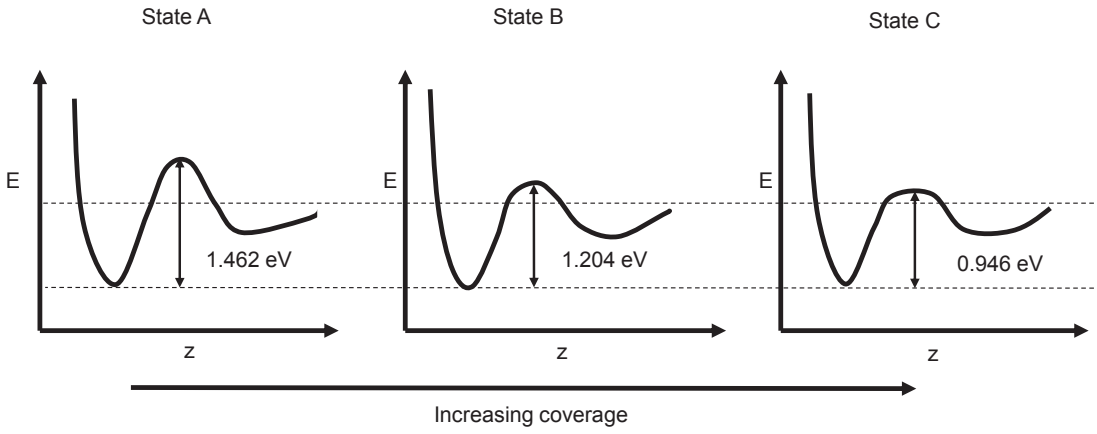

FIGURE 7.2: Potential energy diagrams of the three chemisorbed states of CO on platinum. The binding strength decreases with increasing coverage due to adsorbate-adsorbate interactions. When there is less CO present, the adsorbate molecule binds more strongly with the Pt atoms (hybridised C-Pt bonds) and when there is more CO, the nature of the C-Pt bonding changes, resulting in a more weakly bound state.

Each of these distinct binding states are the result of different bonding arrangements between the platinum surface atoms and the CO molecules [252]. It is expected that increasing coverage leads to lower bonding energies due to the ability of a CO molecule to interact with more than one platinum atom at low coverages, while at high coverages, there are a greater number of CO molecules per platinum atom, and weakly bound CO molecules may even be situated atop or between more strongly bound states [296]. An example of how the coverage of CO on platinum is expected to affect its bonding configuration is shown in Figure 7.3.

A high pressure study of CO adsorption on Pt was also performed by Rupprecheter et al. [305] using SFG vibrational spectroscopy. Their findings indicated that CO was the

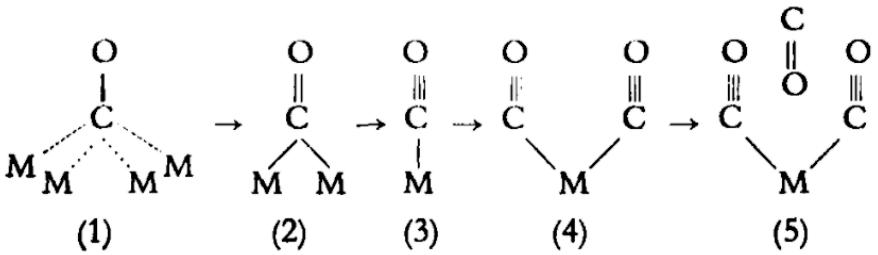

FIGURE 7.3: Speculative schematic of how coverage of CO molecules on platinum atoms affects the CO-platinum bonding configuration (taken from Culver [296]). (1) represents the most strongly bound state in the lowest coverage regime, while (5) shows a weakly bound state situated between chemisorbed CO molecules.

only species present on the Pt surface between 160 and 400 K, independent of gaseous CO pressure up to 500 mBar. They observed co-adsorbed H_2O below 160 K, which red-shifted the terminal CO peak as a result of electron donation from water to CO. The water was inadvertently introduced through the gas delivery system, but was observed to completely desorb at temperatures exceeding 160 K. The stability of the CO peak under changing pressure indicated that full coverage is achieved with initial exposure to CO.

7.3 Experimental methods

A circular Pt (110) single crystal 5 mm in diameter was used for this study. Prior to loading to the EPYS chamber, the sample was cleaned with a sonicator in acetone, isopropanol and then water for 20 minutes each, then baked at 120°C for eight hours. Once loaded into the vacuum chamber, the sample was preconditioned by heating to 150°C at 6×10^{-8} mBar for two hours to remove residual water and hydrocarbons. The spectra acquired during the following experiments were not corrected for system response because the purpose of these experiments was to monitor only the emission threshold, which is most easily identified in the raw data

The chamber pressure was raised to 2 mBar with CO gas, through a gas delivery needle positioned to maximize gas flux over the sample surface. Stable dynamic pressure was achieved by setting the in-flow rate to 1 sccm with a mass flow controller, and opening a manual needle valve to a scroll pump until the desired pressure was reached. Photo-electron yield spectra were then gathered at room temperature at rate of 1 spectrum per 3 minutes for approximately 1 hour with a detector bias of +440 V. The sample

temperature was then raised incrementally over the period of six hours, from approximately 47°C to 380°C, while EPYS spectra were continuously collected. The pressure and detector bias were kept constant during the course of the experiment.

The temperature was controlled by a current supply to a heating element beneath the sample stage, and the temperature was measured with a Pt resistance thermometer embedded into the sample stage. Approximately every 30 minutes the temperature was increased and allowed to settle for 20 minutes, at which point the temperature was measured and recorded. After reaching 380°C, the temperature was decreased back to 300°C in order to verify the reversibility of the photoelectron emission thresholds.

A secondary experiment was performed to examine the photoelectron emission reversibility over the full temperature range. In identical conditions to those described above, photoelectron emission spectra collection began at 380°C, and the sample stage was then allowed to cool to room temperature. However, the temperature was not measured during the course of this experiment due to the electrical noise induced by closing the circuit on the Pt resistance thermometer in the EPYS sample stage.

A supplementary experiment was performed to verify that the photoelectron emission observed was not arising from an unidentified source, or that it was not spurious emission from the stage. A residual gas analyser was incorporated onto the EPYS chamber to monitor the presence of CO, CO_2 and O_2 in order to be able to correlate changes in the photoelectron emission spectra with changes in the Pt surface coverage, which could be inferred from the partial pressures of CO and O_2 and the production rate of CO_2. A series of measurements were performed resembling the experiments described above. Firstly, spectra were collected at room temperature from Pt in a high vacuum environment ($\sim 3 \times 10^{-6}$ mBar); then CO was introduced to the chamber at a pressure of 2.6 mBar at room temperature; the sample was then heated to 380°C while spectra were being collected; and finally, a small amount of gaseous O_2 was injected into the chamber, such that the absolute pressure was not significantly affected by the addition of O_2.

Additional experiments were performed to confirm the effects of oxygen on the work function of Pt. Firstly, oxygen-terminated Pt was achieved by exposing the Pt surface

to oxygen plasma prior to acquiring EPYS spectra without breaking vacuum. Secondly, EPYS spectra were continuously acquired while heating Pt in an O_2 environment. In both cases, the photoelectron emission threshold was found to increase beyond reported values of clean Pt surfaces - 5.65 to 6.1 eV [306, 307] - as is expected of oxygen-terminated/oxidised Pt [308]. The photoelectron current during these experiment was extremely weak: in the case of oxygen plasma treated Pt, the photoemission threshold was barely observed at incident photon energies >6 eV; and the photoemission threshold while heating in an O_2 environment was observed to increase with a corresponding decrease in photoelectron current until photoemission as barely discernible beyond 6 eV.

7.4 Results

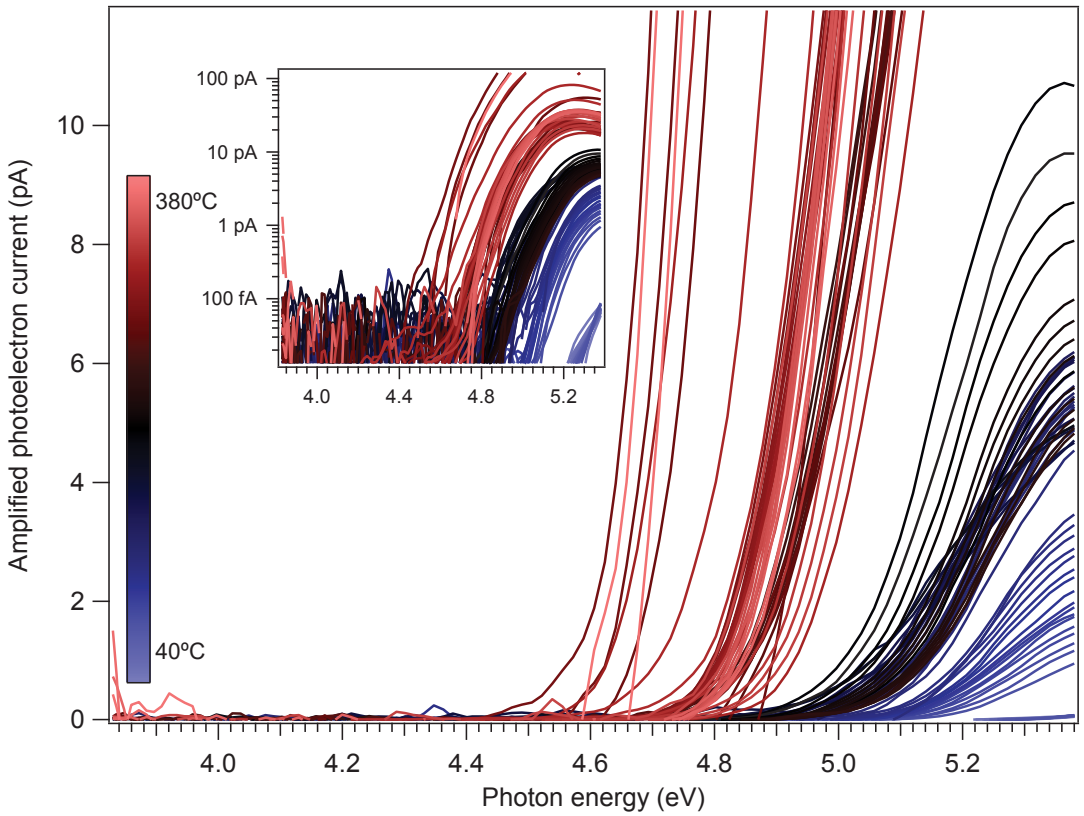

FIGURE 7.4: Temperature-resolved EPYS spectra acquired while Pt was heated in a CO environment. The blue traces were collected at ~47°C the temperature was incrementally increased and recorded for each set of spectra until reaching ~380°C, shown in red. After collecting spectra at 380°C, the temperature was decreased to 307°C to check for reversibility. The inset is a log-linear plot of the same data that highlights the shifting photoelectron emission threshold.

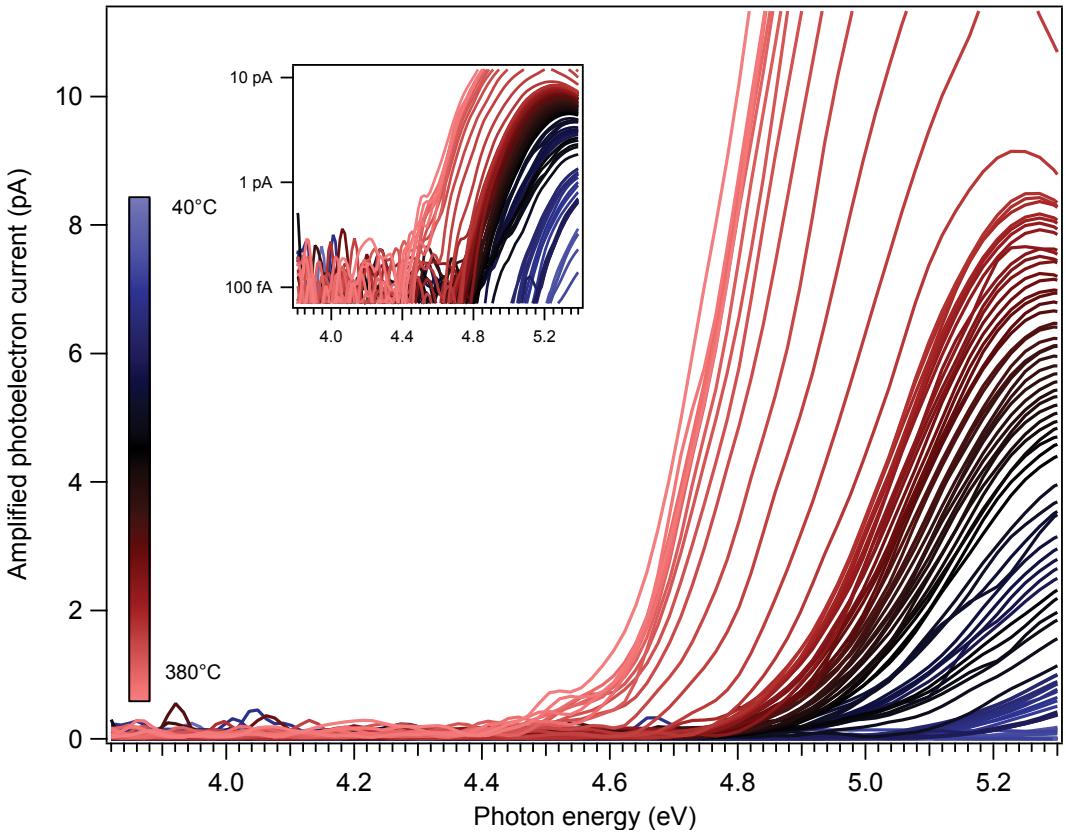

FIGURE 7.5: Temperature-resolved EPYS spectra acquired while Pt was cooled in a CO environment. The light red traces were collected at ~380°C, the temperature was allowed to decrease until reaching room temperature, shown in blue. The temperature was measured only at the start and end of this experiment due to the influence of measuring temperature on the EPYS signal integrity. The inset is a log-linear plot of the same data that highlights the decreasing photoelectron emission threshold.

Temperature resolved EPYS spectra from heating Pt (110) in CO are shown in Figure 7.4, and corresponding EPYS spectra from cooling Pt(110) in CO are shown in Figure 7.5. The insets in both show the spectra on log-linear scale. The photoelectron emission threshold of CO covered Pt at approximately 47°C was observed to be 5.2 eV, which corresponds with reported work functions [15, 273, 293]. Upon heating the sample, the work function decreased rapidly to approximately 4.8 eV at 100°C. The work function subsequently appeared to increase relatively slowly until approximately 300 °C, at which point it began to drop rapidly again, eventually to 4.5 eV at 380°C. As the temperature was lowered after reaching 380°C, the photoelectron emission threshold increased by an amount corresponding with its original decrease. During the second experiment cooling Pt in gaseous CO, the observed decrease of the work function with temperature was also found to be reversible over the whole temperature range, as shown in Figure 7.5.

Another feature of the EPYS spectra is a significant, reversible increase in the photoelectron emission current with increasing temperature. There are two possible reasons for this that are discussed below.

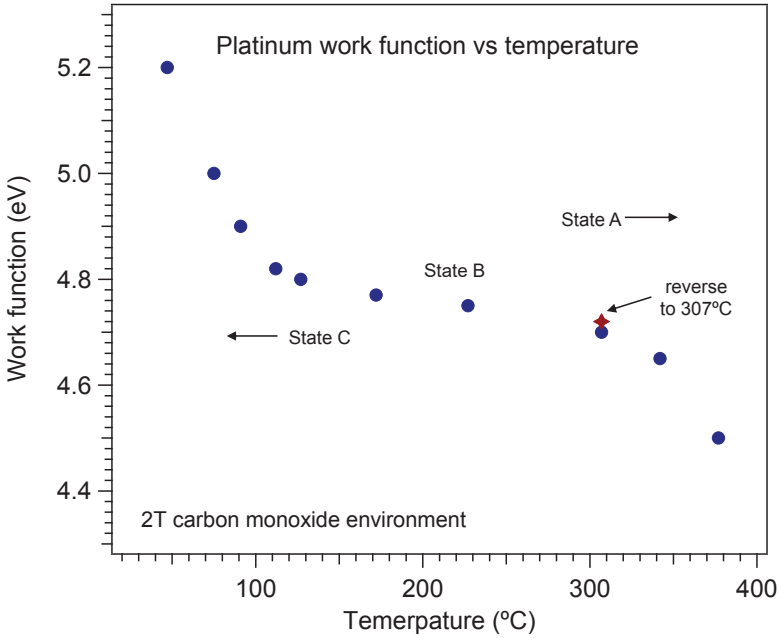

FIGURE 7.6: Work function determined from the average of photoelectron emission thresholds collected as a function of sample temperature. The existence of different binding states can explain the nonlinear relationship between the observed work functions and temperature.

During the first (heating) experiment, the temperature was increased from 47°C up to 380°C in 10 increments. The increments were not equally spaced due to the poor accuracy of calibrating the current source with the heating element over the range of possible pressures that the EPYS operates at. The temperatures to which the sample stage equilibrated after 20 minutes at a constant heater current were as follows: 47°C; 75°; 91°C; 112°C; 127°C; 172°C; 227°C, 307°C; 342°C and; 377°C. After reaching the maximum 377°C, the sample temperature was returned to 307°C.

At each temperature during the first Pt heating experiment, the five final spectra collected were averaged and used to determine the work function, which is plotted versus temperature in Figure 7.6.

The spectra shown in Figure 7.5 (cooling Pt from 380°C in CO) demonstrate the complete reversibility of the work function shift over the entire temperature range studied. Although the intermediate temperatures were not measured during cooling the spectra clearly demonstrate a return to initial room temperature photoelectron emission from

Pt in CO. The absence of sample temperature measurements (to preserve the EPYS signal quality) also means that each spectra are approximately equally spaced in time and correspond to an exponential decrease in temperature. A significant bunching of the photoelectron emission threshold about 4.8 eV suggests that between 47°C and 380°C, the Pt work function was largely between the values of 4.7 and 4.9 eV.

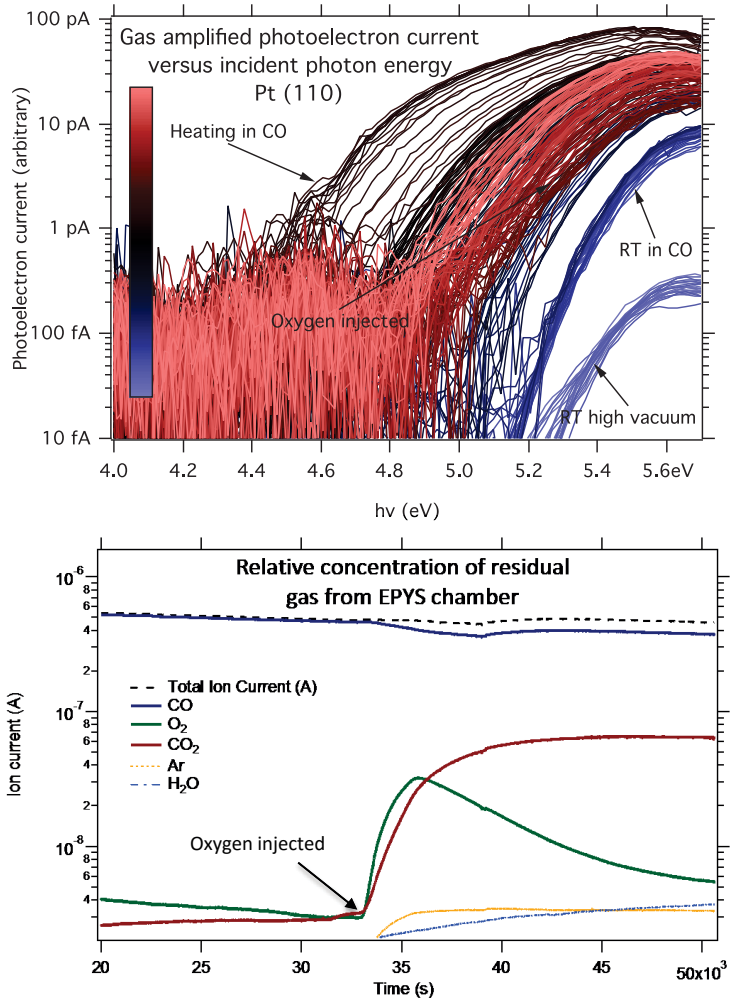

FIGURE 7.7: (Top) A repeat experiment monitoring the photoelectron emission from CO-covered Pt with increasing temperature in which O_2 was injected at ∼370°C. Upon O_2 injection, the work function immediately decreased, and then returned to its former CO covered state. (Bottom) The corresponding residual gas analysis of this experiment. The work function slowly returns to its high temperature CO-covered state as O_2 is depleted via the CO oxidation reaction.

Figure 7.7 (Top) shows the effect of injecting O_2 into the EPYS chamber when the CO-covered Pt surface is heated to ∼380°C. The work function of Pt immediately increased to approximately 5 eV upon the introduction of O_2. The work function then steadily begins to return to its CO value of ∼4.8 eV. Figure 7.7 (Bottom) shows the residual gas

analysis of this experiment, confirming the oxidation of CO by O_2 via Reactions 7.1 - 7.3 as the residual CO_2 partial pressure follows the O_2 partial pressure very closely and both approach steady state values as time approaches infinity. It is important to remember that CO is injected into and pumped from the chamber continuously during the course of the experiment. Hence, upon injection of O_2, the CO partial pressure decreases as the CO_2 partial pressure increases, due to CO consumption in the oxidation Reaction 7.3. It is assumed that traces of Ar and H_2O traces identified by residual gas analysis upon O_2 injection are residual gas species present in the shared gas delivery lines.

7.5 Discussion

To our knowledge, this is the first experiment in which the absolute work function was measured during a Pt heating cycle. A Pt work function of 4.5 eV, observed at high temperatures, in a CO environment (Figure 7.4), is significantly lower than any values reported in the literature [15, 273, 293]. To confirm that this observation was not an artefact, EPYS spectra were also acquired from oxidised Pt by both heating in an O_2 environment, and also after exposing to oxygen plasma. In both cases the work function was observed to increase to vales >6 eV, which is consistent with literature.

The increase in photoelectron emission current that accompanies the observed decrease in work function may be associated with an increase in the density of states close to the Fermi level at the Pt surface, which is an effect that has been both calculated and observed previously for CO-covered Pt [293, 309]. It may also arise due to the fact that the photoelectron yield represents the sum of all filled states hv below the vacuum level. If the work function is lowered by $\triangle\phi$, bringing the density of states closer to the vacuum level, then for a given hv, the total number of photoelectrons increases proportionally to the total number of filled states $\triangle\phi$ below its former level. Both of these effects are likely to be contributing to the significant increase observed in the photoelectron emission current.

The work function changes observed here are discussed in the context of different CO binding states resulting in dipole fields of different strengths. However, additional experiments probing the effects of CO coverage should be performed to verify this effect. Reactions and interactions of CO with residual gas molecules such as H_2O - especially

under irradiation by UV light - could give rise to the formation of unique surface terminations and molecular overlayers that may lead to the work functions shifts observed in this study. Similar effects have been observed with water overlayers preventing an otherwise spontaneous fluorination of hydrogen-terminated diamond [113], such that heating in a gaseous fluorine environment causes the photoelectron emission threshold of diamond to increase because the residual water overlayer is desorbed, allowing fluorination to occur.

Given the CO flow rate remained unchanged, the arrival rate of CO molecules onto the Pt surface would not have changed; however, the sticking probability and desorption rate will have decreased and increased, respectively, as the sample was heated. It is therefore inferred that the coverage of CO on the Pt sample decreases with the increasing temperature, despite the low vacuum environment. Additionally, the coverage is expected to reach steady state rapidly (relative to the time taken to acquire an EPYS spectrum) whenever the temperature is altered due to the high pressure and hence arrival rate of CO molecules at the Pt surface.

The relation between work function and temperature is not linear, but rather appears to change rapidly upon reaching certain activation temperatures. This behaviour further indicates that the work function shift is associated with coverage, and the temperature ranges of stable work function correspond to the temperature differences between desorption energies associated with different adsorption states. Reported desorption temperatures for binding states (C), (B), and (A) of CO on Pt (see Figure 7.2) are 200°C 330°C and 490°C respectively. In the range between 200°and 330°C, the (B) state is dominant, and coverage is not expected to change significantly until either the (B) state is depopulated beyond 330°C, or when the (C) state coverage begin to increase below 200°C. A distribution of binding states taken from Nishiyama [299] is shown in Figure 7.8.

The temperature range investigated in this study does not probe the desorption temperature of the most strongly bound state, (A). However, it does cover a range of temperatures over which adsorbates residing in states (B) and (C) are expected to desorb rapidly. Correspondingly, we observed two temperature ranges over which the work function dropped significantly, these being from approximately 50 - 100°C, and 300 - 380°C. The latter is approximately the temperature at which the dominant binding state

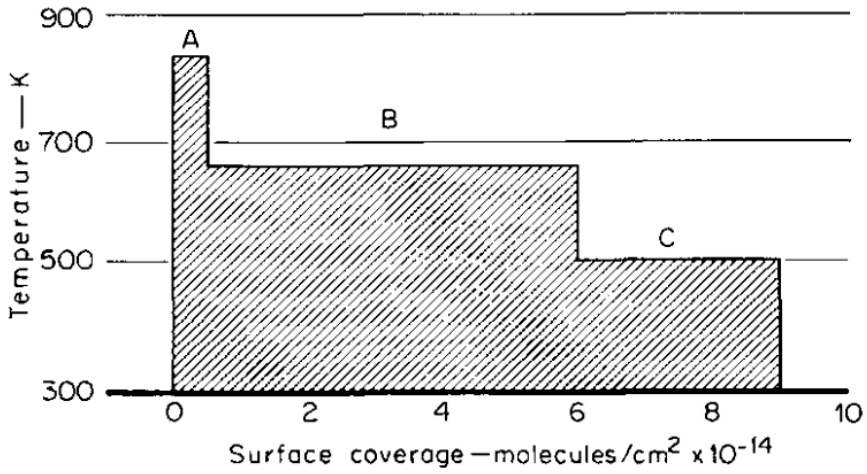

FIGURE 7.8: Distribution of binding states of CO on Pt taken from Nishiyama [299].

(B) is expected to depopulate, leaving the most strongly bound CO configuration at low coverages. The lower temperature over which the work function was observed to decrease does not correspond to the reported desorption temperature of state (C), 200°C, which may be due to the weakly bound states being more susceptible to desorption over a much wider temperature range - as shown in Figure 7.9 taken from Nishiyama [299].

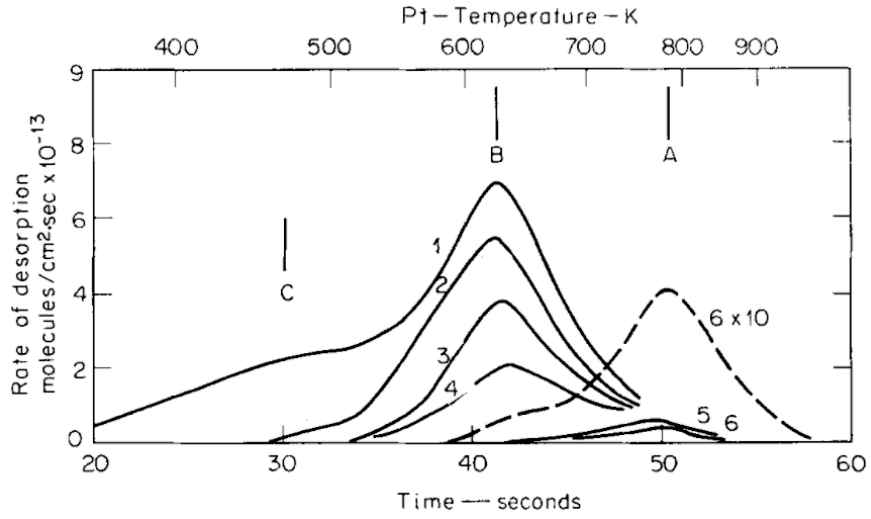

FIGURE 7.9: Desorption kinetics of CO chemisorbed on Pt taken from Nishiyama [299].

An important question about how the binding configuration of CO changes with coverage is whether the states coexist, or whether the way a CO molecule is bound to the surface evolves as the number of nearest neighbours changes. The fact that variations in the binding states are largely influenced by interactions with neighbouring adsorbates points to an evolution of binding configuration with coverage. This interpretation also intuitively makes sense in terms of the shift in work function. The presence of all

states simultaneously would lead to contributions to the photoelectron emission from each state, albeit a contribution weighted by their relative populations. One would thus expect some small but detectable photoelectron emission at ∼4.5 eV, no matter what the coverage. However, this is not observed.

The coordination configuration of the CO molecule on top of the Pt surface determines how the electron density between the surface and the CO molecule is distributed [296]. The very presence of a CO molecule results in a redistribution of the native Pt electron density; and this electron density difference is the cause of the surface dipole associated with CO molecules on Pt. The surface dipole superimposed over the native surface energetic barrier, or work function, causes the barrier height to change; in this case, the barrier decreases, lowering the work function of the bare Pt surface. As the coordination, or geometry of the chemisorbed CO molecule reorganises into its lowest energetic state, according to its interactions with co-adsorbed CO molecules, the electron density difference increases or decreases in polarity, thus affecting the work function.

It is proposed in this work that the increasing binding strength of CO to Pt, that occurs with decreasing coverages, is the result of hybridisation with a greater number of Pt atoms per CO molecule, the outcome of which is an increase in strength of the CO-Pt bond polarity. The natural dipole field generated by CO on Pt lowers the work function. It is, therefore, natural to assume that increasing the polarity continues to lower the surface energetic barrier.

Although the dipole field strength may vary in proportion to the coverage due to adsorbate-adsorbate interactions, the coverage itself is not directly proportional to temperature as a result of the discrete binding configurations of the CO molecules. A consequence of these relationships is a work function of CO covered Pt that decreases rapidly over certain temperatures due to an enhanced desorption rate of CO molecules in a particular configuration, and a relatively stable work function across temperate ranges between these thermal activation energies. It is the very process of thermally induced CO desorption that allows remaining CO to bind to the surface with a discretely higher bonding strength, and thus decreasing the work function.

7.6 Conclusion

This study used temperature-resolved EPYS to identify a non-linear decrease in the work function of CO-covered Pt (110) with temperature. Work functions as low as 4.5 eV were observed, which have not previously been reported. A model invoking the relationship between dipole fields, adsorbate bonding configurations and adsorbate-adsorbate interactions was proposed to account for the observations made with EPYS. Specifically, three reported binding states of CO on Pt, associated with interactions between co-adsorbed molecules, were used to understand how CO coverage varies non-linearly with temperature, and how the evolution of the binding states with coverage causes a change in the surface dipole field, and hence work function of Pt.

7.7 Implications

This study is one of few examining the nuances of a fundamental process in a catalytic reaction that has previously been considered to be adequately explained by Langmuir-Hinchellwood kinetics, when studied with UHV techniques. The study highlights the need for low vacuum, real-time surface analysis techniques to elucidate surface processes that take place in semi-realistic conditions, and may otherwise go unnoticed. Furthermore, it has identified that an important surface property of CO-covered Pt: the work function decreases to a significantly low value previously not observed. This is a particularly important factor to be considered when attempting to understand the kinetics of catalytic reactions taking place on Pt surfaces.

Chapter 8

Conclusion

The environmental photoelectron yield spectroscopy (EPYS) instrument, developed entirely as a major part of this project, is a completely unique and novel, low vacuum, surface analysis instrument. Unlike its conventional, ultra high vacuum counterparts that interrogate ideal surfaces in non-realistic conditions, the EPYS enables real-time characterisation of dynamic surface processes in semi-realistic, reactive gaseous environments. This capability is a requirement for the technological progress and fundamental understanding of processes in materials physics, chemistry and bio-sciences. The ability to observe time- and temperature-resolved surface electronic structure changes in response to ambient gas species has been demonstrated as necessary for the identification of a surface functionalisation pathway and an effect of adsorbate-adsorbate interactions on surface dipole fields.

The development of the instrument from the ground-up has been an integral part of this project, from designing and building the light and gas delivery systems, the low vacuum detector to machining and welding the cryogenic sample stage and developing instrument automation and control software. Furthermore, the interpretation of experimental results based on a fundamental understanding of the solid-gas interactions that take place has been a core aspect of the project.

This project presents four experimental applications of the EPYS system: the study of gas cascade properties, elucidating a previously unidentified aspect of gaseous molecules that makes them more or less suitable for use as an amplification medium; the study of subsurface defects, the effects of their presence on surface band structure and observation

of a strong, selective response to the presence of ambient NH_3; identification of a surface functionalisation pathway that led to the development of a method for locally activating charge states of shallow, luminescent defects in diamond; and observing previously unseen changes in the surface work function of Pt, a catalytically active metal, that is ascribed to dependence of dipole fields on interactions between coexisting adsorbates that change with coverage.

Limitations of the EPYS instrument are largely associated with its detection mechanism, a gas cascade. The limitations this imposes on the EPYS capability are due to gas amplification artefacts arising from changes in ambient pressure and gas species over time. Although normalised EPYS spectra can be used to quantitatively compare photoelectron thresholds, gases possessing significantly different amplification characteristics prevent time-resolved studies of transitions between environments composed of them. The sensitivity of amplification to pressure also hinders attempts to perform pressure-resolved experiments that would be of tremendous use in the study of coverage related phenomena.

Further research and development could focus on improvements to the existing EPYS hardware system such as increasing dynamic range and operating temperature range. Furthermore, incorporation of additional hardware such as an electron multiplier system offers a high vacuum characterisation capability.

Appendix A

Townsend gas capacitance model

Models of gas cascade amplification for low energy electrons generally assume that each ionising collision between an electron and a neutral atom or molecule produces a single low energy secondary electron.

$$(g) + e^- \rightarrow (g)^+ + 2e^- \tag{A.1}$$

low energy electrons are accelerated by the electric field generated between the stage and positively biased detector. Once an electron has gained sufficient kinetic energy, ionising collisions can take place with gaseous atoms or molecules. The number of ionisations per unit distance in swarm conditions is the first Townsend coefficient α_{swarm}, and has been given by the relationship [83]

$$\alpha_{swarm} = \beta p e^{-\zeta p/E} \tag{A.2}$$

where p is the gas pressure, E is the electric field strength (V/d_{gap} where V is the detector voltage and d_{gap} is the sample-detector distance) and

$$\beta = \frac{1}{\lambda}, \quad \zeta = \frac{\iota}{\lambda} \tag{A.3}$$

In the above equations λ is the mean free path of electrons between inelastic collisions with molecules, and ι is the ionisation energy of the gas molecule. It intuitively follows

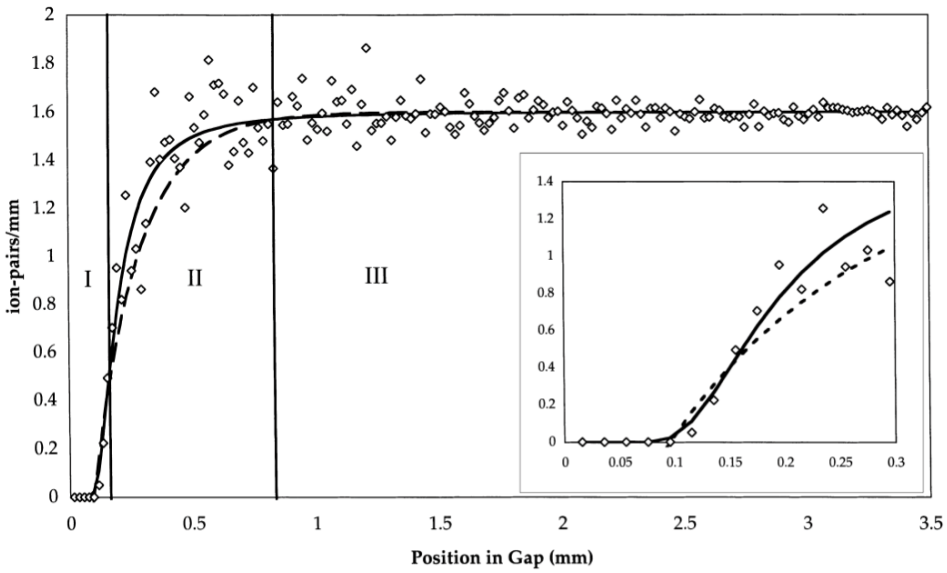

FIGURE A.1: Simulated $\alpha(z)$ curve [86] for typical gas cascade detector operating conditions (d_{gap} =8.5 mm, p =5 Torr and V =500 Volts). Regions I to III represent different ionisation efficiencies as electrons move through the gap. Region 1: no ionisation by low energy electrons near the sample surface; Region II represents increasing ionisation efficiency as electrons are accelerated under the electric field; Region II: swarm conditions and constant ionisation efficiency where energy gained under the influence of an the electric field is equal to the energy loss from inelastic scattering collisions.

from this model that gases exhibiting high values of α will have low ionisation energies, ι. This property of gases is often used as an indication of how efficient the gas will be in cascade amplification detection systems.

α_{swarm} has been shown to vary across the gap [86] due to evolution of the electron energy distribution, and is more appropriately defined as a function of the path, z, between sample and detector by

$$\alpha(z) = \alpha_{swarm}[1 - e^{-Cp(z-z_0)}] \tag{A.4}$$

where C is a specific gas constant, α_{swarm} is the first Townsend coefficient given in equation A.2 and z_0 is the average distance through which photoelectrons must be accelerated from the sample in order to exceed the ionisation potential of the gas ι

$$z_0 = \frac{(\iota - \varepsilon)d}{eV} \tag{A.5}$$

Above, ε is the median of the initial photoelectron energy distribution and e is the charge of an electron.

In Figure A.1 $\alpha(z)$ is zero until $z = z_0$ at which point electrons accelerated by the detector field have exceeded ι and begin ionising gaseous atoms or molecules (region I). In region II $\alpha(z)$ increases as an exponential function approaching α_{swarm}, which is attained in region III. The exponential rise is a direct result of an increase in the ionisation cross sections with electron energy, and swarm conditions are reached due to the increasing efficiency and hence rate of the total inelastic scattering events approaching the rate that energy is gained by electrons under the influence of the electric field.

Following the treatment in [122] the cascade amplification arising from these ionisation efficiencies (under swarm conditions), consider that each ion produces an average of α ion-pairs per unit length, dz, of distance traveled. Thus the number of electrons generated at any point along the path (dN^-) is proportional to the number of preexisting electrons ($N^-(z)$) such that

$$dN^- = N^-(z)\alpha dz \tag{A.6}$$

Integrating across the path length (d_{gap}) from the sample surface ($N^-(0)$) to the detector gives the total number of electrons collected and hence the amplification:

$$\mathcal{A} = \frac{N^-(d_{gap})}{N^-(0)} = e^{\alpha d_{gap}} \tag{A.7}$$

The corresponding number of ions generated is therefore

$$N^+(d_{gap}) = N^-(0)e^{\alpha d_{gap}} - N^-(0) \tag{A.8}$$

$$= N^-(0)[e^{\alpha d_{gap}} - 1] \tag{A.9}$$

Likewise the positive ion current (I_{PI}) can be expressed as the product of the amplification and the initial photoelectron current (I_{PE}).

$$I_{PI} = I_{PE}[e^{\alpha d_{gap}} - 1] \tag{A.10}$$

Positive ions are directed towards the sample under the influence of the detector field. When a positive ion comes into contact with a surface there is a probability that a secondary electron will be ejected as a result of their interaction, γ. When this occurs the secondary electron initiates a feedback cascade that produces more positive ions that return to the sample. If γ is less than the reciprocal of $e^{\alpha d_{gap}}$ (convergence criterion)

$$\gamma(e^{\alpha d_{gap}}) < 1 \tag{A.11}$$

the cascade will stabilize with an additional self-amplification factor (k) which is the sum of successive amplifications from a single positive impact with the surface. k is formalized by summing the number of electrons ejected from the sample after the first cascade ($^1N_c^-$) and all subsequent cascades ($^nN_c^-$) where $n = 2, 3, 4...\infty$

$$^1N_c^- = \gamma\ N^-(0)[(e^{\alpha d_{gap}}) - 1] \tag{A.12}$$

and

$$^2N_c^- = \gamma^2\ N^-(0)[(e^{\alpha d_{gap}}) - 1]^2 \tag{A.13}$$

$$^3N_c^- = \gamma^3\ N^-(0)[(e^{\alpha d_{gap}}) - 1]^3 \tag{A.14}$$

such that k in an infinite sum

$$^\infty N_c^- = N^-(0)\left\{1 + \gamma\ [(e^{\alpha d_{gap}}) - 1] + \gamma^2\ [(e^{\alpha d_{gap}}) - 1]^2 + \gamma^3\ [(e^{\alpha d_{gap}}) - 1]^3...\right\} \tag{A.15}$$

that can be summarily expressed in the form

$$^\infty N_c^- = N^-(0)\sum_{n=0}^{\infty}\gamma^n\ ((e^{\alpha d_{gap}}) - 1)^n \tag{A.16}$$

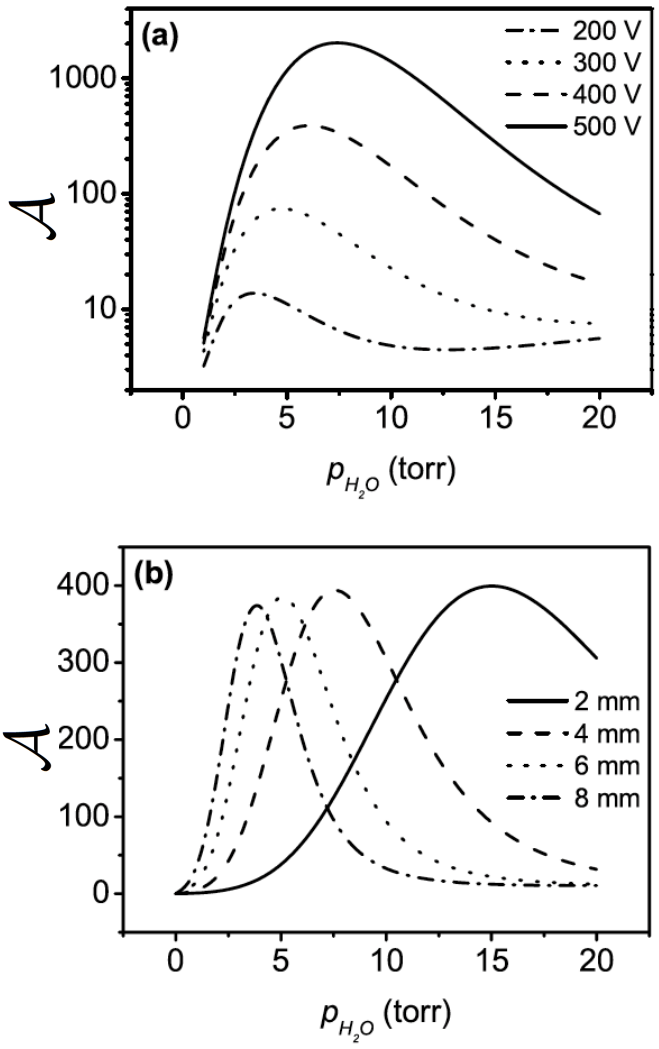

FIGURE A.2: Gas cascade amplification $\mathcal{A}$ versus H_2O pressure as a function of (a) detector voltage at $d_{gap} = 5$ mm and (b) sample-detector separation distance. Figure adapted from [310]

giving the cascade generated self-amplification

$$k = \frac{^{\infty}N_c^-}{N^-(0)} = \sum_{n=0}^{\infty} \gamma^n \ ((e^{\alpha d_{gap}}) - 1)^n \tag{A.17}$$

If the convergence criterion (equation A.11) is met equation A.17 becomes

$$k = \frac{1}{1 - \gamma \ (e^{\alpha d_{gap}} - 1)} \tag{A.18}$$

An expression for the total ion current is thus given by

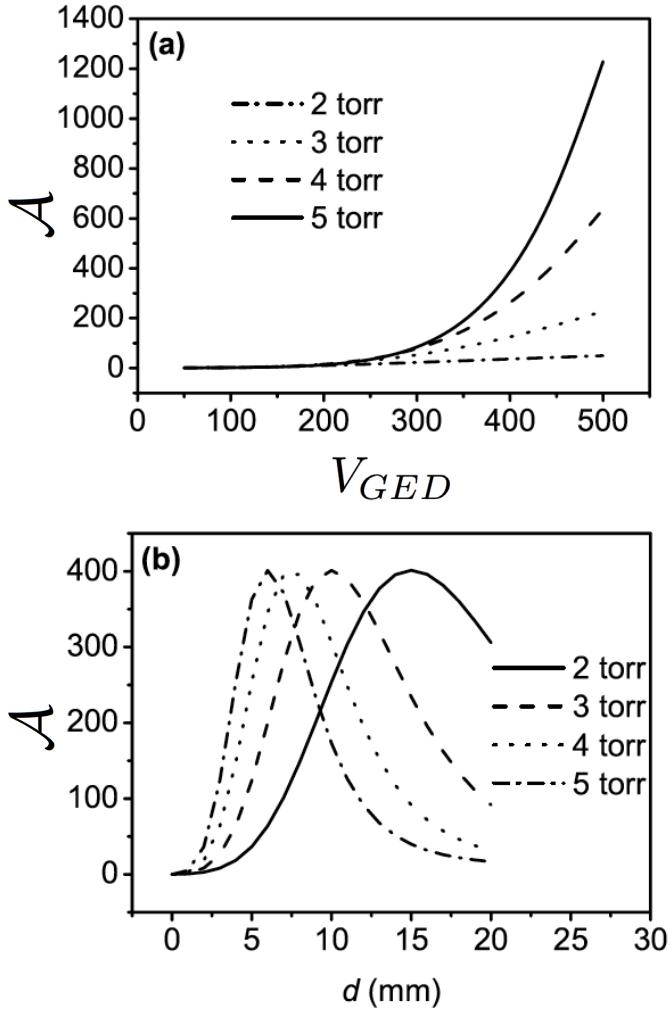

FIGURE A.3: Gas cascade amplification $\mathcal{A}$ versus (a) detector voltage at $d_{gap} = 5$ mm and (b) sample-detector separation distance calculated at four pressures: 2, 3, 4 and 5 Torr of H_2O. Figure adapted from [310].

$$I_{PI} = k\ I_{PE}[e^{\alpha d_{gap}} - 1] = \frac{I_{PE}[e^{\alpha d_{gap}} - 1]}{1 - \gamma\ (e^{\alpha d_{gap}} - 1)} \tag{A.19}$$

The above equation can be used to model amplification, $\mathcal{A}$, of specific gases over a range of detector voltages, pressure and gap distance, as shown in Figures A.2 and A.3, which together determine the rate at which electron energy is gained, the rate at which electron energy is lost and the total number of collisions.

If the efficiency of secondary electron generation by ion impact with the surface is greater than the reciprocal of gas amplification, i.e. the convergence criterion is not met

$$\gamma(e^{\alpha d_{gap}}) > 1 \tag{A.20}$$

a runaway feedback process occurs, resulting in spark breakdown across the gap. γ is a ion-surface specific property that also varies with electric field strength (E) and gas pressure (p) between the sample and detector. In decreasing E/p the number of excitations occurring in the gas is greater than the number of ionisations, and large γ in these conditions is attributed mostly to the production of photoelectrons. However γ increases with larger values of E/p due to increased drift velocity and kinetic energy which, in addition to inelastic ion-surface processes such as excitation of meta stable states, contributes secondary electrons to the cascade by way of elastic collisions.

The ionisation potential of a sample partially determines γ, with low work functions producing higher γ as less ion, meta-stable and photon energies are required to extract electrons. γ is also generally smaller for molecules than atomic gases because moleucules have additional mechanisms for dissipating excitation energy (for example vibration, rotation and neutral dissociation).

Appendix B

EPYS Standard Operating Procedure

B.1 Purpose

The purpose of this SOP is to direct EPYS users in the appropriate operation and maintenance of the EPYS system, including safe practices with respect to gas delivery, high voltage ion detection and avoiding practices that may be harmful to the instrument.

B.2 Procedures

B.2.1 Venting EPYS Chamber

1. Make sure HV to the detector is turned off.
2. Close the inlet valve from shared gas lines (to avoid venting the shared gas lines).
3. Close the outlet valve to RGA (to avoid venting RGA).
4. Isolate chamber from TMP using large gate valve (make sure valve is completely closed).
5. Spin down TMP (if spinning). This can be done simply by removing the wireless remote that plugs into the side of the control box atop the pump.

6. Close the small manual outlet valve on underside of chamber (bypasses TMP to scroll pumps).

7. Close the inlet manual needle valve (to avoid a pressure burst when venting).

8. Open the manual inlet valves from EPYS gas lines.

9. Open nitrogen pneumatic valve by flicking 'Vent' on switch box to 'On' position. Nitrogen gas will begin entering the EPYS chamber.

10. Open up inlet manual needle valve to hasten the vent process.

11. When venting is complete, flick 'Vent' on switch box to 'Off' position

B.2.2 Removing/Loading samples into EPYS Chamber

1. Vent EPYS chamber (see section B.2.1).

2. Remove EPYS window (incrementally loosen nuts opposite one another - do **not** remove nuts completely one by one). O-ring can be left in place.

3. Use Allen key to loosen sample clamps. Be careful not to push loaded sample off the stage - if it drops it can be *extremely* difficult to retrieve.

4. Use clean tweezers to remove/insert sample. This can be difficult, using two pairs of tweezers to pick-up/place sample onto stage may prove simpler than using just one.

5. Fasten clamps over sample corners with the sample beneath detector, be sure to leave ample space free for incident light (approximately 5 mm diameter).

6. Replace EPYS chamber window and fasten nuts (tightening incrementally - do **not** fully tighten nuts one by one).

7. Pump EPYS chamber

B.2.3 Pumping EPYS Chamber

1. Make sure 'Vent' switch on switch box is in 'Off' position.

2. Make sure TMP is completely spun down (revolutions per second can be viewed on the TMP controller under 'Act Rot Speed').

3. (Optional, but recommended - avoids pressure burst to scroll pumps) Open up outlet manual valve on underside of EPYS chamber. Open up needle valve after manual valve. This will begin slowly pumping the chamber. Leave this for 5 minutes or longer.

4. Open up large gate valve. This will pump the chamber down rapidly.

5. When chamber pressure is below 0.1 Torr, spin up TMP. This can be done simply by plugging in the wireless remote that plugs into the side of the control box atop the pump.

6. Close manual valve on underside of chamber (if open).

7. Close all inlet valves to chamber.

In this configuration, the EPYS TMP can be used to pump on gas delivery lines and the RGA gas lines by opening up the appropriate valves.

Do **not** open chamber to any high pressure lines ($> 10^{-4}$ Torr). Damage to the TMP may occur if this happens.

B.2.4 Operating EPYS Chamber

B.2.4.1 Introducing Gas

1. Pump on shared gas line (minimum 1 hour) prior to introducing desired gas.

2. Make sure valve to RGA and valve to EPYS gas lines are closed.

3. Open up 'Beam Chem Monitor' on the EPYS laptop and begin tracking EPYS chamber pressure with 10 Torr Baratron.

4. Close all valves along gas line in preparation for gas introduction.

5. Close large EPYS chamber gate valve and begin spin down of TMP. Isolate TMP from roughing lines by closing the smaller gate valve on backside of the TMP.

6. Introduce desired gas to gas delivery line.
7. Open up valves along gas line beginning with valves closest to the source and ending with the EPYS inlet valve (making sure the MFC/needle valve between the source and EPYS chamber is closed).
8. Gas will begin bleeding into EPYS chamber. The gas flow rate into the EPYS chamber can be adjusted to bring the chamber pressure to 2 Torr (recommended operating pressure).
9. When the desired chamber pressure is reached, decrease in-flow rate to 0.5-2 sccm (recommended) and open manual valve on underside of EPYS chamber.
10. Adjust out-flow rate using manual needle valve on underside of EPYS chamber. If stable pressure cannot be achieved using only the manual out-flow needle valve, adjust the in-flow rate accordingly.

B.2.4.2 Set-up Light Delivery

1. Monochromator should be switched 'on' (turn 'on' if not already). electrometer should be switched 'on' (turn 'on' if not already).
2. Switch on Deuterium lamp. This will take several minutes to ignite.
3. Open LabView program "Spectrometer control - collection time - multi scan". (Check software is communicating with instruments. See section B.5 for troubleshooting advice if they are not communicating).
4. Plug electrometer into BNC feedthrough on EPYS chamber lid (to sample stage).
5. Plug HV supply into SHV feedthrough on EPYS chamber lid (to detector).
6. When Deuterium lamp is on, use LabView program to set monochromator wavelength to 0 nm (this will allow all of the light to pass through the monochromator).
7. Open monochromator shutter using the LabView program.
8. **Wearing UV safety goggles** (located on the optical bench) align the optic fibre over the EPYS chamber window so that light from the Deuterium lamp is incident on the sample (avoiding other materials - stage, clamps etc.). **Do not look into the fibre directly or with any optic, even if there is no light**.

9. Secure the optic fibre in place using the magnetic retort stand and clamp (located on the underside of the first EPYS system shelf).

10. Close monochromator shutter and set the wavelength to 195 nm using the LabView program.

B.2.4.3 Set-up Detector Voltage and Begin Measurement

1. Switch on HV supply (0 V).

2. Open monochromator shutter (wavelength should be set at 195 nm and light incident on the sample).

3. Increase voltage on HV supply slowly, observing the current passing though the electrometer. Continue increasing voltage until you have a good signal to noise ratio in the amplified photocurrent (noise levels are typically 200 fA, signal levels range from 10 - 1000 pA. These values can vary drastically depending on sample and gas.) The best operating detector voltage is often about 20 V below breakdown voltage (Ar - 270 V; H_2O - 600 V; O_2 - 550 V; NH_3 - 450 V; ethanol - 400 V; CO - 400 V).

4. When you have a stable pressure and current, set the monochromator wavelength to 350 nm.

5. Set the scan wavelengths from 350 - 180 nm (in the LabView program). Use wavelength increments of 1 nm.

6. Set the desired number of scans. Double check the shutter is open.

7. Press 'Go Scan', select a directory for the scan data and name the file. (It is recommended you include the sample material, gas type, pressure and voltage [and temp] in your file name, e.g. 'ZnO-Ar-2T-250V[-150C]').

8. Each scan will be saved as a text file containing the wavelength (nm) and corresponding current (A) in two adjacent columns. If you selected to perform several scans, the number of each scan will be tagged onto the end of your specified file name.

9. While measurement is in process, pay close attention to the pressure, making small adjustments to maintain constant pressure. Also continue to monitor the photocurrent passing through the electrometer, if it very noisy - decrease the voltage a little bit, if it very high (nA) over an entire scan - the gas has broken down and you need to decrease the voltage significantly (even turn off HV supply and reset the voltage).

B.2.4.4 Finish Measurement

1. When you have finished collecting data, turn down the HV supply then switch it off.
2. Switch off Deuterium lamp.
3. Close gas bottle (or gas source).
4. (When TMP completely spun down) Open small gate valve between TMP and roughing lines. Then open large gate valve between EPYS chamber and TMP. This will begin pumping out gas from the EPYS chamber and gas lines.
5. Let the scroll pump evacuate all gas from lines (including behind MFC or needle valve) until pressure is below 0.1 Torr.
6. Spin up TMP.
7. Close 'Beam Chem Monitor' and 'spectrometer control - collection time - multi scan' programs.
8. Leave both monochromator and electrometer switched on.

B.3 Heating and Cooling Sample Stage

Heating can be performed prior to and/or during measurement. Heating prior is often very useful for removing residual contaminants (like water), and heating during is very useful for elucidating temperature dependent effects like desorption and surface reactions. The stage can be heated from approximately 40°C up to 700°C safely (although without a quieter power supply, collecting spectra above about 350°C can be very difficult). I would also add that if collecting spectra while heating the stage, it is much

more effective to heat very gradually while collecting spectra, as raising the temperature rapidly tends to result in significant drifting of the offset current, and you will end up with less usable data.

Cooling the stage may also be performed by flowing cooled nitrogen gas through the stage. This is very useful for condensing adsorbates from the gas phase that do not stick at room temperature. The stage temperature can be varied from approximately -150°C up to 300°C with the cold stage feedthrough attached to the stage. The cold stage feedthrough is typically not attached, so must be installed specifically for cold measurements (this is because the lines delivering nitrogen gas to the stage are made of Teflon and will melt during heating experiments that exceed 300°C).

B.3.1 Heating

1. Plug in electrical feedthrough from heater power supply to front end of chamber (near EPYS control laptop).

2. Make sure voltage and current on power supply are both turned down. Switch power supply on.

3. With current knob turned all the way down - turn voltage knob all the way up.

4. Control the temperature using the current knob on the power supply. The temperature is measure with a Pt resistance thermometer embedded into the stage (the resistance of which can be converted to temperature). There is a calibration data sheet for the resistance to temperature conversion located in the EPYS SOP folder.

   In addition to resistance-temperature conversion, the calibration sheet also contains current-temperature conversion collected over many experiments. This can useful for getting an idea of what your current should be for a specific temperature. Please feel free to contribute to this calibration spreadsheet when performing experiences and heat treatments.

If you wish to heat prior to an experiment and begin the experiment as soon as you have completed the heat treatment, i recommend removing the electrical feedthrough as soon

as the power supply has been switched off. This will reduce the electrical noise in the spectra, although, while rapid cooling is taking place the current offset will drift.

B.3.2 Cooling

Setting up the cold stage requires opening up the chamber to install the nitrogen flow feedthrough.

1. Vent chamber (Section B.2.1), and remove chamber lid. Loosen nuts opposite one another incrementally - do not completely remove them one by one.
2. Remove the 4" flange located on the top-back corner of the chamber, near the RGA feedthrough.
3. Fasten cold stage feedthrough onto port, with Teflon tubing on the inside of the EPYS chamber.
4. Attach Teflon tubing to sample stage (they will push-fit onto steel tubes either side of chamber, then cap must be screwed on to form vacuum seal).
5. Close chamber and pump down (section B.2.3). Make sure high vacuum is reached.
6. Now attach the Teflon line from the liquid nitrogen dewar (40 L often used in CL lab, smaller Styrofoam dewar is kept at back of lab) to the air-side of the cold stage feedthrough.
7. Begin flowing nitrogen gas through the lines slowly.
8. Fill dewar with liquid nitrogen and submerge spiraled line into dewar.

You should feel cold nitrogen gas flowing out of the cold stage feedthrough. It will take approximately 20 minutes to reach a steady state temperature. You can adjust the temperature by adjusting the nitrogen gas flow. reaching liquid nitrogen temperature (-196 C) requires a high flow of nitrogen through the stage, and it is difficult to make measurements at these temperature due to electrical noise generated by vibrations in the stage. It is possible to acquire good data at -150 C.

B.4 Calibrate Light Delivery

Calibrating the wavelength on the monochromator is a standard procedure. It requires a spectral lamp with lines in the UV region (Ne or Hg will suffice) and preferably a PMT (or a CCD detector with a high spectral resolution). The monochromator control program (Traq Basic - which communicates with the PMT) has a wavelength calibration function built in (calibrate wavelength). The 'calibrate wavelength' function is adequate as you will only be looking at a narrow wavelength range (350-180 nm). You also have the option of a more thorough calibration which finds the first three coefficients in a polynomial that controls the grating position as a function of desired wavelengths.

The spectral lamp should be placed at the entrance aperture to the monochromator and the optic fibre into the entrance to the PMT. The PMT requires a HV supply and a power meter to measure its output. It is controlled using the Traq basic program which can be found on the EPYS laptop desktop. The power meter GPIB must be plugged into the monochromator (and the electrometer removed). Instructions for operation of the PMT can be found with the PMT and power meter.

Make sure no stray light is entering the PMT, which requires the monochromator exit, fibre entrance and coupling optics to be covered with light blocking cloths, and the PMT itself should be shrouded in light blocking cloths (aluminium foil can be used before the cloth to help keep light out). Close the exit aperture on the monochromator completely to achieve the highest spectra resolution.

Switch on spectra lamp and allow 15 minutes to warm up (spectral lines will shift during this period). switch on PMT - monitor the output voltage, do not allow to exceed 2 V. Adjust the high voltage on the PMT appropriately. Use Traq basic to perform monochromator scans across the range of the spectra lines. Identify the line position and use 'Go To Wavelength' function to move the monochromator to those wavelengths. When you have identified the peak, cross reference your wavelength with NIST data for the wavelength of the spectral line at that position. Use the 'Calibrate Wavelength' function to set the observed wavelength (on the monochromator) to the real wavelength (NIST).

If you use a CCD detector, you can use the EPYS monochromator control program to calibrate the wavelength and do not need to block stray light.

B.4.1 Gathering System Response

The system response is necessary to correct the EPYS data i.e. make it usable. The response is the intensity spectrum of light that reaches the sample. It is best collected with a PMT (or a high resolution CCD - the existing CCD detector at the MAU has a FWHM spectral resolution of 7 nm)).

The system response is collected with a PMT by measuring a full spectrum from the light source after having passed through all the optics before the sample. Light from the Deuterium lamp passes through the focusing lens, then into the monochromator (controlled by the EPYS computer), through the fiber coupling optics, the fiber and then through the chamber window finally into the PMT. It is important to eliminate stray light again, so that all openings between the monochromator exit aperture and PMT are closed to light.

When you have the raw spectrum collected with the PMT, you must then correct this data with the PMT response (which is located in an Igor Pro experiment 'PYS spectral analysis'). this final spectrum is the system response, and raw EPYS data must be divided by this spectrum to correct for the changing light intensity with incident wavelength.

If you are able to get a high spectral resolution UV CCD detector, this process becomes much simpler, and probably more accurate.

B.5 Troubleshoot LabView – Instrument Communication Errors

B.5.1 Monochromator

Occasionally the LabView program appears to not communicate with the monochromator. This typically occurs if the monochromator has been switched off and then on again. First check the device manager to ensure the GPIB connection is working. If not: turn off monochromator; shut down computer; remove GPIB connection from monochromator end, and put firmly back in place (this may require removing the electrometer GPIB

as well); start up computer; turn on monochromator - If it is still not registering in NI device monitor - try replacing the GBIP cable.

If the monochromator is showing up on the device manager, but setting the wavelength to 0 nm does not result in all the light coming out of the fiber (and the shutter is open) this is because the monochromator has had a mechanical fault. This occurs when the monochromator is switched on - it should make a very audible noise as the gratings undergo a full revolution. If it does not - then the rotating grating plate has become stuck, and the monochromator will need re-calibration. This can be more difficult than a regular calibration because the wavelength range you must traverse to find a spectral line is around 2000 nm. It is recommended to use a CCD detector to first locate the appropriate spectral lines before using the PMT.

The most effective way to avoid this situation is to leave the monochromator switched on. It may also prevent unnecessary frustration if you are aware this may occur after a power outage or annual PAT test.

B.5.2 Beam Chem Monitor

A data acquisition (DAQ) board that receives output from the 10 Torr Baratron, and communicates with the beam chem monitor, can occasionally fail to register on the beam chem GUI. This only occurs when people take the DAQ board to use for other purposes and replace it with a different board. The device manager creates a new identity for the DAQ boards each time they are swapped (even if the same boards are repeatedly swapped back and forth) and the beam chem monitor will only take the first identity. To remedy this you must first delete the existing identities for the instrument, then punish the person that swapped the DAQ board.

B.6 Troubleshoot Hardware Failure

If you are unable to collect spectra - and everything appears to be working properly, its most likely that there is either a broken electrical connection or no light is reaching the sample.

First check that the light is reaching the sample by making sure the shutter is open, and check the filter wheel at the exit aperture to make sure it is allowing light to pass. You can check there is light by driving the wavelength to 500 nm and observe green light reflecting off a surface. If there is still no light - the monochromator may need re-calibration (see Section B.5.1).

The simplest way to identify whether all electrical contacts are intact is to plug the HV and electrometer into the chamber lid - then turn the voltage up and down while observing the current on the electrometer - if a small current is induced when changing the voltage - then everything is connected appropriately.

If you have a broken electrical contact - it is most likely the pin spot-welded onto the stage, but could be four other points of contact (ground feedthrough pin, pin between ground cable and stage cable, HV feedthrough and the connection between the HV and the detector). Fixing any of these requires removing the lid - and if its one of the four listed in brackets - just reconnecting them. If the stage connection is broken, the stage must be removed from the system, and the pin re-welded onto the stage. This must then be cleaned and baked before mounting into position and resuming measurements.

B.7 Data Processing and Analysis

All EPYS data is collected in wavelength, but is best plotted vs energy - as it tells us about the electronic/energetic structure of the material under investigation. The energy at which the EPYS spectra begins to rise marks the minimum energy require to liberate electrons from the material - this is typically the work function in metals, or the ionisation potential (electron affinity) in semiconductors. Whether its the electron affinity or ionisation potential depends on the type (p/n) and carrier concentration of the semiconductor,

All data must be corrected with the system response, this normalises the photocurrent to a constant number of incident photons. The shape of corrected EPYS spectra is the integral of the effective density of states.

The spectra may be manipulated to determine things like threshold values and the presence of multiple thresholds. Typically the processing involves taking the square or

cube root of the yield - which should lead to a linear yield curve as a function of energy. 'PYS Spectral Analysis' contains a macro that performs these operations on collected spectra. More background information about these processes has been written by J. M. Ballantyne in his 1972 'Effect of phonon energy loss on photoemissive yield near threshold' [55].

B.7.1 EPYS Spectral Analysis in Igor Pro

All raw EPYS data can be automatically imported and processed in an Igor Pro experiment file - 'PYS Spectral Analysis 7'.

B.8 Using the EPYS Chamber for DC Plasma Treatment

The EPYS system can be used to generate a DC plasma between the stage and detector for sample treatments. Spectra cannot be collected during this process.

1. Load sample. Pump Chamber.
2. Introduce Gas to desired pressure (several Torr recommended).
3. Plug in HV supply to detector (positive bias).
4. Plug in secondary HV supply to stage (negative bias). Do **not** run DC plasma with electrometer plugged into stage.
5. Switch on detector HV supply and set to approximately 200 V.
6. Switch on stage HV supply and increase voltage until plasma generated.

Bibliography

[1] B Feuerbacher and R F Willis. Photoemission and electron states at clean surfaces. *Journal of Physics C: Solid State Physics*, 9(2), 2001.

[2] F Reinert and S Hüfner. Photoemission spectroscopyfrom early days to recent applications. *New Journal of Physics*, 7(1):97, 2005.

[3] R Courths and S Hüfner. Photoemission experiments on copper. *Physics Reports*, 112(2):53–171, 1984.

[4] S Hüfner, R Claessen, F Reinert, T Straub, V N Strocov, and P Steiner. Photoemission spectroscopy in metals: band structure-fermi surface–spectral function. *Journal of electron spectroscopy and related phenomena*, 100(1):191–213, 1999.

[5] M Alnot, J J Ehrhardt, and J A Barnard. A characterization of heterogeneous Pt surfaces by work function measurements and photoemission of adsorbed xenon. *Surface Science*, 208(3):285–305, 1989.

[6] G M Guichar, G A Garry, and C A Sébenne. Photoemission yield spectroscopy of electronic surface states on germanium (111) surfaces. *Surface Science*, 85(2): 326–334, 1979.

[7] R H Williams, G P Srivastava, and I T McGovern. Photoelectron spectroscopy of solids and their surfaces. *Reports on Progress in Physics*, 43(12):1357, 1980.

[8] R H Williams and J I Polanco. The electronic structure of chalcogenide solids: A photoemission study of ordered and disordered selenium and tellurium. *Journal of Physics C: Solid State Physics*, 7(15):2745, 1974.

[9] G A Somorjai, H Frei, and J Y Park. Advancing the frontiers in nanocatalysis, biointerfaces, and renewable energy conversion by innovations of surface techniques. *Journal of the American Chemical Society*, 131(46):16589–16605, 2009.

[10] G A Somorjai and J Y Park. Concepts, instruments, and model systems that enabled the rapid evolution of surface science. *Surface Science*, 603(10):1293–1300, 2009.

[11] C T Au, W Hirsch, and W Hirschwald. Adsorption of carbon monoxide and carbon dioxide on annealed and defect zinc oxide (0001) surfaces studied by photoelectron spectroscopy (xps and ups). *Surface Science*, 197(3):391–401, 1988.

[12] M Chen, X Wang, Y H Yu, Z L Pei, X D Bai, C Sun, R F Huang, and L S Wen. X-ray photoelectron spectroscopy and auger electron spectroscopy studies of al-doped ZnO films. *Applied Surface Science*, 158(1):134–140, 2000.

[13] D J Cooke, A Marmier, and S C Parker. Surface structure of (1010) and (1120) surfaces of ZnO with density functional theory and atomistic simulation. *The Journal of Physical Chemistry B*, 110(15):7985–7991, 2006.

[14] M Kunat, G Girol, U Burghaus, and C Wöll. The interaction of water with the oxygen-terminated, polar surface of ZnO. *The Journal of Physical Chemistry B*, 107(51):14350–14356, 2003.

[15] P R Norton, J W Goodale, and E B Selkirk. Adsorption of co on Pt (111) studied by photoemission, thermal desorption spectroscopy and high resolution dynamic measurements of work function. *Surface Science*, 83(1):189–227, 1979.

[16] K Jacobi, G Zwicker, and A Gutmann. Work function, electron affinity and band bending of zinc oxide surfaces. *Surface Science*, 141(1):109–125, 1984.

[17] K Hirose, A Uchiyama, T Noguchi, and M Uda. Surface states observed by photoemission yield spectroscopy on GaAs (001) surfaces with different superstructures. *Applied surface science*, 56:11–14, 1992.

[18] G Ertl, M Neumann, and K M Streit. Chemisorption of CO on the Pt(111) surface. *Surface Science*, 64(2):393, 1977.

[19] W Göpel, G Rocker, and R Feierabend. Intrinsic defects of TiO_2 (110): Interaction with chemisorbed O_2, H_2, CO, and CO_2. *Physical Review B*, 28(6):3427, 1983.

[20] Kian Ping Loh, XN Xie, SW Yang, and JC Zheng. Oxygen adsorption on (111)-oriented diamond: a study with ultraviolet photoelectron spectroscopy,

temperature-programmed desorption, and periodic density functional theory. *The Journal of Physical Chemistry B*, 106(20):5230–5240, 2002.

[21] P S Cremer, X Su, Y R Shen, and G A Somorjai. Ethylene hydrogenation on Pt (111) monitored in situ at high pressures using sum frequency generation. *Journal of the American Chemical Society*, 118(12):2942–2949, 1996.

[22] D C Tang, K S Hwang, M Salmeron, and G A Somorjai. High pressure scanning tunneling microscopy study of CO poisoning of ethylene hydrogenation on Pt (111) and rh (111) single crystals. *The Journal of Physical Chemistry B*, 108(35): 13300–13306, 2004.

[23] M D Ackermann, T M Pedersen, B L M Hendriksen, O Robach, S C Bobaru, I Popa, C Quiros, H Kim, B Hammer, S Ferrer, et al. Structure and reactivity of surface oxides on Pt (110) during catalytic CO oxidation. *Physical Review Letters*, 95(25):255505, 2005.

[24] P J Feibelman and D E Eastman. Photoemission spectroscopycorrespondence between quantum theory and experimental phenomenology. *Physical Review B*, 10(12):4932, 1974.

[25] K Shimada. *High-resolution Photoemission Spectroscopy of Solids Using Synchrotron Radiation*. Springer, 2007.

[26] K Kobayashi. Hard x-ray photoemission spectroscopy. *Nuclear Instruments and Methods in Physics Research Section A: Accelerators, Spectrometers, Detectors and Associated Equipment*, 601(1):32–47, 2009.

[27] H P Bonzel and C Kleint. On the history of photoemission. *Progress in surface science*, 49(2):107–153, 1995.

[28] J Frenkel. Some remarks on the theory of the photoelectric effect. *Physical Review*, 38(2):309, 1931.

[29] P D Innes. On the velocity of the cathode particles emitted by various metals under the influence of röntgen rays, and its bearing on the theory of atomic disintegration. *Proceedings of the Royal Society of London. Series A, Containing Papers of a Mathematical and Physical Character*, 79(532):442–462, 1907.

[30] E Rutherford. *Radioactive substances and their radiations.* University Press; New York: GP Putnam's sons, 1913.

[31] E Rutherford. The radiation and emanation of radium. *Scientific American*, 58: 24073–24075, 1904.

[32] R A Millikan and C F Eyring. Laws governing the pulling of electrons out of metals by intense electrical fields. *Physical Review*, 27(1):51, 1926.

[33] R A Millikan. The extension of the ultra-violet spectrum. *The Astrophysical Journal*, 52:47, 1920.

[34] WL Schaich and NW Ashcroft. Model calculations in the theory of photoemission. *Physical Review B*, 3(8):2452, 1971.

[35] C N Berglund and WE Spicer. Photoemission studies of copper and silver: theory. *Physical Review*, 136(4A):A1030, 1964.

[36] E Yablonovitch and E O Kane. Band structure engineering of semiconductor lasers for optical communications. *Lightwave Technology, Journal of*, 6(8):1292–1299, 1988.

[37] Marvin L Cohen and T K Bergstresser. Band structures and pseudopotential form factors for fourteen semiconductors of the diamond and zinc-blende structures. *Physical Review*, 141(2):789, 1966.

[38] E O Kane. Thomas-fermi approach to impure semiconductor band structure. *Physical Review*, 131(1):79, 1963.

[39] D Brust and E O Kane. Band-structure effects and many-particle scattering corrections in the far-ultraviolet spectra of Ge and Si. *Physical Review*, 176(3):894, 1968.

[40] T E Fischer. Photoemission and surfaces. *Journal of Vacuum Science & Technology*, 9(2):860–867, 1972.

[41] R A Powell and W E Spicer. Photoemission studies of the cesiation of ZnO. *Journal of Applied Physics*, 48(10):4311–4314, 1977.

[42] T Gustafsson, E W Plummer, D E Eastman, and J L Freeouf. Interpretation of the photoelectron spectra of molecularly adsorbed CO. *Solid State Communications*, 17(3):391–396, 1975.

[43] W E Spicer. Photoemissive, photoconductive, and optical absorption studies of alkali-antimony compounds. *Physical review*, 112(1):114, 1958.

[44] L F Wagner and W E Spicer. Observation of a band of silicon surface states containing one electron per surface atom. *Physical Review Letters*, 28(21):1381, 1972.

[45] G W Gobeli and E O Kane. Dependence of the optical constants of silicon on uniaxial stress. *Physical Review Letters*, 15(4):142, 1965.

[46] J W Gadzuk and M Šunjić. Excitation energy dependence of core-level x-ray-photoemission-spectra line shapes in metals. *Physical Review B*, 12(2):524, 1975.

[47] Douglas M Collins, James B Lee, and WE Spicer. A photoemission and thermal desorption study of carbon monoxide and oxygen adsorbed on platinum. *Surface Science*, 55(2):389–402, 1976.

[48] P R Norton. A photoelectron spectroscopic study of the adsorption and reactivity of oxygen on platinum. *Journal of Catalysis*, 36(2):211–223, 1975.

[49] G W Gobeli, F G Allen, and E O Kane. Polarization evidence for momentum conservation in photoelectric emission from germanium and silicon. *Physical Review Letters*, 12(4):94, 1964.

[50] A Liebsch. Theory of photoemission from localized adsorbate levels. *Physical Review B*, 13(2):544, 1976.

[51] J A Pople and M Gordon. Molecular orbital theory of the electronic structure of organic compounds. i. substituent effects and dipole moments. *Journal of the American Chemical Society*, 89(17):4253–4261, 1967.

[52] G Feher and E A Gere. Electron spin resonance experiments on donors in silicon. ii. electron spin relaxation effects. *Physical Review*, 114(5):1245, 1959.

[53] W B Mims. Amplitudes of superhyperfine frequencies displayed in the electron-spin-echo envelope. *Physical Review B*, 6(9):3543, 1972.

[54] W B Mims. Envelope modulation in spin-echo experiments. *Physical Review B*, 5 (7):2409, 1972.

[55] J M Ballantyne. Effect of phonon energy loss on photoemissive yield near threshold. *Physical Review B*, 6(4):1436, 1972.

[56] M Honda, K Kanai, K Komatsu, Y Ouchi, H Ishii, and K Seki. Atmospheric effect on the ionization energy of titanyl phthalocyanine thin film as studied by photoemission yield spectroscopy. *Molecular Crystals and Liquid Crystals*, 455(1): 219–225, 2006.

[57] M Honda, K Kanai, Ki Komatsu, Y Ouchi, H Ishii, and K Seki. Atmospheric effect of air, N_2, O_2, and water vapor on the ionization energy of titanyl phthalocyanine thin film studied by photoemission yield spectroscopy. *Journal of Applied Physics*, 102(10):103704, 2007.

[58] S Yagyu, M Yoshitake, T Kim, and T Chikyow. Consideration of the threshold of secondary electrons in photoelectron yield spectroscopy (PYS). *Journal of the Vacuum Society of Japan*, 53:187–190, 2010.

[59] I D Baikie, A C Grain, J Sutherland, and J Law. Ambient pressure photoemission spectroscopy of metal surfaces. *Applied Surface Science*, 323:45–53, 2014.

[60] C A Sébenne, D Bolmont, G Guichar, and M Balkanski. Surface states from photoemission threshold measurements on a clean, cleaved, Si (111) surface. *Physical Review B*, 12(8):3280, 1975.

[61] C A Sébenne. High-resolution photoemission yield and surface states in semiconductors. *Il Nuovo Cimento B (1971-1996)*, 39(2):768–780, 1977.

[62] G M Guichar, C A Sébenne, and G A Garry. Intrinsic and defect-induced surface states of cleaved GaAs (110). *Physical Review Letters*, 37(17):1158, 1976.

[63] G W Gobeli and F G Allen. Direct and indirect excitation processes in photoelectric emission from silicon. *Physical Review*, 127(1):141, 1962.

[64] G W Gobeli and F G Allen. Photoelectric properties and work function of cleaved germanium surfaces. *Surface Science*, 2:402–408, 1964.

[65] GD Mahan. Theory of photoemission in simple metals. *Physical Review B*, 2(11): 4334, 1970.

[66] *Ferromagnetism and Photoemission in Transition Metals*, volume 10, 1973. AIP Publishing.

[67] E O Kane. Two-level model of heterojunction band offsets. *Journal of Vacuum Science & Technology B*, 4(4):1051–1054, 1986.

[68] A R Gentle, G B Smith, and S E Watkins. Discharge amplified photo-emission from ultra-thin films applied to tuning work function of transparent electrodes in organic opto-electronic devices. *Applied Surface Science*, 285:110–114, 2013.

[69] K Kanai, M Honda, H Ishii, Y Ouchi, and K Seki. Interface electronic structure between organic semiconductor film and electrode metal probed by photoelectron yield spectroscopy. *Organic Electronics*, 13(2):309–319, 2012.

[70] G M Guichar, M Balkanski, and C A Sébenne. Semiconductor surface state spectroscopy. *Surface Science*, 86:874–887, 1979.

[71] G M Guichar, C A Sébnne, and C D Thuault. Electronic surface properties of cleaved gap (110). *Surface Science*, 86:789–793, 1979.

[72] G M Guichar, F Houzay, R Pinchaux, and Y Petroff. Dangling bond surface state of Si (111): New results. *Solid State Communications*, 38(9):809–813, 1981.

[73] D Bolmont, Ping Chen, CA Sébenne, and F Proix. Structural and electronic properties of cleaved Si (111) upon room-temperature formation of an interface with ag. *Physical Review B*, 24(8):4552, 1981.

[74] F Maier, J Ristein, and L Ley. Electron affinity of plasma-hydrogenated and chemically oxidized diamond (100) surfaces. *Physical Review B*, 64(16):165411, 2001.

[75] J Ristein, W Stein, and L Ley. Defect spectroscopy and determination of the electron diffusion length in single crystal diamond by total photoelectron yield spectroscopy. *Physical review letters*, 78(9):1803, 1997.

[76] D Takeuchi, S-G Ri, H Kato, C E Nebel, and S Yamasaki. Total photoyield experiments on hydrogen terminated n-type diamond. *Diamond and Related Materials*, 14(11):2019–2022, 2005.

[77] D Yamashita, Y Nakajima, A Ishizaki, and M Uda. Photoelectron spectrometer equipped with open counter for electronic structures of organic materials. *Journal of Surface Analysis*, 14(4):433–436, 2008.

[78] K Seki and K Kanai. Development of experimental methods for determining the electronic structure of organic materials. *Molecular Crystals and Liquid Crystals*, 455(1):145–181, 2006.

[79] K Kanai, M Honda, H Ishii, Y Ouchi, and K Seki. Interface electronic structure between organic semiconductor film and electrode metal probed by photoelectron yield spectroscopy. *Organic Electronics*, 13(2):309 – 319, 2012.

[80] H Ishii, H Kinjo, T Sato, S I Machida, and Y Nakayama. *Photoelectron yield spectroscopy for organic materials and interfaces*. 2015. cited By 0.

[81] Yasuo Nakayama, Shinichi Machida, Takeo Minari, Kazuhito Tsukagishi, Yutaka Noguchi, and Hisao Ishii. Direct observation of the electronic states of single crystalline rubrene under ambient condition by photoelectron yield spectroscopy. *Applied Physics Letters*, 93(17):173305, 2008.

[82] T Noguchi, S Nagashima, and M Uda. An electron counting mechanism for the open counter operated in air. *Nuclear Instruments and Methods in Physics Research Section A: Accelerators, Spectrometers, Detectors and Associated Equipment*, 342(2):521–526, 1994.

[83] A Von Engel and L Marton. Ionized gases. *Physics Today*, 18:64, 1965.

[84] Essam Nasser. *Fundamentals of gaseous ionization and plasma electronics*. Wiley-Interscience, 1971.

[85] A N Farley and J S Shah. Primary considerations for image enhancement in high-pressure scanning electron microscopy. *Journal of Microscopy*, 158(3):389–401, 1990.

[86] BL Thiel, IC Bache, AL Fletcher, P Meredith, and AM Donald. An improved model for gaseous amplification in the environmental sem. *Journal of Microscopy*, 187(3):143–157, 1997.

[87] M Toth and MR Phillips. The role of induced contrast in images obtained using the environmental scanning electron microscope. *Scanning*, 22(6):370–379, 2000.

[88] P A Redhead. Multiple ionization of the rare gases by successive electron impacts (0-250 ev): i. appearance potentials and metastable ion formation. *Canadian Journal of Physics*, 45(5):1791–1812, 1967.

[89] D Stokes. *Principles and practice of variable pressure: environmental scanning electron microscopy (VP-ESEM)*. John Wiley & Sons, 2008.

[90] K Chandrakar and A Von Engel. The starting mechanism of the first stage of the ring discharge. In *Proceedings of the Royal Society of London A: Mathematical, Physical and Engineering Sciences*, volume 284, pages 442–454. The Royal Society, 1965.

[91] AL Fletcher, BL Thiel, and AM Donald. Amplification measurements of alternative imaging gases in environmental sem. *Journal of Physics D: Applied Physics*, 30(15):2249, 1997.

[92] B L Thiel and M Toth. Secondary electron contrast in low-vacuum/ environmental scanning electron microscopy of dielectrics. *Journal of applied physics*, 97(5): 051101, 2005.

[93] T Yamada, T J Chuang, H Seki, and Y Mitsuda. Chemisorption of fluorine, hydrogen and hydrocarbon species on the diamond c (111) surface. *Molecular Physics*, 76(4):887–908, 1992.

[94] N Miljkovic, R Enright, and EN Wang. Effect of droplet morphology on growth dynamics and heat transfer during condensation on superhydrophobic nanostructured surfaces. *ACS nano*, 6(2):1776–1785, 2012.

[95] CA Amadei, CY Lai, MJ Esplandiu, F Alzina, CD Vecitis, A Verdaguer, and M Chiesa. Elucidation of the wettability of graphene through a multi-length-scale investigation approach. *RSC Advances*, 5(49):39532–39538, 2015.

[96] K Rykaczewski, J Chinn, M L Walker, J H Scott, A Chinn, and W Jones. Dynamics of nanoparticle self-assembly into superhydrophobic liquid marbles during water condensation. *ACS nano*, 5(12):9746–9754, 2011.

[97] S Lippincott. A conversation with robert f. christy–part ii. *Physics in Perspective*, 8(4):408–450, 2006.

[98] K Rykaczewski. Microdroplet growth mechanism during water condensation on superhydrophobic surfaces. *Langmuir*, 28(20):7720–7729, 2012.

[99] B Carrier, L Wang, M Vandamme, R Pellenq, Ml Bornert, A Tanguy, and H Van Damme. Esem study of the humidity-induced swelling of clay film. *Langmuir*, 29(41):12823–12833, 2013.

[100] M P Rossi, Hi Ye, Y Gogotsi, S Babu, P Ndungu, and J C Bradley. Environmental scanning electron microscopy study of water in carbon nanopipes. *Nano Letters*, 4(5):989–993, 2004.

[101] S J Randolph, A Botman, and M Toth. Capsule-free fluid delivery and beam-induced electrodeposition in a scanning electron microscope. *RSC Advances*, 3 (43):20016–20023, 2013.

[102] M Bresin, A Botman, S J Randolph, M Straw, and J T Hastings. Liquid phase electron-beam-induced deposition on bulk substrates using environmental scanning electron microscopy. *Microscopy and Microanalysis*, 20(2):376–384, 2014.

[103] J M Perry, Z D Harms, and S C Jacobson. 3D nanofluidic channels shaped by electron-beam-induced etching. *Small*, 8(10):1521, May 2012.

[104] M Toth, C J Lobo, W R Knowles, M R Phillips, M T Postek, and A E Vladár. Nanostructure fabrication by ultra-high-resolution environmental scanning electron microscopy. *Nano letters*, 7(2):525–530, 2007.

[105] T D Yuzvinsky, A M Fennimore, W Mickelson, C Esquivias, and A Zettl. Precision cutting of nanotubes with a low-energy electron beam. *Appl. Phys. Lett.*, 86(5): 053109, 2005.

[106] C J Lobo, A Martin, M R Phillips, and M Toth. Electron beam induced chemical dry etching and imaging in gaseous NH_3 environments. *Nanotechnology*, 23(37): 375302, 2012.

[107] J Niitsuma, X Yuan, S Koizumi, and T Sekiguchi. Nanoprocessing of diamond using a variable pressure scanning electron microscope. *Jpn. J. Appl. Phys.*, 45 (1–3), 2006.

[108] M Toth, W R Knowles, and B L Thiel. Secondary electron imaging of nonconductors with nanometer resolution. *Applied physics letters*, 88(2):023105, 2006.

[109] S O Kucheyev, M Toth, T F Baumann, A V Hamza, J Ilavsky, W R Knowles, C K Saw, B L Thiel, V Tileli, and T van Buuren. Structure of low-density nanoporous dielectrics revealed by low-vacuum electron microscopy and small-angle x-ray scattering. *Langmuir*, 23(2):353–356, 2007.

[110] D J Stokes, B L Thiel, and A M Donald. Direct observation of water-oil emulsion systems in the liquid state by environmental scanning electron microscopy. *Langmuir*, 14(16):4402–4408, 1998.

[111] B L Thiel, M Toth, R P M Schroemges, J J Scholtz, G Van Veen, and W R Knowles. A two-stage gas amplification secondary electron detector for ultra-high resolution imaging. *Microscopy and Microanalysis*, 10(S02):1058–1059, 2004.

[112] M Toth, M Uncovsky, W R Knowles, and F S Baker. Secondary electron imaging at gas pressures in excess of 1kpa. *Applied Physics Letters*, 91(5):053122, 2007.

[113] T W Shanley, A A Martin, I Aharonovich, and M Toth. Localized chemical switching of the charge state of nitrogen-vacancy luminescence centers in diamond. *Applied Physics Letters*, 105(6):063103, 2014.

[114] J R E Christy, Y Hamamoto, and Kl Sefiane. Flow transition within an evaporating binary mixture sessile drop. *Physical Review Letters*, 106(20):205701, 2011.

[115] L Shi, P Shen, D Zhang, Q Lin, and Q Jiang. Wetting and evaporation behaviors of water-ethanol sessile drops on PTFE surfaces. *Surface and Interface Analysis*, 41(12-13):951–955, 2009.

[116] Y Murakami, Y Miyauchi, S Chiashi, and S Maruyama. Direct synthesis of high-quality single-walled carbon nanotubes on silicon and quartz substrates. *Chemical Physics Letters*, 377(1-2):49–54, 2003.

[117] D Takagi, H Hibino, S Suzuki, Y Kobayashi, and Y Homma. Carbon nanotube growth from semiconductor nanoparticles. *Nano Letters*, 7(8):2272–2275, 2007.

[118] S Maruyama, E Einarsson, Y Murakami, and T Edamura. Growth process of vertically aligned single-walled carbon nanotubes. *Chemical Physics Letters*, 403 (4-6):320–323, 2005.

[119] W Zhou, Z Han, J Wang, Y Zhang, Z Jin, X Sun, Y Zhang, C Yan, and Y Li. Copper catalyzing growth of single-walled carbon nanotubes on substrates. *Nano letters*, 6(12):2987–2990, 2006.

[120] J Sun and Y Wang. Recent advances in catalytic conversion of ethanol to chemicals. *ACS Catalysis*, 4(4):1078–1090, 2014.

[121] M Choi, K Na, J Kim, Y Sakamoto, O Terasaki, and R Ryoo. Stable single-unit-cell nanosheets of zeolite mfi as active and long-lived catalysts. *Nature*, 461(7261): 246–249, 2009.

[122] G D Danilatos. Foundations of environmental scanning electron microscopy. *Advances in Electronics and Electron Physics*, 71(109-250), 1988.

[123] B L Thiel. Master curves for gas amplification in low vacuum and environmental scanning electron microscopy. *Ultramicroscopy*, 99(1):35–47, 2004.

[124] Bradley L Thiel. Master Murves for Gas Amplification in Low Vacuum and Environmental Scanning Electron Microscopy. *Ultramicroscopy*, 99(1), 2004.

[125] R Locht, B Leyh, W Denzer, G Hagenow, and H Baumgärtel. The photoionization of ammonia revisited. The vibrational autoionization of NH_3 and its three isotopomers in the 10–12 eV photon energy range. *Chemical Physics*, 155(3):407, 1991.

[126] K B Snow and T F Thomas. Mass spectrum, ionization potentials and appearance potentials for fragment ions of sulfuric acid vapor. *International Journal of Mass Spectrometry and Ion Processes*, 125(2-3):271, 1993.

[127] Richard D Bowen and Allan Maccoll. Low energy, low temperature mass spectra 2—low energy, low temperature mass spectra of some small saturated alcohols and ethers. *Organic Mass Spectrometry*, 19(8):379, 1984.

[128] Yuhai Jiang, Jinfeng Sun, and Lingde Wan. Additivity rule for the calculation of electron scattering from polyatomic molecules. *Physical Review A*, 62(6), 2000.

[129] H Deutsch, C Cornelissen, L Cespiva, V Bonacic-Koutecky, D Margreiter, and T D Märk. Total electron impact ionization cross sections of free molecular radicals: the failure of the additivity rule revisited. *International Journal of Mass Spectrometry and Ion Processes*, 129:43, 1993.

[130] H Deutsch, K Becker, R Basner, M Schmidt, and T D Märk. Application of the Modified Additivity Rule to the Calculation of Electron-Impact Ionization Cross Sections of Complex Molecules. *The Journal of Physical Chemistry A*, 102(45): 8819, 1998.

[131] R L Watson, Yong Peng, V Horvat, G J Kim, and R E Olson. Target Z dependence and additivity of cross sections for electron loss by 6-MeV/amu Xe 1 8 + projectiles . *Physical Review A*, 67(2), 2003.

[132] D Margreiter, H Deutsch, M Schmidt, and T D Märk. Electron impact ionization cross sections of molecules: Part ii. theoretical determination of total (counting) ionization cross sections of molecules: a new approach. *International Journal of Mass Spectrometry and Ion Processes*, 100:157–176, 1990.

[133] W Hwang, Y K Kim, and M Eugene Rudd. New model for electron-impact ionization cross sections of molecules. *The Journal of Chemical Physics*, 104(8): 2956–2966, 1996.

[134] M Toth, D R Daniels, B L Thiel, and A M Donald. Quantification of electron-ion recombination in an electron-beam-irradiated gas capacitor. *J. Phys. D*, 35(14): 1796–1804, January 2002.

[135] D H Baker, L D Doverspike, and R L Champion. Negative-ion and electron emission from surfaces at low impact energies. *Physical Review A*, 46(1):296, 1992.

[136] Özgür Ümit, Daniel Hofstetter, and Hadis Morkoc. ZnO devices and applications: a review of current status and future prospects. *Proceedings of the IEEE*, 98(7): 1255–1268, 2010.

[137] Ü Özgür, Ya I Alivov, A Teke, C Liu, A Teke, S Do gan, M A Reshchikov, S Doğan, V Avrutin, H Morkoç, S J Cho, and H Morkoç. A comprehensive review of ZnO materials and devices. *Journal of Applied Physics*, 98(4):041301, 2005.

[138] B K Meyer, B K Meyer, H Alves, D M Hofmann, H Alves, W Kriegseis, D M Hofmann, D Forster, W Kriegseis, F Bertram, D Forster, J Christen, F Bertram, A Hoffmann, J Christen, M Straßburg, A Hoffmann, M Straßburg, U Haboeck, M Dworzak, U Haboeck, and A V Rodina. Bound exciton and donor–acceptor pair recombinations in ZnO. *Physica Status Solidi (b)*, 241(2):231, 2004.

[139] B Meyer. First-principles study of the polar o-terminated ZnO surface in thermodynamic equilibrium with oxygen and hydrogen. *Physical Review B*, 69(4):045416, 2004.

[140] G D Sharma, R Kumar, S K Sharma, and M S Roy. Charge generation and photovoltaic properties of hybrid solar cells based on ZnO and copper phthalocyanines (cupc). *Solar Energy Materials and Solar Cells*, 90(7):933–943, 2006.

[141] Andreas Klein, Christoph Körber, André Wachau, Frank Säuberlich, Yvonne Gassenbauer, Steven P Harvey, Diana E Proffit, and Thomas O Mason. Transparent conducting oxides for photovoltaics: manipulation of Fermi level, work function and energy band alignment. *Materials*, 3(11):4892, 2010.

[142] Z Zhang and J T Yates. Band bending in semiconductors: chemical and physical consequences at surfaces and interfaces. *Chemical Reviews*, 112(10):5520, 2012.

[143] J H Kim, H Song, and E K Kim. Study of magnetic impurity as defects in ZnO grown by pulsed laser deposition. *Microelectronics Journal*, 40(2):283–285, 2009.

[144] S J Pearton, D P Norton, M P Ivill, A F Hebard, J M Zavada, W M Chen, and Irina A Buyanova. Ferromagnetism in transition-metal doped ZnO. *Journal of Electronic Materials*, 36(4):462–471, 2007.

[145] S K Mandal, A K Das, T K Nath, and Debjani Karmakar. Temperature dependence of solubility limits of transition metals (Co, Mn, Fe, and Ni) in ZnO nanoparticles. *Applied Physics Letters*, 89(14):144105, 2006.

[146] T M Børseth, B G Svensson, A Y Kuznetsov, P Klason, Q X Zhao, and M Willander. Identification of oxygen and zinc vacancy optical signals in ZnO. *Applied Physics Letters*, 89(26):262112, December 2006.

[147] E De la Rosa, S Sepulveda-Guzman, B Reeja-Jayan, A Torres, P Salas, N Elizondo, and M Jose Yacaman. Controlling the growth and luminescence properties of well-faceted ZnO nanorods. *The Journal of Physical Chemistry C*, 111(24):8489–8495, 2007.

[148] J H Kim, D Andeen, and F F Lange. Hydrothermal growth of periodic, single-crystal ZnO microrods and microtunnels. *Advanced Materials*, 18(18):2453–2457, 2006.

[149] K Maeda, M Sato, I Niikura, and T Fukuda. Growth of 2 inch ZnO bulk single crystal by the hydrothermal method. *Semiconductor Science and Technology*, 20 (4):S49, 2005.

[150] D Ehrentraut, H Sato, Y Kagamitani, H Sato, A Yoshikawa, and T Fukuda. Solvothermal growth of ZnO. *Progress in Crystal Growth and Characterization of Materials*, 52(4):280–335, 2006.

[151] D D Awschalom, L C Bassett, A S Dzurak, E L Hu, and J R Petta. Quantum spintronics: engineering and manipulating atom-like spins in semiconductors. *Science*, 339(6124):1174–1179, 2013.

[152] S A Wolf, D D Awschalom, R A Buhrman, J M Daughton, S Von Molnar, M L Roukes, A Y Chtchelkanova, and D M Treger. Spintronics: a spin-based electronics vision for the future. *Science*, 294(5546):1488–1495, 2001.

[153] J Nause and B Nemeth. Pressurized melt growth of ZnO boules. *Semiconductor Science and Technology*, 20(4):S45, 2005.

[154] S Monticone, R Tufeu, and Kanaev. Complex nature of the uv and visible fluorescence of colloidal ZnO nanoparticles. *The Journal of Physical Chemistry B*, 102 (16):2854, 1998.

[155] M Kunat, T Becker, U Burghaus, C Wöll, et al. Stability of the polar surfaces of ZnO: A reinvestigation using he-atom scattering. *Physical Review B*, 66(8): 081402, 2002.

[156] K Ogata, T Kawanishi, K Maejima, K Sakurai, S Fujita, and S Fujita. ZnO growth using homoepitaxial technique on sapphire and Si substrates by metalorganic vapor phase epitaxy. *Journal of Crystal Growth*, 237:553–557, 2002.

[157] W An, X Wu, and X C Zeng. Adsorption of o2, h2, CO, NH_3, and no2 on ZnO nanotube: a density functional theory study. *The Journal of Physical Chemistry C*, 112(15):5747–5755, 2008.

[158] S Anantachaisilp, S M Smith, C Ton-That, T Osotchan, A R Moon, and M R Phillips. Tailoring deep level surface defects in ZnO nanorods for high sensitivity ammonia gas sensing. *The Journal of Physical Chemistry C*, 118(46):27150, 2014.

[159] J B L Martins, E Longo, and C A Taft. CO_2 and NH_3 interaction with ZnO surface: An am1 study. *International Journal of Quantum Chemistry*, 70(2):367–374, 1998.

[160] W Ang, W Zhao, P Liu-Hua, L Wei-Wei, X Li, D Xiao-Chen, and H Wei. Room-temperature NH_3 gas sensor based on hydrothermally grown ZnO nanorods. *Chinese Physics Letters*, 28(8):080702, 2011.

[161] J B K Law and J T L Thong. Improving the NH_3 gas sensitivity of ZnO nanowire sensors by reducing the carrier concentration. *Nanotechnology*, 19(20):205502, 2008.

[162] M N R Ashfold, R P Doherty, N G Ndifor-Angwafor, D J Riley, and Y Sun. The kinetics of the hydrothermal growth of ZnO nanostructures. *Thin Solid Films*, 515 (24):8679–8683, 2007.

[163] D C Look, C Coşkun, B Claflin, and G C Farlow. Electrical and optical properties of defects and impurities in ZnO. *Physica B: Condensed Matter*, 340-342:32, 2003.

[164] L S Vlasenko and G D Watkins. Optical detection of electron paramagnetic resonance for intrinsic defects produced in ZnO by 2.5-mev electron irradiation in situ at 4.2 k. *Physical Review B*, 72(3):035203, 2005.

[165] N Kouklin. Cu-doped ZnO nanowires for efficient and multispectral photodetection applications. *Advanced Materials*, 20(11):2190, 2008.

[166] K Iwata, T Sakemi, A Yamada, P Fons, K Awai, T Yamamoto, M Matsubara, H Tampo, and S Niki. Growth and electrical properties of ZnO thin films deposited by novel ion plating method. *Thin Solid Films*, 445(2):274–277, 2003.

[167] D C Look, D C Reynolds, Joseph W Hemsky, R L Jones, and J R Sizelove. Production and annealing of electron irradiation damage in ZnO. *Applied Physics Letters*, 75(6):811–813, 1999.

[168] D C Look. Unusual electrical properties of hydrothermally grown ZnO. *Superlattices and Microstructures*, 42(1-6):284, 2007.

[169] D C Look, C Coşkun, B Claflin, and G C Farlow. Electrical and optical properties of defects and impurities in ZnO. *Physica B: Condensed Matter*, 340-342:32, 2003.

[170] W Gopel and U Lampe. Influence of defects on the electronic structure of zinc oxide surfaces. *Physical Review B*, 22(12):6447, 1980.

[171] O Schmidt, P Kiesel, D Ehrentraut, T Fukuda, and Noble M Johnson. Electrical characterization of ZnO, including analysis of surface conductivity. *Applied Physics A*, 88(1):71–75, 2007.

[172] A Janotti and C G Van de Walle. Native point defects in ZnO. *Physical Review B*, 76(16):165202, 2007.

[173] M D McCluskey and S J Jokela. Defects in ZnO. *J. Appl. Phys.*, 106(7):071101, October 2009.

[174] S J Clark, J Robertson, S Lany, and A Zunger. Intrinsic defects in ZnO calculated by screened exchange and hybrid density functionals. *Physical Review B*, 81(11): 115311, 2010.

[175] A Janotti and C G Van de Walle. New insights into the role of native point defects in ZnO. *Journal of Crystal Growth*, 287(1):58–65, 2006.

[176] F Hai-Bo, Y Shao-Yan, Z Pan-Feng, W Hong-Yuan, L Xiang-Lin, J Chun-Mei, Z Qin-Sheng, C Yong-Hai, and W Zhan-Guo. Investigation of oxygen vacancy and interstitial oxygen defects in ZnO films by photoluminescence and x-ray photoelectron spectroscopy. *Chinese Physics Letters*, 24(7):2108, 2007.

[177] S Lany and A Zunger. Dopability, intrinsic conductivity, and nonstoichiometry of transparent conducting oxides. *Physical Review Letters*, 98(4):045501, 2007.

[178] P Erhart, K Albe, and A Klein. First-principles study of intrinsic point defects in ZnO: Role of band structure, volume relaxation, and finite-size effects. *Physical Review B*, 73(20):205203, 2006.

[179] A F Kohan, G Ceder, D Morgan, and C G Van de Walle. First-principles study of native point defects in ZnO. *Physical Review B*, 61(22):15019, 2000.

[180] R Vidya, P Ravindran, H Fjellvåg, B G Svensson, E Monakhov, M Ganchenkova, and Risto M Nieminen. Energetics of intrinsic defects and their complexes in ZnO investigated by density functional calculations. *Physical Review B*, 83(4):045206, 2011.

[181] R Lindsay, E Michelangeli, B G Daniels, T V Ashworth, A J Limb, G Thornton, A Gutiérrez-Sosa, A Baraldi, R Larciprete, and S Lizzit. Impact of defects on the surface chemistry of ZnO (0001)-o. *Journal of the American Chemical Society*, 124(24):7117–7122, 2002.

[182] T Tatsumi, M Fujita, and N Kawamoto. Intrinsic defects in ZnO films grown by molecular beam epitaxy. *Japanese Journal of Applied Physics*, 43(5A):2602, 2004.

[183] A B Djurišić, Y H Leung, K H Tam, L Ding, W K Ge, H Y Chen, and S Gwo. Green, yellow, and orange defect emission from ZnO nanostructures: Influence of excitation wavelength. *Applied Physics Letters*, 88(10):103107, 2006.

[184] B Lin, Z Fu, and Y Jia. Green luminescent center in undoped zinc oxide films deposited on silicon substrates. *Applied Physics Letters*, 79(7):943–945, 2001.

[185] D Li, Y H Leung, A B Djurišić, Z T Liu, M H Xie, S L Shi, S J Xu, and W K Chan. Different origins of visible luminescence in ZnO nanostructures fabricated by the chemical and evaporation methods. *Applied Physics Letters*, 85(9):1601–1603, 2004.

[186] H Zeng, G Duan, Y Li, S Yang, H Xu, and W Cai. Blue luminescence of ZnO nanoparticles based on non-equilibrium processes: defect origins and emission controls. *Advanced Functional Materials*, 20(4):561–572, 2010.

[187] B K Meyer, H Alves, D M Hofmann, W Kriegseis, D Forster, F Bertram, J Christen, A Hoffmann, M Straßburg, and M Dworzak. Bound exciton and donor–acceptor pair recombinations in ZnO. *Physica Status Solidi (b)*, 241(2):231–260, 2004.

[188] Y F Lu, H Q Ni, Z H Mai, and Z M Ren. The effects of thermal annealing on ZnO thin films grown by pulsed laser deposition. *Journal of Applied Physics*, 88 (1):498–502, 2000.

[189] K Vanheusden, W L Warren, C H Seager, D R Tallant, J A Voigt, and B E Gnade. Mechanisms behind green photoluminescence in ZnO phosphor powders. *Journal of Applied Physics*, 79(10):7983–7990, 1996.

[190] G Srinivasan, R T Rajendra Kumar, and J Kumar. Li doped and undoped ZnO nanocrystalline thin films: a comparative study of structural and optical properties. *Journal of Sol-Gel Science and Technology*, 43(2):171–177, 2007.

[191] M A Reshchikov, J Q Xie, B Hertog, and A Osinsky. Yellow luminescence in ZnO layers grown on sapphire. *J. Appl. Phys.*, 103(10):103514, 2008.

[192] J H Cai, G Ni, G He, and Z Y Wu. Red luminescence in ZnO films prepared by a glycol-based pechini method. *Physics Letters A*, 372(22):4104–4108, 2008.

[193] P M Aneesh and M K Jayaraj. Red luminescence from hydrothermally synthesized eu-doped ZnO nanoparticles under visible excitation. *Bulletin of Materials Science*, 33(3):227–231, 2010.

[194] Y-J Lin and C-L Tsai. Changes in surface band bending, surface work function, and sheet resistance of undoped ZnO films due to NH_4 treatment. *Journal of Applied Physics*, 100(11):113721, 2006.

[195] S Anantachaisilp. *The effect of surface defects on the optical and electrical properties of ZnO nanorods.* PhD thesis, Shool of Mathematical and Physical Sciences, UTS, 2015.

[196] O F Schirmer and D Zwingel. The yellow luminescence of zinc oxide. *Solid State Communications*, 8(19):1559–1563, 1970.

[197] H Moormann, D Kohl, and G Heiland. Variations of work function and surface conductivity on clean cleaved zinc oxide surfaces by annealing and by hydrogen adsorption. *Surface Science*, 100(2):302, 1980.

[198] A Wei, X W Sun, C X Xu, Z L Dong, Y Yang, S T Tan, and W Huang. Growth mechanism of tubular ZnO formed in aqueous solution. *Nanotechnology*, 17(6): 1740, 2006.

[199] Y Sevinchan, P E Hopkinson, A A Bakulin, J Herz, M Motzkus, and Y Vaynzof. Improving charge separation across a hybrid oxide/polymer interface by cs doping of the metal oxide. *Advanced Materials Interfaces*, 2016.

[200] O T Hofmann, J-C Deinert, Y Xu, P Rinke, J Stähler, M Wolf, and M Scheffler. Large work function reduction by adsorption of a molecule with a negative electron

affinity: Pyridine on ZnO (101$^-$ 0). *The Journal of chemical physics*, 139(17): 174701, 2013.

[201] R K Swank. Surface properties of ii-vi compounds. *Physical Review*, 153(3):844, 1967.

[202] Y Yan, M M Al-Jassim, and S-H Wei. Oxygen-vacancy mediated adsorption and reactions of molecular oxygen on the ZnO (10 1$^-$ 0) surface. *Physical Review B*, 72(16):161307, 2005.

[203] M Grunze, W Hirschwald, and D Hofmann. Zinc oxide: Surface structure, stability, and mechanisms of surface reactions. *Journal of Crystal Growth*, 52:241–249, 1981.

[204] D Gordon. *Properties and growth of diamond*. INSPEC, the Institution of Electrical Engineers, 1994, 1994.

[205] C Santori, P E Barclay, K M C Fu, and R G Beausoleil. Vertical distribution of nitrogen-vacancy centers in diamond formed by ion implantation and annealing. *Physical Review B*, 79(12):125313, 2009.

[206] C Santori, P E Barclay, K M C Fu, R G Beausoleil, S Spillane, and M Fisch. Nanophotonics for quantum optics using nitrogen-vacancy centers in diamond. *Nanotechnology*, 21(27):274008, 2010.

[207] D Englund, B Shields, K Rivoire, F Hatami, J Vuckovic, H Park, and M D Lukin. Deterministic coupling of a single nitrogen vacancy center to a photonic crystal cavity. *Nano Letters*, 10(10):3922–3926, 2010.

[208] J Maze, J Taylor, and M Lukin. Electron spin decoherence of single nitrogen-vacancy defects in diamond. *Physical Review B*, 78(9):094303, 2008.

[209] C Santori, P E Barclay, K M C Fu, R G Beausoleil, S Spillane, and M Fisch. Nanophotonics for quantum optics using nitrogen-vacancy centers in diamond. *Nanotechnology*, 21(27):274008, June 2010.

[210] T Ishikawa, K M C Fu, C Santori, V M Acosta, R G Beausoleil, H Watanabe, S Shikata, and K M Itoh. Optical and spin coherence properties of nitrogen-vacancy centers placed in a 100 nm thick isotopically purified diamond layer. *Nano letters*, 12(4):2083–2087, 2012.

[211] L M Pham, D Le Sage, P L Stanwix, T K Yeung, D Glenn, A Trifonov, P Cappellaro, P R Hemmer, M D Lukin, H Park, A Yacoby, and R L Walsworth. Magnetic field imaging with nitrogen-vacancy ensembles. *New Journal of Physics*, 13(4): 045021, 2011.

[212] L Robledo, L Childress, H Bernien, B Hensen, P F A Alkemade, and R Hanson. High-fidelity projective read-out of a solid-state spin quantum register. *Nature*, 477(7366):574–578, 2011.

[213] A Ermakova, G Pramanik, J-M Cai, G Algara-Siller, U Kaiser, T Weil, Y-K Tzeng, H C Chang, L P McGuinness, M B Plenio, et al. Detection of a few metallo-protein molecules using color centers in nanodiamonds. *Nano Letters*, 13(7):3305–3309, 2013.

[214] S Kaufmann, D A Simpson, L T Hall, V Perunicic, P Senn, S Steinert, L P McGuinness, B C Johnson, T Ohshima, F Caruso, et al. Detection of atomic spin labels in a lipid bilayer using a single-spin nanodiamond probe. *Proceedings of the National Academy of Sciences*, 110(27):10894–10898, 2013.

[215] D Le Sage, K Arai, D R Glenn, S J DeVience, L M Pham, L Rahn-Lee, M D Lukin, A Yacoby, A Komeili, and R L Walsworth. Optical magnetic imaging of living cells. *Nature*, 496(7446):486–489, 2013.

[216] F Dolde, H Fedder, M W Doherty, T Nöbauer, F Rempp, G Balasubramanian, T Wolf, F Reinhard, L C L Hollenberg, F Jelezko, et al. Electric-field sensing using single diamond spins. *Nature Physics*, 7(6):459–463, 2011.

[217] J M Taylor, P Cappellaro, L Childress, L Jiang, D Budker, P R Hemmer, A Yacoby, R Walsworth, and M D Lukin. High-sensitivity diamond magnetometer with nanoscale resolution. *Nature Physics*, 4(10):810–816, 2008.

[218] L M Pham, D Le Sage, P L Stanwix, T K Yeung, D Glenn, A Trifonov, P Cappellaro, P R Hemmer, M D Lukin, H Park, A Yacoby, and R L Walsworth. Magnetic field imaging with nitrogen-vacancy ensembles. *New Journal of Physics*, 13(4): 045021, 2011.

[219] V V Dobrovitski, G D Fuchs, A L Falk, C Santori, and D D Awschalom. Quantum control over single spins in diamond. *Annu. Rev. Condens. Matter Phys.*, 4(1): 23–50, 2013.

[220] R Hanson, V V Dobrovitski, A E Feiguin, O Gywat, and D D Awschalom. Coherent dynamics of a single spin interacting with an adjustable spin bath. *Science*, 320 (5874):352–355, 2008.

[221] Yuen Yung Hui, Chia-Liang Cheng, and Huan-Cheng Chang. Nanodiamonds for optical bioimaging. *Journal of Physics D: Applied Physics*, 43(37):374021, 2010.

[222] D Glenn, H Zhang, A Benado, N Kasthuri, R Schalek, and R Lichtman, Jand Walsworth. Bioimaging applications using color centers in diamond. In *APS Division of Atomic, Molecular and Optical Physics Meeting Abstracts*, 2012.

[223] M-F Weng, S-Y Chiang, N-S Wang, and H Niu. Fluorescent nanodiamonds for specifically targeted bioimaging: Application to the interaction of transferrin with transferrin receptor. *Diamond and Related Materials*, 18(2):587–591, 2009.

[224] Jing Wu, Zhiqiang Ye, Guilan Wang, Dayong Jin, Jingli Yuan, Yafeng Guan, and James Piper. Visible-light-sensitized highly luminescent europium nanoparticles : preparation and application for time-gated luminescence bioimaging. *Journal of Materials Chemistry*, 19(9), 2009.

[225] B Grotz, M V Hauf, M Dankerl, B Naydenov, S Pezzagna, J Meijer, F Jelezko, M Wrachtrup, J nd Stutzmann, F Reinhard, and J A Garrido. Charge state manipulation of qubits in diamond. *Nature Communications*, 3, 2012.

[226] J Wrachtrup, F Jelezko, B Grotz, and L McGuinness. Nitrogen-vacancy centers close to surfaces. *MRS Bulletin*, 38(02), 2013.

[227] T Gaebel, M Domhan, C Wittmann, I Popa, F Jelezko, J Rabeau, A Greentree, S Prawer, E Trajkov, P R Hemmer, and J Wrachtrup. Photochromism in single nitrogen-vacancy defect in diamond. *Applied Physics B*, 82(2), 2005.

[228] F Jelezko, T Gaebel, I Popa, A Gruber, and J Wrachtrup. Observation of coherent oscillations in a single electron spin. *Physical review letters*, 92(7):076401, 2004.

[229] J Wrachtrup and F Jelezko. Processing quantum information in diamond . *Journal of Physics: Condensed Matter*, 2006.

[230] B Grotz, J Beck, P Neumann, B Naydenov, R Reuter, F Reinhard, F Jelezko, J Wrachtrup, D Schweinfurth, B Sarkar, and P Hemmer. Sensing external spins with nitrogen-vacancy diamond. *New Journal of Physics*, 13(5):055004, May 2011.

[231] G Waldherr, J Beck, M Steiner, P Neumann, and A Gali. Dark states of single nitrogen-vacancy centers in diamond unraveled by single shot NMR. *Physical Review Letters*, 106:157601, 2011.

[232] E Neu, M Agio, and C Becher. Photophysics of single silicon vacancy centers in diamond: implications for single photon emission. *Optics Express*, 20(18):19956, 2012.

[233] A Beveratos, R Brouri, T Gacoin, A Villing, and J P Poizat. Phys. Rev. Lett. 89, 187901 (2002) - Single Photon Quantum Cryptography. *Physical Review*, 2002.

[234] V Jacques, P Neumann, J Beck, M Markham, D Twitchen, J Meijer, F Kaiser, G Balasubramanian, F Jelezko, and J Wrachtrup. Dynamic polarization of single nuclear spins by optical pumping of nitrogen-vacancy color centers in diamond at room temperature. *Physical Review Letters*, 102(5):057403, 2009.

[235] K-M C Fu, C Santori, P E Barclay, I Aharonovich, S Prawer, N Meyer, A M Holm, and R G Beausoleil. Coupling of nitrogen-vacancy centers in diamond to a gap waveguide. *Applied Physics Letters*, 93(23):234107, 2008.

[236] T A Kennedy, J S Colton, J E Butler, R C Linares, and P J Doering. Long coherence times at 300 k for nitrogen-vacancy center spins in diamond grown by chemical vapor deposition. *Applied Physics Letters*, 83(20):4190, 2003.

[237] F H L Koppens, C Buizert, K-J Tielrooij, I T Vink, K C Nowack, T Meunier, L P Kouwenhoven, and L M K Vandersypen. Driven coherent oscillations of a single electron spin in a quantum dot. *Nature*, 442(7104):766–771, 2006.

[238] L T Hall, J H Cole, C D Hill, and L C L Hollenberg. Sensing of Fluctuating Nanoscale Magnetic Fields Using Nitrogen-Vacancy Centers in Diamond. *Physical Review Letters*, 103(22):220802, 2009.

[239] H J Mamin, M Kim, M H Sherwood, C T Rettner, K Ohno, D D Awschalom, and D Rugar. Nanoscale nuclear magnetic resonance with a nitrogen-vacancy spin sensor. *Science*, 339(6119):557–560, 2013.

[240] S Machida, Y Nakayama, and H Ishii. Charge-up durability and in-situ tracking of a photooxidation process of rubrene studied by photoelectron yield spectroscopy:

toward photoelectronic investigation on organic electronics devices. *Hyomen Kagaku*, 29(9):543–549, 2008.

[241] Alison Mainwood. Nitrogen and nitrogen-vacancy complexes and their formation in diamond. *Physical Review B*, 49(12):7934, 1994.

[242] N B Manson, J P Harrison, and M J Sellars. Nitrogen-vacancy center in diamond: Model of the electronic structure and associated dynamics. *Physical Review B*, 74 (10):104303, 2006.

[243] K Beha, A Batalov, N B Manson, R Bratschitsch, and A Leitenstorfer. Optimum Photoluminescence Excitation and Recharging Cycle of Single Nitrogen-Vacancy Centers in Ultrapure Diamond. *Physical Review Letters*, 109(9):097404, August 2012.

[244] Y V Pleskov. Electrochemistry of diamond: A review. *Russian Journal of Electrochemistry*, 38(12):1275–1291, 2002.

[245] P K Baumann and R J Nemanich. Characterization of copper-diamond (100),(111), and (110) interfaces: Electron affinity and schottky barrier. *Physical Review B*, 58(3):1643, 1998.

[246] J P Goss, P R Briddon, R Jones, and S Sque. Donor and acceptor states in diamond. *Diamond and Related Materials*, 13(4):684–690, 2004.

[247] J Ristein, F Maier, M Riedel, M Stammer, and L Ley. Diamond surface conductivity experiments and photoelectron spectroscopy. *Diamond and Related Materials*, 10(3):416–422, 2001.

[248] F Maier, M Riedel, B Mantel, J Ristein, and L Ley. Origin of surface conductivity in diamond. *Physical Review Letters*, 85(16):3472, 2000.

[249] W Deferme, K Haenen, G Tanasa, C F J Flipse, and M Nesládek. Compositional and electrical characterisation of the hydrogen–oxygen terminated diamond (100) surface. *physica status solidi (a)*, 203(12):3114–3120, 2006.

[250] T Maki, S Shikama, M Komori, Yi Sakaguchi, K Sakuta, and T Kobayashi. Hydrogenating effect of single-crystal diamond surface. *Japanese Journal of Applied Physics*, 31(10A):L1446, 1992.

[251] S Sque, R Jones, and P Briddon. Structure, electronics, and interaction of hydrogen and oxygen on diamond surfaces. *Physical Review B*, 73(8):085313, 2006.

[252] M V Hauf, B Grotz, B Naydenov, M Dankerl, S Pezzagna, J Meijer, F Jelezko, J Wrachtrup, M Stutzmann, F Reinhard, and J A Garrido. Chemical control of the charge state of nitrogen-vacancy centers in diamond. *Physical Review B*, 83 (8):081304, 2011.

[253] A K Tiwari, J P Goss, P R Briddon, N G Wright, A B Horsfall, R Jones, H Pinto, and M J Rayson. Calculated electron affinity and stability of halogen-terminated diamond. *Physical Review B*, 84(24):245305, 2011.

[254] J B Cui, J Ristein, and L Ley. Electron affinity of the bare and hydrogen covered single crystal diamond (111) surface. *Physical Review Letters*, 81(2):429, 1998.

[255] J B Cui, J Ristein, and L Ley. Low-threshold electron emission from diamond. *Physical Review B*, 60(23):16135, 1999.

[256] T E Derry, C C P Madiba, and J P F Sellschop. Oxygen and hydrogen on the surface of diamond. *Nuclear Instruments and Methods in Physics Research*, 218 (1):559–562, 1983.

[257] M C Salvadori, W W R Araujo, F Teixeira, M Cattani, A Pasquarelli, E M Oks, and I G Brown. Termination of diamond surfaces with hydrogen, oxygen and fluorine using a small, simple plasma gun. *Diamond and Related Materials*, 19(4): 324–328, 2010.

[258] A Tallaire, J Achard, F Silva, R S Sussmann, A Gicquel, and E Rzepka. Oxygen plasma pre-treatments for high quality homoepitaxial cvd diamond deposition. *Physica Status Solidi (a)*, 201(11):2419–2424, 2004.

[259] T I Hukka, T A Pakkanen, and M P D'Evelyn. Chemisorption of fluorine, chlorine, hf, and hcl on the diamond (100) 2x1 surface: an ab initio study. *The Journal of Physical Chemistry*, 99(13):4710–4719, 1995.

[260] K J Rietwyk, S L Wong, L Cao, K M O'Donnell, L Ley, A T S Wee, and C I Pakes. Work function and electron affinity of the fluorine-terminated (100) diamond surface. *Applied Physics Letters*, 102(9):091604, 2013.

[261] F Maier, J Ristein, and L Ley. Electron affinity of plasma-hydrogenated and chemically oxidized diamond (100) surfaces. *Physical Review B*, 64(16):165411, 2001.

[262] T Ando, K Yamamoto, M Matsuzawa, Y Takamatsu, S Kawasaki, F Okino, H Touhara, M Kamo, and Y Sato. Direct interaction of elemental fluorine with diamond surfaces. *Diamond and Related Materials*, 5(9):1021–1025, 1996.

[263] M V Hauf, B Grotz, B Naydenov, M Dankerl, S Pezzagna, J Meijer, F Jelezko, J Wrachtrup, M Stutzmann, F Reinhard, and J A Garrido. Chemical control of the charge state of nitrogen-vacancy centers in diamond. *Physical Review B*, 83 (8):081304, February 2011.

[264] S Cui and E L Hu. Increased negatively charged nitrogen-vacancy centers in fluorinated diamond. *Applied Physics Letters*, 103(5):051603, 2013.

[265] L Rondin, G Dantelle, A Slablab, F Grosshans, F Treussart, P Bergonzo, S Perruchas, T Gacoin, M Chaigneau, H C Chang, V Jacques, and J F Roch. Surface-induced charge state conversion of nitrogen-vacancy defects in nanodiamonds. *Physical Review B*, 82(11):115449, 2010.

[266] W Hu, Z Li, and J Yang. Surface and size effects on the charge state of nv center in nanodiamonds. *Computational and Theoretical Chemistry*, 1021:49–53, 2013.

[267] A Tarditi, P Kondratyuk, P K Wong, and A J Gellman. Controlling the work function of a diamond-like carbon surface by fluorination with XeF[sub 2]. *Journal of Vacuum Science & Technology A: Vacuum, Surfaces, and Films*, 28(5):1250, 2010.

[268] I Utke, P Hoffmann, and J Melngailis. Gas-assisted focused electron beam and ion beam processing and fabrication. *Journal of Vacuum Science & Technology B*, 26 (4):1197, 2008.

[269] C Popov, W Kulisch, S Bliznakov, G Ceccone, D Gilliland, L Sirghi, and F Rossi. Surface modification of nanocrystalline diamond/amorphous carbon composite films. *Diamond and Related Materials*, 17(7-10), 2008.

[270] R J Behm, P A Thiel, P R Norton, and P E Bindner. The oxidation of CO on Pt (100): Mechanism and structure. *Surface Science*, 147(1):143–161, 1984.

[271] D A Mantell, K Kunimori, S B Ryali, G L Haller, and J B Fenn. The dynamics of CO oxidation on Pt deduced from translational, rotational and vibrational excitation in product CO_2. *Surface Science*, 172(2):281–302, 1986.

[272] S M McClure and D W Goodman. New insights into catalytic CO oxidation on Pt-group metals at elevated pressures. *Chemical Physics Letters*, 469(1):1–13, 2009.

[273] G Ertl, M Neumann, and KM Streit. Chemisorption of CO on the Pt (111) surface. *Surface Science*, 64(2):393–410, 1977.

[274] J Ma, N Sun, X Zhang, N Zhao, F Xiao, W Wei, and Y Sun. A short review of catalysis for CO_2 conversion. *Catalysis Today*, 148(3):221–231, 2009.

[275] A Manasilp and E Gulari. Selective CO oxidation over Pt/alumina catalysts for fuel cell applications. *Applied Catalysis B: Environmental*, 37(1):17–25, 2002.

[276] L Frachebourg, P L Krapivsky, and S Redner. Heterogeneous catalysis on a disordered surface. *Physical Review Letters*, 75(15):2891, 1995.

[277] B Hendriksen and J Frenken. CO Oxidation on Pt(110): Scanning Tunneling Microscopy Inside a High-Pressure Flow Reactor. *Physical Review Letters*, 89(4): 046101, July 2002.

[278] F Gao, S M McClure, Y Cai, K K Gath, Y Wang, M S Chen, Q L Guo, and D W Goodman. CO oxidation trends on Pt-group metals from ultrahigh vacuum to near atmospheric pressures: A combined in situ PM-IRAS and reaction kinetics study. *Surface Science*, 603(1), January 2009.

[279] A Manasilp and E Gulari. Selective CO oxidation over Pt/alumina catalysts for fuel cell applications. *Applied Catalysis B: Environmental*, 37(1):17–25, 2002.

[280] C Wang and R Gomer. The adsorption of CO on the (100) plane of tungsten; thermal and work function measurements. *Surface Science*, 90(1):10–36, 1979.

[281] John Freel. Chemisorption on supported platinum: Ii. stoichiometry for hydrogen, oxygen and carbon monoxide. *Journal of Catalysis*, 25(1):149–160, 1972.

[282] G Ertl, P R Norton, and J Rüstig. Kinetic oscillations in the platinum-catalyzed oxidation of CO. *Physical Review Letters*, 49(2):177, 1982.

[283] V S Bagotzky and M R Tarasevich. Oxygen adsorption on platinum and platinum metals: Part i. investigation of the adsorption mechanism by the potentiodynamic method. *Journal of Electroanalytical Chemistry and Interfacial Electrochemistry*, 101(1):1–17, 1979.

[284] C W Oatley. The adsorption of oxygen and hydrogen on platinum and the removal of these gases by positive-ion bombardment. *Proceedings of the Physical Society*, 51(2):318, 1939.

[285] J L Gland and V N Korchak. The adsorption of oxygen on a stepped platinum single crystal surface. *Surface Science*, 75(4):733–750, 1978.

[286] C-W Chen and M Akashi. Synthesis, characterization, and catalytic properties of colloidal platinum nanoparticles protected by poly (n-isopropylacrylamide). *Langmuir*, 13(24):6465–6472, 1997.

[287] P R Norton. An investigation of the adsorption of oxygen and oxygen containing species on platinum by photoelectron spectroscopy. *Surface Science*, 47(1):98–114, 1975.

[288] J C Tully. Dynamics of gas–surface interactions: Reaction of atomic oxygen with adsorbed carbon on platinum. *The Journal of Chemical Physics*, 73(12):6333–6342, 1980.

[289] N Wagner and E Gülzow. Change of electrochemical impedance spectra (eis) with time during CO-poisoning of the Pt-anode in a membrane fuel cell. *Journal of Power Sources*, 127(1):341–347, 2004.

[290] H P Dhar, L G Christner, A K Kush, and H C Maru. Performance study of a fuel cell pt-on-c anode in presence of CO and CO_2, and calculation of adsorption parameters for CO poisoning. *Journal of the Electrochemical Society*, 133(8):1574–1582, 1986.

[291] F Gao, S McClure, M Chen, and D W Goodman. Comment on catalytic activity of the rh surface oxide: CO oxidation over rh (111) under realistic conditions. *The Journal of Physical Chemistry C*, 114(50):22369–22371, 2010.

[292] R van Rijn, O Balmes, R Felici, J Gustafson, D Wermeille, R Westerstrom, E Lundgren, and J W M Frenken. Comment on CO oxidation on Pt-group metals from

ultrahigh vacuum to near atmospheric pressures. 2. palladium and platinum. *The Journal of Physical Chemistry C*, 114(14):6875–6876, 2010.

[293] E R Kötz, H Neff, and K Müller. A ups, xps and work function study of emersed silver, platinum and gold electrodes. *Journal of Electroanalytical Chemistry and Interfacial Electrochemistry*, 215(1):331–344, 1986.

[294] S Nettesheim, A von Oertzen, H H Rotermund, and G Ertl. Reaction diffusion patterns in the catalytic CO-oxidation on Pt(110): Front propagation and spiral waves. *The Journal of Chemical Physics*, 98(12):9977, 1993.

[295] S Bebelis and C G Vayenas. Non-faradaic electrochemical modification of catalytic activity: 1. the case of ethylene oxidation on Pt. *Journal of Catalysis*, 118(1):125–146, 1989.

[296] R Culver, J Pritchard, and F C Tompkins. The dipole moment and nature of the chemisorption bond. *Zeitschrift für Elektrochemie, Berichte der Bunsengesellschaft für physikalische Chemie*, 63(7):741–745, 1959.

[297] J W Gadzuk. Surface molecules and chemisorption: I. adatom density of states. *Surface Science*, 43(1):44–60, 1974.

[298] P Pianetta, I Lindau, C M Garner, and W E Spicer. Chemisorption and oxidation studies of the (110) surfaces of GaAs, GaSb, and InP. *Physical Review B*, 18(6): 2792, 1978.

[299] Yi Nishiyama and H Wise. Surface interactions between chemisorbed species on platinum: Carbon monoxide, hydrogen, oxygen, and methanol. *Journal of Catalysis*, 32(1):50–62, 1974.

[300] H P Bonzel and R Ku. Adsorbate interactions on a Pt (110) surface. i. sulfur and carbon monoxide. *The Journal of Chemical Physics*, 58(10):4617–4624, 1973.

[301] I Toyoshima and G A Somorjai. Heats of chemisorption of O_2, H_2, CO, CO_2, and N_2 on polycrystalline and single crystal transition metal surfaces. *Catalysis Reviews Science and Engineering*, 19(1):105–159, 1979.

[302] C M Comrie and R M Lambert. Chemisorption and surface structural chemistry of carbon monoxide on Pt (110). *Journal of the Chemical Society, Faraday Transactions 1: Physical Chemistry in Condensed Phases*, 72:1659–1669, 1976.

[303] K C Lin, J D Witt, and R M Hammaker. Structure of carbon monoxide chemisorbed on platinum. *The Journal of Chemical Physics*, 55(3):1148–1151, 1971.

[304] P T Dawson and Y K Peng. The adsorption, desorption, and exchange reactions of oxygen, hydrogen, and water on platinum surfaces: Iv. field emission studies on the adsorption of water, hydrogen and the reaction between hydrogen and adsorbed oxygen. *Surface Science*, 92(1):1–13, 1980.

[305] G Rupprechter, T Dellwig, H Unterhalt, and H-J Freund. High-pressure carbon monoxide adsorption on Pt (111) revisited: a sum frequency generation study. *The Journal of Physical Chemistry B*, 105(18):3797–3802, 2001.

[306] H B Michaelson. The work function of the elements and its periodicity. *Journal of Applied Physics*, 48(11):4729–4733, 1977.

[307] G N Derry and Z Ji-Zhong. Work function of Pt(111). *Physical Review B*, 39: 1940–1941, Jan 1989.

[308] N Freyer, M Kiskinova, G Pirug, and H P Bonzel. Oxygen adsorption on Pt(110)-(1×2) and Pt(110)-(1×1). *Surface Science*, 166(1):206 – 220, 1986.

[309] X-Q Gong, R Raval, and P Hu. General Insight into CO Oxidation: A Density Functional Theory Study of the Reaction Mechanism on Platinum Oxides. *Physical Review Letters*, 93(10):106104, September 2004.

[310] Scott Warwick Morgan. *Gaseous secondary electron detection and cascade amplification in the environmental scanning electron microscope*. PhD thesis, University of Technology, Sydney, 2005.